ornl

ORNL/TM-2000/16

OAK RIDGE NATIONAL LABORATORY

LOCKHEED MARTIN

Heavy Vehicle Propulsion System Materials Program Semiannual Progress Report for April 1999 Through September 1999

Prepared for
U.S. Department of Energy
Assistant Secretary for
Energy Efficiency and Renewable Energy
Office of Transportation Technologies

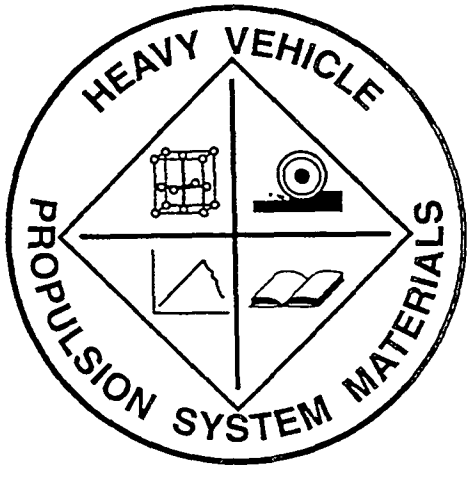

MANAGED AND OPERATED BY
LOCKHEED MARTIN ENERGY RESEARCH CORPORATION
FOR THE UNITED STATES
DEPARTMENT OF ENERGY

DISCLAIMER

Portions of this document may be illegible in electronic image products. Images are produced from the best available original document.

ORNL/TM-2000/16

Metals and Ceramics Division

HEAVY VEHICLE PROPULSION SYSTEM MATERIALS PROGRAM SEMIANNUAL PROGRESS REPORT FOR APRIL 1999 THROUGH SEPTEMBER 1999

D. R. Johnson
Program Manager

Date Published: January 2000

Prepared for
U.S. Department of Energy
Assistant Secretary for Energy Efficiency and Renewable Energy
Office of Transportation Technologies
EE 07 01 000

Prepared by the
OAK RIDGE NATIONAL LABORATORY
Oak Ridge, Tennessee 37831-6285
managed by
LOCKHEED MARTIN ENERGY RESEARCH CORP.
for the
U.S. DEPARTMENT OF ENERGY
under Contract DE-AC05-96OR22464

REPORTS PREVIOUSLY ISSUED

ORNL/TM-9325	Period March 1983-September 1983
ORNL/TM-9466	Period October 1983-March 1984
ORNL/TM-9497	Period April 1984-September 1984
ORNL/TM-9673	Period October 1984-March 1985
ORNL/IM-9947	Period April 1985-September 1985
ORNL/TM-10079	Period October 1985-March 1986
ORNL/TM-10308	Period April 1986-September 1986
ORNL/TM-10469	Period October 1986-March 1987
ORNL/TM-10705	Period April 1987-September 1987
ORNL/TM-10838	Period October 1987-March 1988
ORNL/TM-11116	Period April 1988-September 1988
ORNL/TM-11239	Period October 1988-March 1989
ORNL/TM-11489	Period April 1989-September 1989
ORNL/TM-11586	Period October 1989-March 1990
ORNL/TM-11719	Period April 1990-September 1990
ORNL/TM-11859	Period October 1990-March 1991
ORNL/TM-11984	Period April 1991-September 1991
ORNL/TM-12133	Period October 1991-March 1992
ORNL/TM-12363	Period April 1992-September 1992
ORNL/TM-12428	Period October 1992-March 1993
ORNL/TM-12674	Period April 1993-September 1993
ORNL/TM-12778	Period October 1993-March 1994
ORNL/TM-12924	Period April 1994-September 1994
ORNL/TM-13046	Period October 1994-March 1995
ORNL/TM-13219	Period April 1995-September 1995
ORNL/TM-13262	Period October 1995-March 1996
ORNL/TM-13395	Period April 1996-September 1996
ORNL/TM-13467	Period October 1996-March 1997
ORNL/TM-13562	Period April 1997-September 1997
ORNL/TM-13648	Period October 1997-March 1998
ORNL/TM-13735	Period April 1998-September 1998
ORNL/TM-1999/95	Period October 1998-March 1999

Research sponsored by the U.S. Department of Energy, Assistant Secretary for Energy Efficiency and Renewable Energy, Office of Transportation Technologies, as part of the Heavy Vehicle Propulsion System Materials Program, under contract DE-AC05-96OR22464 with Lockheed Martin Energy Research Corporation.

CONTENTS

SUMMARY AND INTRODUCTION 1

COST EFFECTIVE HIGH PERFORMANCE MATERIALS AND PROCESSING 3

Cost-Effective Smart Materials for Diesel Engine Applications (ORNL) 5

Low Cost High Toughness Ceramics (ORNL) 33

Cost-Effective Sintering of Silicon Nitride Ceramics (SIU-C) 50

Diesel Particulate Trap Development 70

ADVANCED MANUFACTURING TECHNOLOGY 73

Durability of Diesel Engine Component Materials (ORNL) 75

Laser Scatter Methods for Detecting Subsurface Machining Damage in Ceramics (Argonne National Laboratory) 78

Intermetallic -Bonded Cermets (ORNL) 85

Cost Effective Machining of Ceramic Engine Components (ORNL) 89

TESTING AND CHARACTERIZATION 95

X-Ray Computed Tomographic Imaging (Argonne National Laboratory) 97

Testing and Evaluation of Advanced Ceramics at High Temperature (North Carolina A&T State University) 108

Life Prediction Verification (ORNL) 116

Field Emission Analytical Electron Microscopy for Characterization of Catalyst Microstructures (ORNL) 123

MATERIALS AND TESTING STANDARDS 127

IEA ANNEX II Management (ORNL) 129

NDE Standards for Advanced Ceramics (ORNL) 131

Ceramic Characterization and Standards for Heat Engines (NIST) 134

Ceramic Mechanical Property Test Method Development (NIST) 135

HEAVY VEHICLE PROPULSION SYSTEM MATERIALS PROGRAM
SEMIANNUAL PROGRESS REPORT
FOR APRIL 1999 THROUGH SEPTEMBER 1999

SUMMARY AND INTRODUCTION

The purpose of the Heavy Vehicle Propulsion System Materials Program is the development of materials: ceramics, intermetallics, metal alloys, and metal and ceramic coatings, to support the dieselization of class 1-3 trucks to realize a 35% fuel-economy improvement over current gasoline-fueled trucks and to support commercialization of fuel-flexible LE-55 low-emissions, high-efficiency diesel engines for class 7-8 trucks.

The Office of Transportation Technologies, Office of Heavy Vehicle Technologies (OTT OHVT) has an active program to develop the technology for advanced LE-55 diesel engines with 55% efficiency and low emissions levels of 2.0 g/bhp-h NOx and 0.05 g/bhp-h particulates. The goal is also for the LE-55 engine to run on natural gas with efficiency approaching that of diesel fuel. The LE-55 program is being completed in FY 1997 and, after approximately 10 years of effort, has largely met the program goals of 55% efficiency and low emissions. However, the commercialization of the LE-55 technology requires more durable materials than those that have been used to demonstrate the goals. Heavy Vehicle Propulsion System Materials will, in concert with the heavy duty diesel engine companies, develop the durable materials required to commercialize the LE-55 technologies.

OTT OHVT also recognizes a significant opportunity for reduction in petroleum consumption by dieselization of pickup trucks, vans, and sport utility vehicles. Application of the diesel engine to class 1, 2, and 3 trucks is expected to yield a 35% increase in fuel economy per vehicle. The foremost barrier to diesel use in this market is emission control. Once an engine is made certifiable, subsequent challenges will be in cost; noise, vibration, and harshness (NVH); and performance.

The design of advanced components for high-efficiency diesel engines has, in some cases, pushed the performance envelope for materials of construction past the point of reliable operation. Higher mechanical and tribological stresses and higher temperatures of advanced designs limit the engine designer; advanced materials allow the design of components that may operate reliably at higher stresses and temperatures, thus enabling more efficient engine designs. Advanced materials also offer the opportunity to improve the emissions, NVH, and performance of diesel engines for pickup trucks, vans, and sport utility vehicles.

The principal areas of research are:

Cost Effective High Performance Materials and Processing
Advanced Manufacturing Technology
Testing and Characterization
Materials and Testing Standards

COST EFFECTIVE HIGH PERFORMANCE MATERIALS AND PROCESSING

Cost-Effective Smart Materials for Diesel Engine Applications

J. O. Kiggans, Jr., T. N. Tiegs, F. C. Montgomery,
L. C. Maxey, A. R. Steffans and P. J. Schroeder
Oak Ridge National Laboratory
Oak Ridge, TN 37831

Objective / Scope

There are two objectives for this project. The first is to evaluate the cost-effectiveness and maturity of various "Smart Materials Technologies," which are under consideration for diesel engine applications, such as fuel injection systems. The second is to develop "Smart Materials," to be incorporated into working actuators and sensors.

Section 1

Task 1 – Characterization of PZT-4 materials modified by chemical additives

The goal of the present effort is to determine if sintering additives, when combined with a commercial PZT-4 powder (APC Ceramics Inc), can lower the sintering temperature of the materials below 1150°C. Five sample types were made for this study: PZT-4 powders with a) no additive (control), b) 2 wt. % lead oxide (PbO), c) 2 wt. % bismuth oxide (Bi_2O_3), d) 2 wt. % niobium oxide (Nb_2O_3), or e) 2 wt. % silver carbonate (Ag_2CO_3). Samples were die pressed, processed for binder burn-out in an open alumina tray at 1 °C to 600 °C and held for a 1 h dwell before cooling at 10 °C per minute. PZT samples were placed in alumina setter crucibles, each of which was covered by a second alumina crucible. A thin powder bed of 90 wt. % $PbZrO_3$-10 wt % ZrO_2 powder was placed around the outer sealing surface of the top cover crucibles to provide atmosphere control. The sample packages were then sintered in an alumina tube furnace in flowing air at 10°C/min to final temperature of, 1120, 1150, and 1275 °C for different times.

The sintered samples were ground using a RotoPol grinding/polishing machine (Struers Inc.) with 500, 1200, and 4000 grit SiC paper. The samples were then sputter coated with gold, and samples were then poled at 3 kV per mm sample thickness. The piezoelectric charge constant, d_{33}, was measured 24 h after poling using a Pennebaker Model 8000 Piezo d_{33} Tester (APC Inc.). In addition, the relative dielectric constant, K^T_{33}, at 1000 Hz, and the electromechanical coupling

coefficient, k_p and the mechanical Q values, Q_m, were measured using a Hewlett Packard 4194a Impedance/Gain Phase Analyzer with a HP 16034E test fixture.

The poled PZT-4 samples were again ground using the RotoPol grinding/polishing machine (Struers Inc.) with 1200, and 4000 grit SiC paper. The samples were then polished with 3 micron diamond and then 0.05 micron silica solution (Struers OP-S Suspension). The samples were rinsed by ultrasonic cleaning in water. The polished samples were etched for 5, 10, or 15 min. in a 18.5 wt. % hydrochloric acid solution. Samples were cleaned with acetone and isopropyl alcohol to remove residual silica from the polishing step, and were sputter coated with a thin layer of gold for SEM examination.

Figure 1a shows the sintered densities (% theoretical density), the piezoelectric constant (d_{33}) values, and the mechanical Q (Q_m) values for samples sintered at 1110 °C for 3 h or 1275 °C for 3 h. The sintering data indicates that all the five sample types sintered to 100 % theoretical density (T.D.) at the 1287 °C 3 h sintering condition, however only the samples with PbO, Nb_2O_3, and Ag_2CO_3 sintered to near 100 % T.D. at the 1110 °C 3 h sintering condition. The sample containing Bi_2O_3 sintered to ~ 65 % T.D at 1110 °C. Figure 1b shows that the d_{33} values were low for the control PZT-4 samples sintered at 1110 °C, the samples containing PbO, and even lower for the samples containing Nb_2O_3, and Ag_2CO_3 additions. The d_{33} values were acceptable for control PZT-4 samples and the samples containing PbO, or Bi_2O_3 which were sintered at 1287 °C. The low d_{33} values of the Nb_2O_3, and Ag_2CO_3 samples was due to the difficulty in poling the samples at high voltages. In particular, there was arcing during poling of the samples containing Ag. The samples with the Bi_2O_3 additions had acceptable d_{33} values, even with the lower densities.

Data in Figure 1c lists the Q_m values for sintered samples. Samples containing added PbO, Bi_2O_3, and Ag_2CO_3 which were sintered at 1110 °C had much lower Q_m values than the control sample which was sintered at 1287 °C. Although the data is incomplete, it is believed that the sintering additives depress the Q_m for all the materials at the concentrations utilized in these tests.

Figure 2 shows photographs of the PZT samples (excluding the Nb_2O_3) sintered using the 1110 and 1287 °C conditions. These photos show that an at least doubling of grain sizes occurred in all samples sintered at 1287 °C versus 1110 °C.

In summary, the densification of the PZT-4 materials containing PbO, Nb_2O_3, and Ag_2CO_3 additions were improved over the undoped control material and PZT containing Bi_2O_3; however, the electrical properties of all PZT-4 materials with dopant additions were degraded. The SEM results do not give the answers for the materials properties. We speculate that the better electrical properties exhibited by materials sintered at the 1287 °C conditions may not only be due to the larger grain sizes observed in these materials; but may due to the smaller amounts of intragranular materials in these materials. Since only one concentration of each additive was used in these experiments, other concentrations need to be tested. The PbO and Ag_2CO_3 show the most promise for further work.

Task 2. Evaluation of Terfenol-D Magnetostrictive Actuator

Dynamic testing of actuators that are under consideration for the Smart Actuators program as essential for determining their suitability for applications requiring rapid cycle performance. It is essential to verify the manufacturer's stated performance characteristics. The system under evaluation in this study consists of a magnetostrictive actuator and the associated drive amplifier purchased from Etrema Inc. The emphasis of the present work was to determine the displacement capability of the actuator as a function of the electrical drive frequencies.

Figure 3 is a schematic of the actuator and the associated equipment used to test or drive the actuator. The magnetostrictive actuator is an Etrema AA050H060 ES1 rated at 60 μm total travel. The power or drive amplifier is a Titan ACP-03, which is a high current device that is primarily designed for driving ac motor systems. The amplifier output is capacitively-coupled and therefore is not capable of producing a dc output or an "asymmetrical" ac output. In other words, the output signal must swing from a positive to a negative voltage on each cycle and be symmetrical about the (ground) baseline. This limitation is significant for the projected applications, where a drive signal of interest will likely by highly asymmetric. The signal waveform for the power amplifier was generated by a Hewlett Packard 8904A Multifunction Synthesizer (generator). A bipolar square wave (symmetrical about the zero voltage baseline) was sent to the drive signal for these tests.

A non-contacting fiber optic displacement probe (Philtec D20-M) was calibrated for use in these tests. The probe is designed for optimum performance when positioned within a few hundred microns of (and normal to) a spectrally reflective surface (i.e. a mirror). The displacement probe was calibrated using a linear interferometer as a reference standard. The probe was aligned to a mirror attached to the optical target of the linear

interferometer. The output voltage from the displacement probe was measured over a range of displacements from 250 to 400 microns from the mirror surface. The response of the probe over that range was -8.80 mV per micron. Dynamic response of the Philtec optical probe was not evaluated because the range of interest (3 kHz) was significantly lower than the manufacturer's documented roll-off frequency (20 kHz) and should have a negligible contribution to error.

Both the drive signal amplitude from the Titan ACP-03, and the output voltage from the Philtec D20-M probe were monitored using a Tektronix 360 digital oscilloscope. This data was then transferred to a computer for data analysis.

The actuator performance specifications provided by the manufacturer indicate that it is a "high frequency" model, capable of performing at frequencies from dc up to 6 kHz with a maximum actuator displacement of 60 microns. Impedance data from dc to 10 kHz is provided with the actuator. The displacement curve for the actuator indicates a response of approximately 1.2 microns for each 100 mA of input current over a limited range. The impedance of the actuator from dc to 2 kHz varies from 28 to 32 ohms. A drive signal of +/- 10V (selected for these tests) is expected to produce a current of 333 mA into a nominal 30 ohm load. Based on the displacement curve, a nominal actuator response of +/- 4 microns should be developed in response to this drive signal.

Dynamic performance was measured at several frequencies, from 150 Hz to 2 kHz. The resulting curves are shown in Figure 4. The first set of curves, acquired at 150 Hz show the response of the actuator lagging the drive signal with a rise time of just under 2 millisecond to reach full actuator extension. At this frequency, however, the actuator does obtain full extension in both polarities. The response from the Philtec probe is approximately +/- 160 mV, which should correlate to a displacement of +/- 18.2 microns.

The next set of curves, taken at 200 Hz show that the actuator is achieving full response only during the negative drive signal cycle. At 300 Hz, the next set of curves show that the actuator never quite achieves full extension in either polarity. The operation is worsened at 500 Hz and 1000 Hz. Finally, at 2000 Hz, with the same +/- 10 V amplitude drive signal applied, the response of the Philtec probe is only a little over +/- 10 mV and is highly distorted.

These dynamic tests suggest several areas of concern in relating the manufacturer's stated performance specifications and test results to the results obtained. The first point of concern is the frequency response. From the product description, the sensor seems to be specified for 60 microns displacement up to a frequency of 6 kHz. Because the

impedance curve increases only slightly from dc to 2 kHz, it should be reasonable to assume that a constant drive signal applied over that range of frequencies would produce a nominally constant range of actuator displacements. The actuator displacement curve provided by the manufacturer (data taken at a frequency of 0.5 Hz) shows a response characteristic of about 1.2 microns for each 100 mA of drive current.

The test results show that the actuator response is minimal and highly distorted at 2 kHz, well below the stated performance range. Despite the impedance data being essentially flat from dc to 2 kHz, the sensor performance degrades rapidly between 150 Hz and 1 kHz. Finally, the actuator displacement for a +/- 10 V input achieves a maximum travel of over 18 microns at 150 Hz. The impedance of the sensor is about 28 ohms at 150 Hz, yielding a current of +/- 0.36 A. This implies that the actuator response is about 5 microns per 100 mA, well in excess of the 1.2 microns per 100 mA implied by the manufacturers performance curves.

Section 2

Task 1

Investigators have reported that reactive calcination of lead zirconate titanate (PZT) precursors results in PZT powders, which are easily milled to small particle sizes and can be sintered at low temperatures (less than 1100°C).[1,2] It has also been reported that the use of lead titanate ($PbTiO_3$) as one of the reactants can lead to minimal volume expansion during PZT formation.[1] Low expansion of the materials during PZT formation may aid in reducing the shrinkage needed during the sintering process. The goal of the this effort is to determine if either of these two approaches can be used to make PZT powders which will sinter at sufficiently low temperature that will allow the use of Ag electrodes in PZT actuator materials.

Reactive calcined PZT powder was prepared according to the following procedure: A mixture of titanium dioxide, TiO_2, (2 – 3 μm, 99+ %, Alfa Aesar); zirconium oxide, ZrO_2,(-325 mesh, 99+ %, Alfa Aesar), at a 0.52 to 0.48 molar ratio, was mixed with water and 1 wt. % polyvinyl pyrrolidone (PVP K-15), and milled overnight using partially stabilized zirconia media. The slurry was screened to remove the media and the powder dried at 90 °C. The powder mixture was then dry milled overnight with the zirconia media and the media screened out. A portion of the powder, designated PW-1a, was placed in an alumina tray and calcined at 1250 °C, 1300°C, 1300 °C, and 1350 °C with a 4 h dwell at each temperature before cooling so a sample of the powder could be taken for x-ray analysis. A second portion of the powder was calcined at 1400°C for 4h, and

designated PW-1b. The PW1a and PW1b clacined powders were milled separately overnight with zirconia media in isopropyl alcohol. The powders were dried and SEM analyses were performed on the powders. The PW1a powder was then mixed with PbO to give a composition of $Pb(Zr_{0.52}Ti_{0.48})O_3$. The mix of powders was dry ball milled 16 h with partially stabilized zirconia media. The media was separated out, and the powder calcined in an alumina crucible to 725°C for 4 h in air (the reactive calcination). This powder is designated PW1a-1.

Three sample types were made using the PW1a-1 powder. Portions of the powder were ball milled in water for 4 h with 1 wt. % PVP K-15 and, a) 2 wt. % lead oxide (PbO); b) 2 wt. % PbO and 0.5 wt. % silver carbonate (Ag_2CO_3); or c) 2 wt. % PbO and 2 wt. % niobium oxide (Nb_2O_5). The powders were dried at 90 °C and ground in a nylon jar containing two, 1 cm diameter partially-stabilized zirconia milling media using a Spex mill. Samples were die pressed in a 2.8 cm diameter steel die to approximately 70 MPa, heated in air to 600°C for 1 h for binder burn-out, and sintered at 1000°C for 1 h, or 1060 °C for 48 h using sintering procedures described in the previous section.

Low expansion PZT powder, designated PW2, was made by the following procedure: A 100 g batch of powder was formulated, containing PbO (99.9 %, -325 mesh, Alfa Aesar), ZrO_2 (-325 mesh, 99+ % Alfa Aesar); $PbTiO_3$ (99.5 %, -325 mesh, Alfa Aesar); and strontium carbonate $SrCO_3$, (99 %, Mallinckrodt); in quantities to give a final molar ratio after calcination of $(Pb_{0.94}Sr_{0.06})(Zr_{0.53}Ti_{0.47})O_3$. PVP K-15 was added at 1 wt. % as a binder. The powders were ball milled with partially stabilized zirconia media overnight, dried, and broken up with an alumina mortar and pestle. Samples were die pressed in a 2.8 cm diameter steel die to approximately 41 MPa, heated in air to 600°C for binder burnout, and sintered at 1000°C for 1 h or 1250 °C for 3 h using procedures described in previous reports. Densities, x-ray analyses, and SEM analyses were performed on sintered discs.

The PW1a " reactively calcined" powder was made to determine if this method could produce easily milled and sintered PZT precursor materials. Reports by Shrout et. al[1] have indicated that powders fabricated using similar methods can be sintered at much lower temperatures than standard commercial powders. One key step in this process is the production of a $Zr_{0.52}Ti_{0.48}O_2$ intermediate powder from the calcination of ZrO_2 and TiO_2. The $Zr_{0.52}Ti_{0.48}O_2$ powder is then reacted with PbO at around 725°C to produce $PbZr_{0.52}Ti_{0.48}O_3$ powder, which is then milled, consolidated into samples, and sintered. Figures 5 and 6 show the x-ray diffraction patterns for two batches of $Zr_{0.52}Ti_{0.48}O_2$ powders made from separate calcination treatments of the ZrO_2 and TiO_2 powder mixtures. The first batch,

PW1a, was made from successive 4 h calcination treatments of the same powder mixture at 1250, 1300, 1300, and 1350°C. ZrO_2 and TiO_2 peaks in Figures 5 a and b show that after the 1250°C and 1300°C, the starting powders did not completely react with each other. The second 1300°C calcination (Figure 5c) resulted in an almost complete reaction between the ZrO_2 and TiO_2 powders. The x-ray pattern (Figure 6a) of the 1350°C 4 h calcine shows that the reaction was completed. The x-ray diffraction pattern (Figure 6b) of a second batch of ZrO_2 and TiO_2 powder, PW1b, indicates that a single treatment at 1400°C results in complete conversion to the $Zr_{0.52}Ti_{0.48}O_2$. SEM micrographs (Figure 7) of PW1a and PW1b, which had been milled in IPA after calcination, show that the PW1a powder was reduced to a much finer powder than the PW1b. This indicates that the 1350°C calcination is more desirable to fabricate a friable $Zr_{0.52}Ti_{0.48}O_2$ product. Figure 8 shows a x-ray diffraction pattern of the PW1a powder after it was reacted with PbO at 725°C for 4 h. No diffraction lines from the starting materials are present and only lines from the PZT are found: Thus, the pattern shows a complete reaction to the $Pb(Zr_{0.52}Ti_{0.48})\ O_3$ product, PW1a-1.

Figure 9 shows the sintered densities (%T. D.) of discs prepared from the $Pb(Zr_{0.52}Ti_{0.48})O_3$,PW1a-1 powder which was combined with 2 wt. % excess PbO; 2 wt. % excess PbO plus 0.5 wt. % Ag_2CO_3; and 2 wt. % PbO with 2 wt. % Nb_2O_5. The data show that samples containing the excess PbO and the excess PbO plus Ag_2CO_3 sintered to approximately 100 % T. D. at 1000°C for 1 h. The sample with excess PbO and Nb_2O_5 addition did not reach full density. All the samples sintered at1060°C for 48 h densified to approximately 100 % T. D. Thus, the reactive sintering was helpful in preparing powders, which could be densified at low temperatures. Figure 10 shows results for the d_{33} piezoelectric constant of the sintered discs. The discs sintered at 1000°C for 1 h had very low d_{33} values. The sample with Nb_2O_5 addition could not be poled. The samples sintered at 1060°C for 48 h had higher d_{33} values; however, the sample with the Ag_2CO_3 addition had a lower d_{33} value than commercial material (d_{33} value of 0.3). Figure 11 shows a SEM micrograph of a disc containing 2 wt. % excess PbO and 0.5 wt. % $AgCO_3$ sintered at 1000°C for 1 h. It appears that although the sample is near full density, there is internal porosity and that the grain sizes are smaller than required (> 2 μm) for satisfactory piezoelectric properties.[3] Additional sintering work is necessary to test the usefulness of reactive calcination procedures for fabrication of PZT powders that will sinter well at temperatures less than 1050°C.

The second section of the results involves the use of low expansion PZT precursor, $PbTiO_3$, along with excess PbO for the fabrication of low sintering temperature PZT parts. PZT precursor powders were combined to give a composition of

$(Pb_{0.94}Sr_{0.06})(Zr_{0.53}Ti_{0.47})O_3$, designated PW2. Figure 12 shows x-ray diffraction patterns of discs made from PW2 that were sintered at 1000°C for 1 h or 1250°C for 3 h. This data shows that for both sintering treatments, the precursors were successfully converted to PZT. Figure 13 shows that the 1000°C treatment resulted in a theoretical density of 91 %, and the 1250°C treatment gave a theoretical density of 97 %. In addition, Figure 13 shows d_{33} values for the samples after the two sintering runs. The d_{33} value for the sample sintered at 1000°C was very low; however, the d_{33} value for the sample sintered at 1250°C was good at 0.31 ($x10^{-12}$ m/V). Figure 14 shows the SEM micrographs for samples processed by both sintering runs. Porosity and grains generally less than 5 μm are found in the sample sintered at 1000°C. The 1250°C sample has significant grain growth and less porosity. This fabrication approach offers a much more simple approach to PZT fabrication since there are no intermediate calcination or milling steps required. Additional sintering tests are warranted to see if improved densification and grain growth can be achieved through chemical additions.

Section 3

Task 1

The main task of the project for the last year has been the study of cost-effective alternative PZT compositions and processing methods to allow low temperature (< 1125 °C) sintering of PZT materials. The following work is a continuation of studies on the addition of chemical additives to promote both low temperature densification and grain growth in PZT materials.

Four sample types were made using PZT-4 powder with the following additions: a) none (control), b) 2 wt. % lead oxide (PbO); c) 2 wt. % PbO and 0.1 wt. % silver carbonate (Ag_2CO_3); and d) 2 wt. % PbO and 0.1 wt. % chrome oxide(Cr_2O_3). Additives were mixed with the PZT-4 powder by ball milling for 4 h in water containing 1 wt. % N-(hydroxymethyl)acrylamide and 0.25 wt. % glycerin (based on the total weight of the ceramics). After milling 0.015 g of N,N,N′,N′ tetramethylenediamine (TEMED) and 0.015 g of ammonium persulfate were added to each slurry, which were then heated to boiling rapidly by microwave energy. The gelled powders were dried at 65°C overnight and then milled mill in a 50 cc nylon jar containing two 1 cm diameter partially-stabilized zirconia milling media using a Spex. 5 g samples were die pressed in a 2.8 cm diameter steel die to approximately 70 MPa, heated in air to 600°C for binder burnout, and sintered at 1120°C for 3 h using sintering procedures described in previous reports.

Samples were polished, gold coated, and poled using techniques discussed in Section 1 of this report. The piezoelectric charge constant, d_{33}, was measured 24 h after poling.

Table 1 shows results including green densities, sintered densities, and the d_{33} values obtained for the 4 sample types made in this study. The highest density (97.75 % T. D.) was obtained with the sample containing added PbO and Ag_2CO_3. The sample containing PbO and Cr_2O_3 had the lowest density. All the d_{33} values were low and reflect the fact complete densification was not achieved. It is also felt that the excess lead, which does not significantly volatilize at these low sintering temperatures, may be interfering with the poling process. A follow-up study is underway to make samples, which do not contain excess PbO. Also, longer sintering times will be tested to try to achieve full densification.

Task 2

It is now believed that cost-effective actuators will consist of thin multi-layered PZT structures constructed using tape casting, metal electroding of the PZT via screen printing techniques, and lamination of electroded layers using warm pressing techniques. The present task was initiated to develop the fabrication steps necessary for construction of these multi-layered actuators. The first part of this task is to tape cast PZT-4 material, and to study the lamination of the tapes.

Tape cast materials were fabricated using a Mistler Co. TTC-1000 tape casting machine using basic procedures described in previous reports. The tape slurries consisted of 78.3 wt. % PZT-4, 7.5 wt. % xylene, 7.5 wt. % anhydrous ethanol, 1.0 wt. % menhaden fish oil (Tape Cast Warehouse), 1.6 wt. % butyl benzyl phthalate (Tape Cast Warehouse), 1.6 wt. % polyethylene glycol 400, and 2.5 wt. % polyvinylbutyral (Butvar-98, Monsanto Chemical Co.). Tapes were cast at a speed of 20 cm/min onto a mylar film using a 15.25 cm wide doctor blade adjusted to a thickness of 0.03 cm. The thickness of the dried tapes was ~0.12 mm. A metal punch was used to cut 2.7 cm diameter discs from the tape. The discs were stored in a dessicator separated by wax weighing paper for stable storage.

Laminated tape cast samples were fabricated by uniaxial pressing of 12 to 13 tape discs in a 2.85 cm diameter steel die under the following conditions: die temperature of 60, 70, or 80 °C; pressing pressure of 17.2, 34.5, or 68.9 MPa; and pressing time of 1, 5, or 10 min. Die loading was the fourth variable in this study.

Samples were a) loaded in a pre-heated die at the prescribed temperature and pressed immediately (H/p); b) loaded in a cold die and heated for 45 – 50 min at the prescribed temperature and then pressed (C/rw); or c) loaded into a die at temperature, reheated for 20 – 30 min. to stabilize the temperature and pressed (H/rw). Samples were polished and poled using previously discussed procedures.

The green densities of test samples were measured prior to the binder burn-out process. Samples were placed on tabular alumina powder in an alumina crucible, and binder burn-out conducted in a Neytech box furnace. Laminated discs were heated at 1 °C / min to 225 °C, 250 °C, 275 °C, 300 °C, 350 °C, 400 °C, and 600 °C with a 1 h dwell at each temperature, and then cooled at 10 °C / min to room temperature. PZT samples were placed in alumina setter crucibles, each of which was covered by a second alumina crucible were sintered to 1275 °C for 3 h using methods discussed in Section 1 of this report. Densities of sintered samples were measured by the Archimedes immersion method in absolute ethanol. At this point, discs were subjected to a visual analysis to check for discolorations or irregular appearance and cracks. The discs were given a rating of 1 (bad) to 10 (best), and this was designated as the "quality factor number." Samples were polished, electroded, and poled using methods discussed in previous sections. Electrical measurements were made on the poled discs.

Table 2 shows the $L_9(3^4)$ Taguchi orthogonal array used for the lamination study. A total of 9 lamination trials were needed to test the four experimental variables at three levels. For example, variable 1 is lamination temperature with the three levels being 60, 70, or 80 °C. Taguchi analysis requires averaging of data at a given level, for example 60 °C, and comparing the average data from the other levels, 70 and 80 °C.. Table 3 gives the results of the Taguchi experiment showing the lamination thickness changes, sintered densities, the d_{33} values, and the quality factors for the laminated sintered discs. Figure 15 shows the lamination thickness changes for stacks of discs laminated by the various conditions. Large differences were seen between samples, however measurement errors were present, since it was difficult to press the samples uniformly together while measuring the thickness prior to lamination. Figure 16 shows the final sintered densities of the laminated discs. The differences in the densities of the samples indicate that the densification was greatly affected by the lamination conditions. Figure 17 shows that there was no correlation between thickness changes observed during lamination and the final density. Thus, this analysis will be disregarded in future experiments. Figure 18, a graph of the average density as a function of lamination temperature, shows that there was no clear correlation

between sintered density and lamination temperature, since higher densities were obtained for 60 and 80 °C, and the lowest average density at 70 °C. Figure 19, a graph of the average sintered density as a function of lamination pressure, shows that the lamination pressure has a strong effect in the final densities of the sintered parts. A higher average density was obtained for samples laminated at the lowest pressure. Figure 20, a graph of the average sintered density as a function of the pressing condition, shows the best overall result was obtained with the load cold, heat to temperature, and then press (C/rw) technique. Figure 21, a plot of the average sintered density as a function of the pressing time, shows that that the 5 and 10 minutes pressing times gave the highest average densities.

Only a few d_{33} values were obtained, due to the poor quality of some of the sintered samples and the difficulty in poling these low quality samples. Figure 22 shows that two samples had d_{33} values above 0.3, the manufacturer's listed value. These two samples also had densities above 7.55 g/cm^3. Figure 23, a graph of densities versus quality factors, shows that visual inspection, even though very qualitative, is a fair judge of final density. All samples with high densities also had high quality factors.

A second Taguchi experiment is being conducted to further define the most robust conditions for laminating PZT tape cast materials prepared at Oak Ridge.

References

1. T. R. Shrout, P. Papet, S. Kim, and G.-S. Lee, " Conventionally Prepared Submicrometer Lead-based Perovskite Powders by Reactive Calcination," J. Am. Ceram. Soc., 73 [7], 1862-67, 1990.
2. D. A. Buckner and P. D. Wilcox, "Effects of Calcining on Sintering of Lead Zirconate-Titanate Ceramics," Ceram. Bull., 51[3], 218-222, 1972.
3. N. Ichinose and M. Kimura, " Preparation and Properties of Lead Zirconate-Titanate Piezoelectric Ceramics Using Ultrafine Particles," Jap. J. App. Phys., 30 [9B], 2220-2223, 1991.

Travel

None

Publications

None

Miscellaneous

A draft CRADA document was co-written by Detroit Diesel and the Oak Ridge National Laboratory. Work will proceed following final approvals.

Table 1

Sample Type (PZT-4 +)	BBO Density (%T.D.)*	Sintered Density (%T.D.)	d_{33} (10^{-12}m/V)
2 wt.% PbO	61.7	96.02	0.17
2 wt.% PbO 0.1 wt Ag_2CO_3	62.8	97.75	0.19
2 wt.% PbO 0.1 wt Cr_2O_3	61.4	93.59	0.17
2 wt.% PbO 0.1 wt Ag_2CO_3 0.1 wt Cr_2O_3	62.6	97.55	0.17

Table 2. L_9 Orthogonal Array

Sample#	Temp (C)	P_i (MPa)	Time (min)	Loading
1	60	17.2	1	H/p
2	60	34.5	5	H/rw
3	60	68.9	10	C/rw
4	70	17.2	5	C/rw
5	70	34.5	10	H/p
6	70	68.9	1	H/rw
7	80	17.2	10	H/rw
8	80	34.5	1	H/p
9	80	68.9	5	C/rw

Table 3. Sintered densities, lamination thickness changes, quality factors, and d_{33} values

Sample	Lamination Thickness Change	Density (g/cc)	Qual. Rank	d_{33} 10^{-12}m/V
1	0.35	7.402	5.00	
2	0.37	7.438	5.00	
3	0.43	7.508	7.00	0.277
4	0.45	7.604	8.00	0.300
5	0.59	7.415	4.00	
6	0.40	7.145	2.00	
7	0.35	7.579	7.00	0.368
8	0.48	7.355	4.00	
9	053	7.384	5.00	0.245

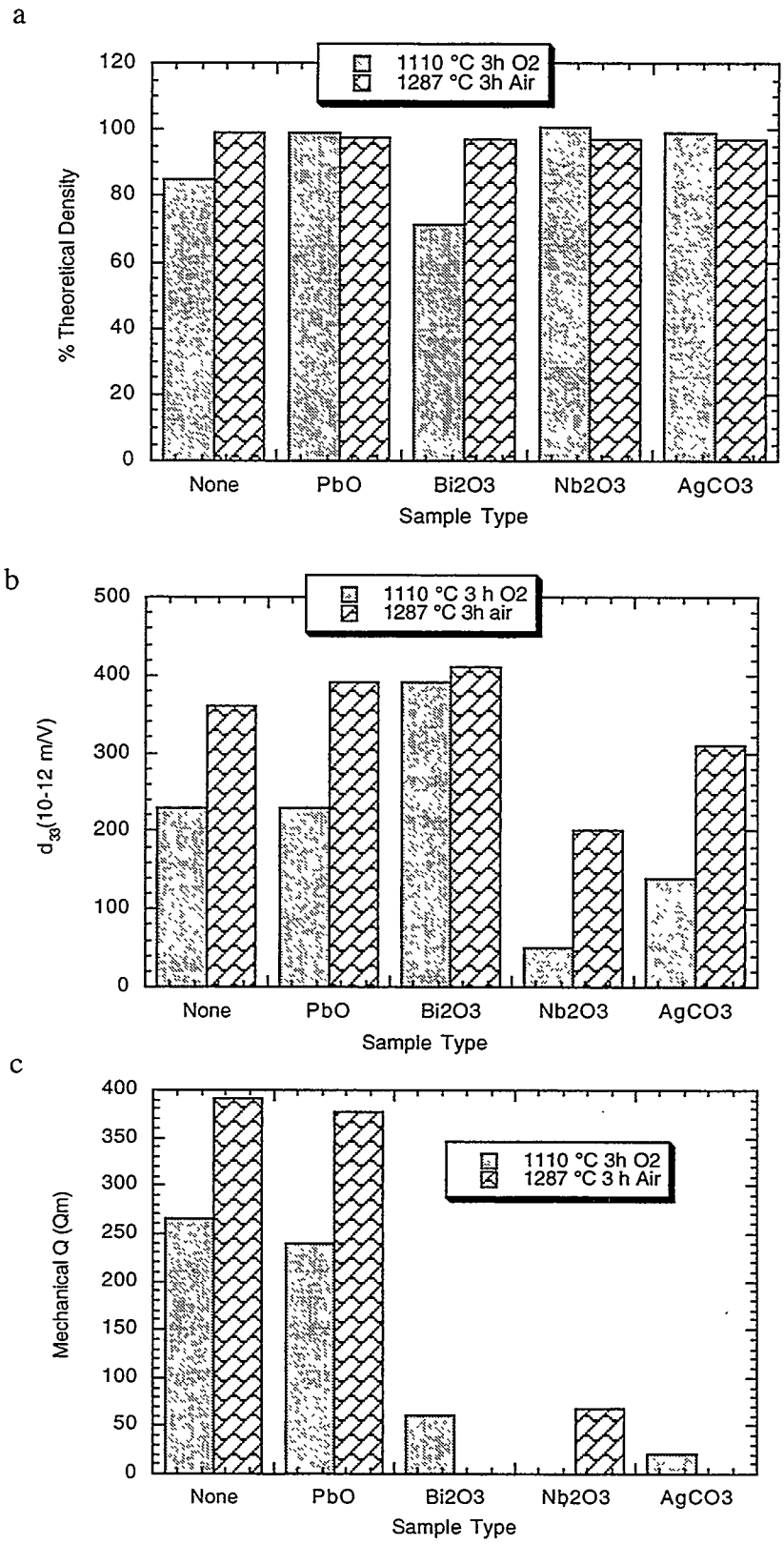

Figure 1. a) % Theoretical densities,b) d_{33} values, and c) Qm values for modified PZT-4 materials sintered at 1110 or 1287 °C.

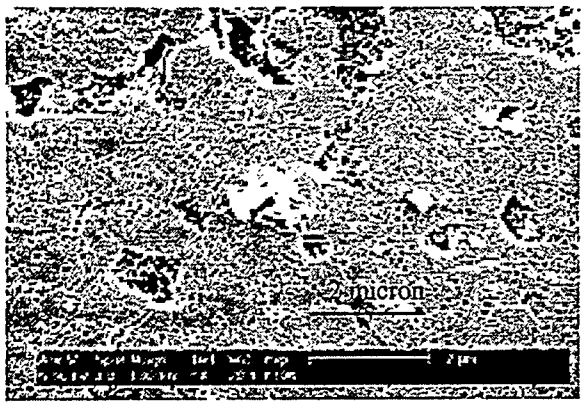

82b - 1110 3h O2 Control 10000X

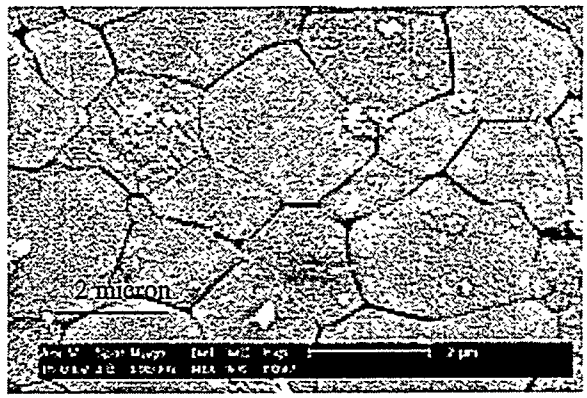

292C - 1287 3h Air Control 10000X

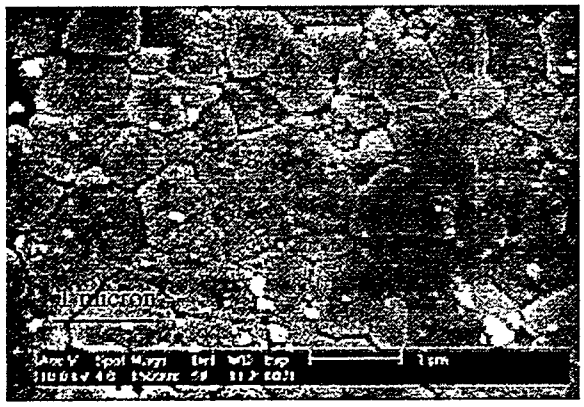

82I - 1110 C 3h O2 PbO 15000X

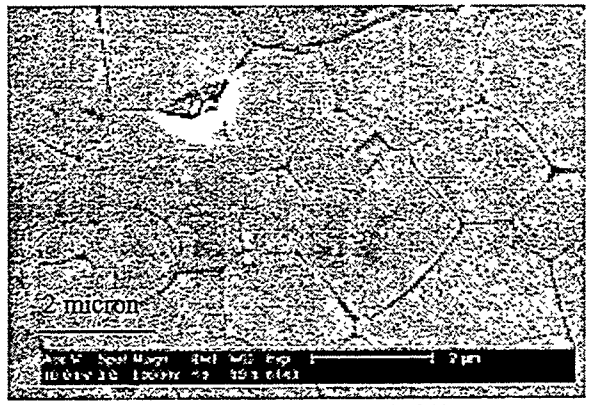

292B- 1287 C 3h Air PbO 10000X

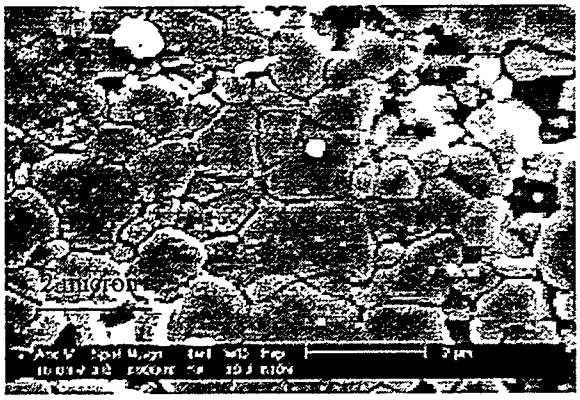

82 H - 1110C 3h O2 2% Silver 10000X

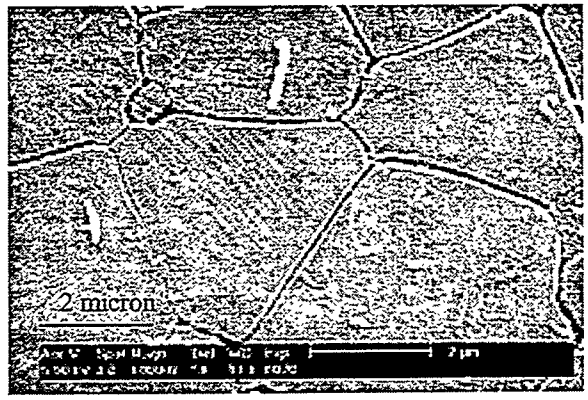

292A -1287 C 3 h Air 2% Ag 10000X

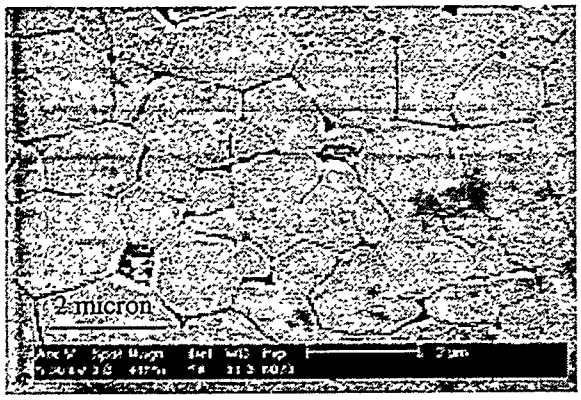

82K - 1110C 3h O2 2%Bismuth 10000X

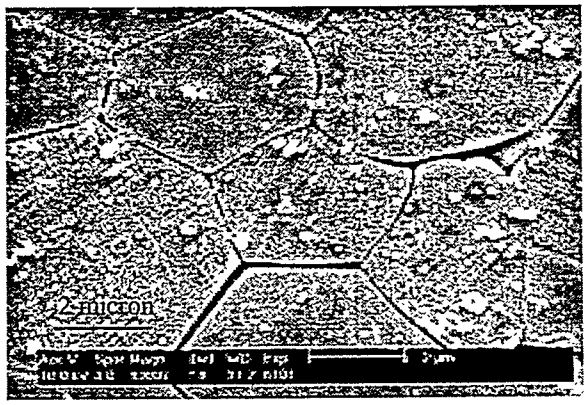

292E- 1287 3H Air 2 % Bismuth 8000X

Figure 2. SEM photographs of PZT-4 materials with added dopants sinterd at 1110 or 1287 °C.

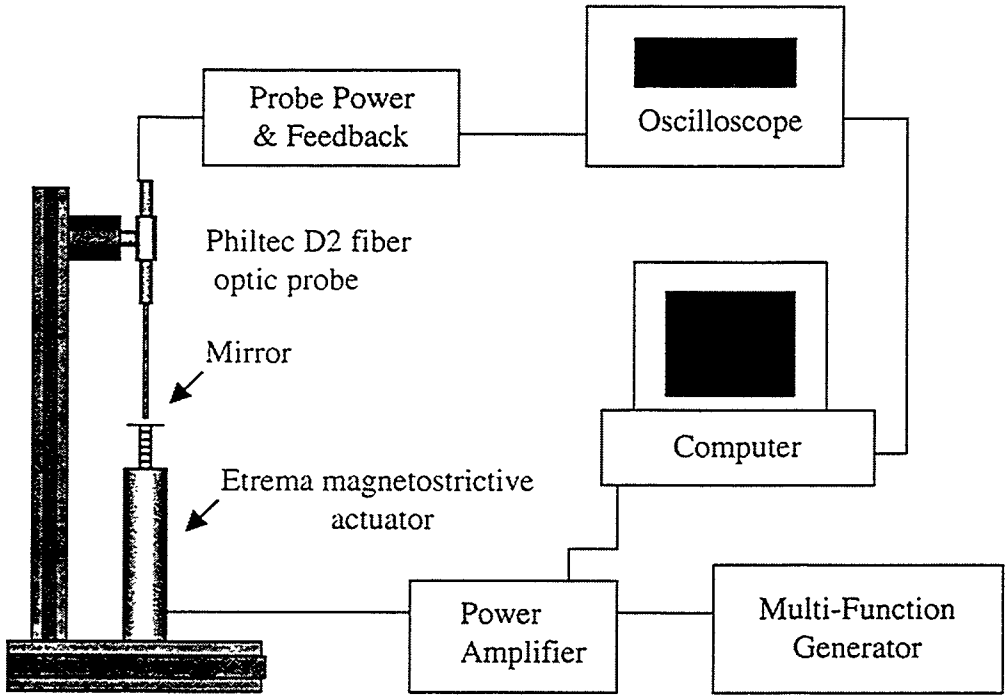

Figure 3. Schematic of magnetostrictive actuator and associated equipment needed to drive and test the actuator.

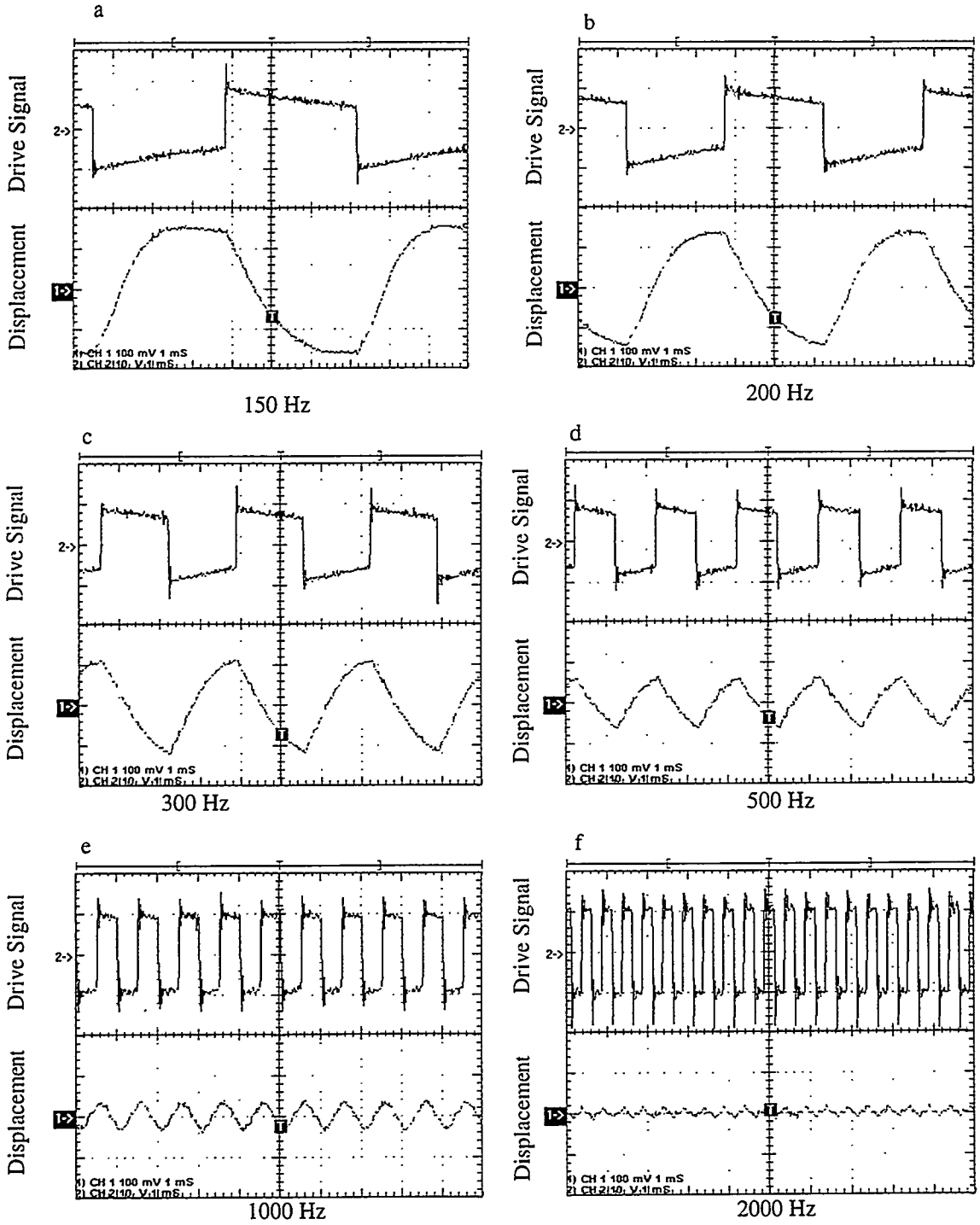

Figure 4. Drive signal - displacement graphs for an Etrema magnetostricive actuator driven at a) 150, b) 200, c) 300, d) 500, e)1000,and f) 2000 Hz frequencies.

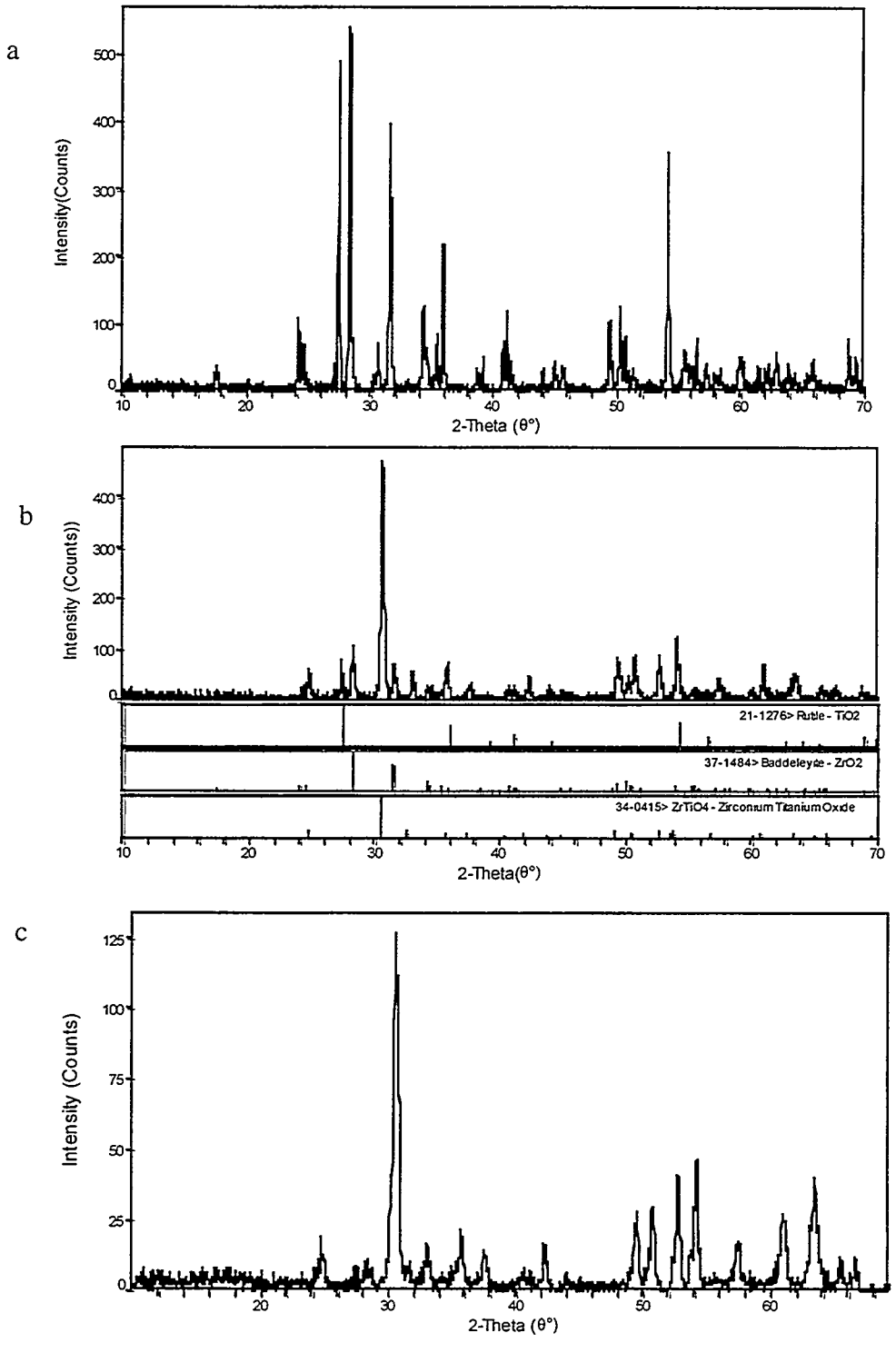

Figure 5. Room temperature X-ray diffraction patterns for ZrO_2 - TiO_2 mixtures calcined at 1250 °C for 4h, b) 1300 °C for 4h, or C) 1300 °C for 8h.

a

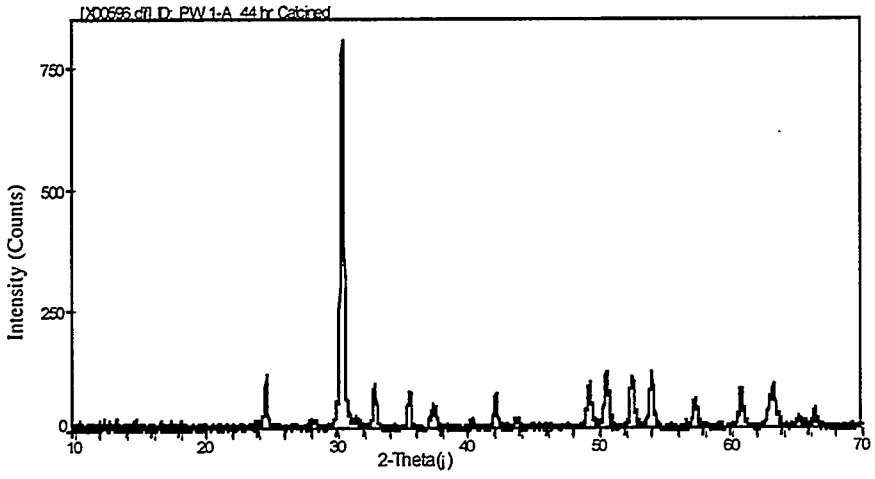

b

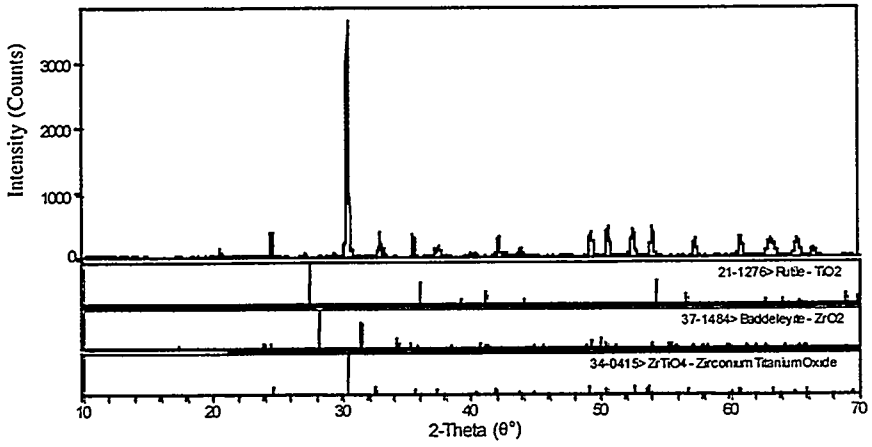

Figure 6. Room temperature x-ray diffraction patterns for a) ZrO_2 - TiO_2 mixtures calcined at 1300°C for 8 h and then at 1350°C for 4 h, b) ZrO_2 - TiO_2 mixture calcined at 1400 °C for 4h.

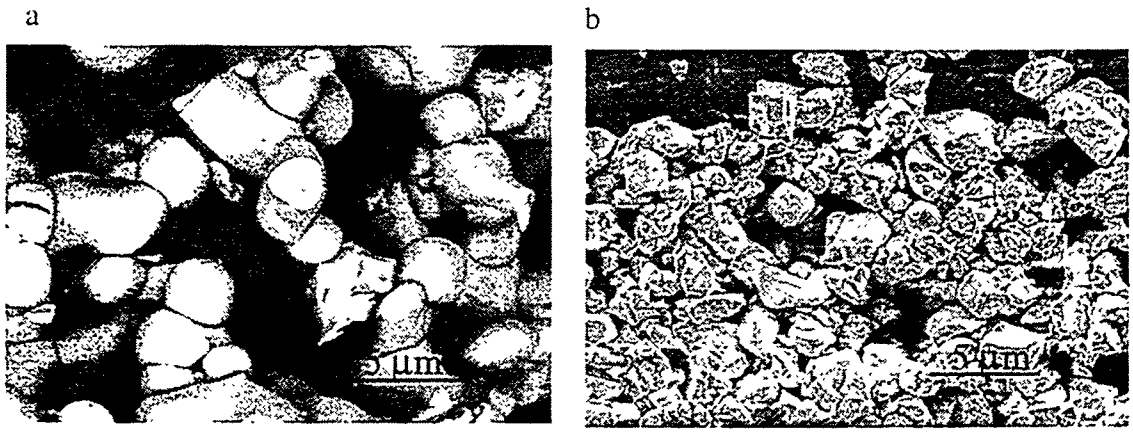

Figure 7. SEM micrographs of $(Zr_{0.52}Ti_{0.48})O_2$ powders produced by calcination of ZrO_2 and TiO_2 powder mixtures at a) 1400°C or b) 1350°C for 4 h.

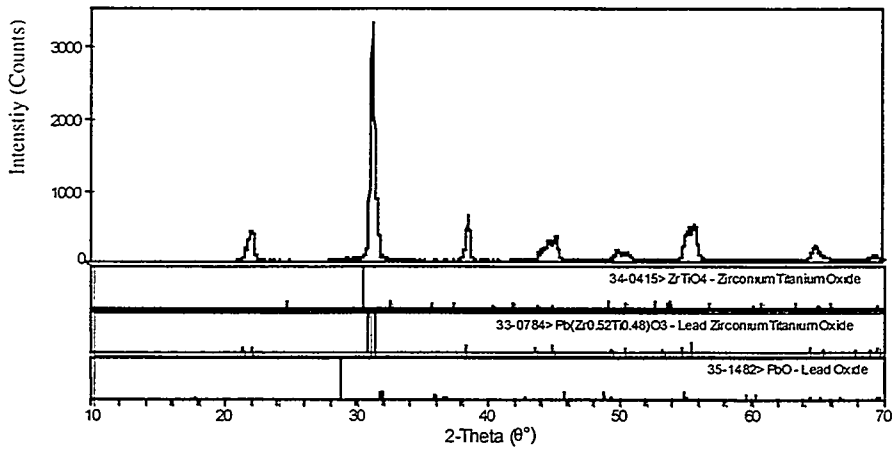

Figure 8. Room temperature x-ray diffraction patterns for $Pb(Zr_{0.52}Ti_{0.48})O_3$ powder fabricated from PbO and $Zr_{0.52}Ti_{0.48}O_2$ powders (1350°C treatment) which were then mixed with PbO powder and calcined to 725°C for 4 h.

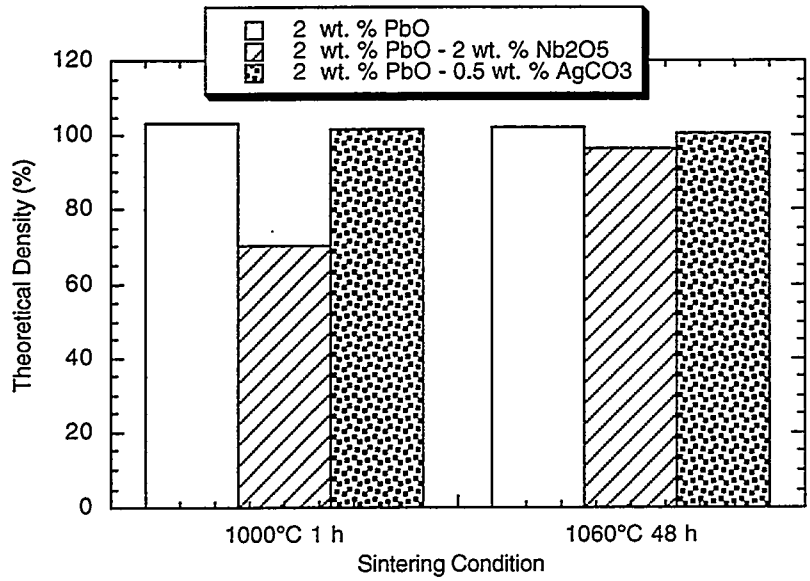

Figure 9. Densities obtained from discs fabricated from PW1a powder containing sintering aides and sintered at either 1000°C for 1 h or 1060°C for 48 h.

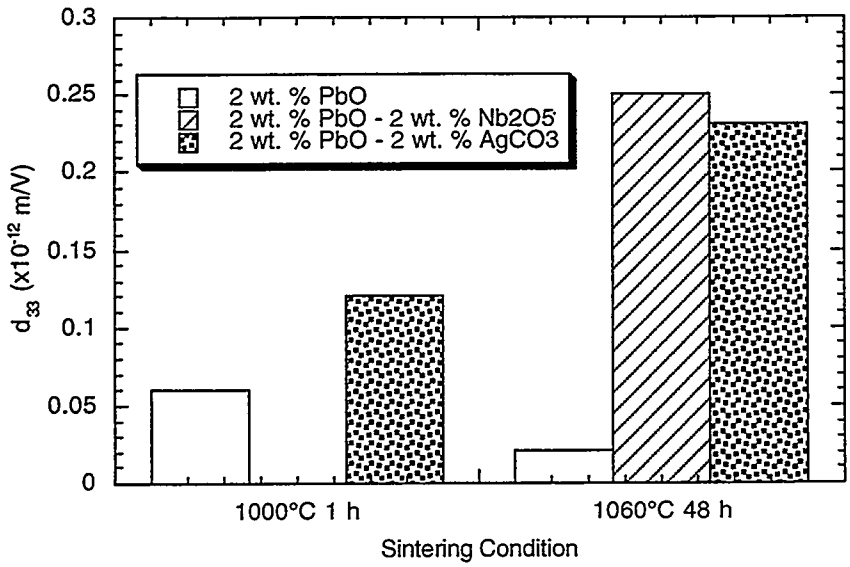

Figure 10. d_{33} values for discs fabricated from PW-1 powders containing sintering aides.

a

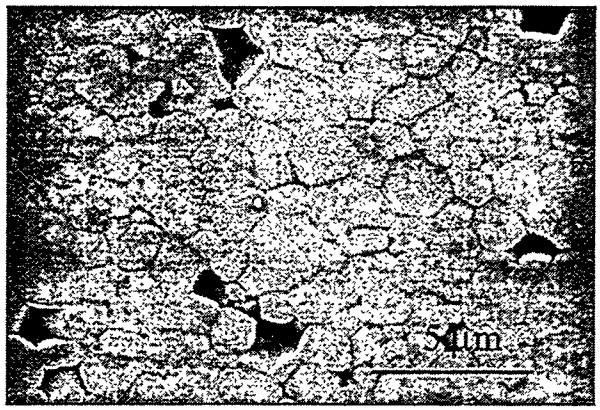

Figure 11. SEM micrograph of a) $Pb(Zr_{0.52}Ti_{0.48})O_3$ with 2 wt% excess PbO and 0.5wt% AgCO3 sintered at 1000°C for 1 h.

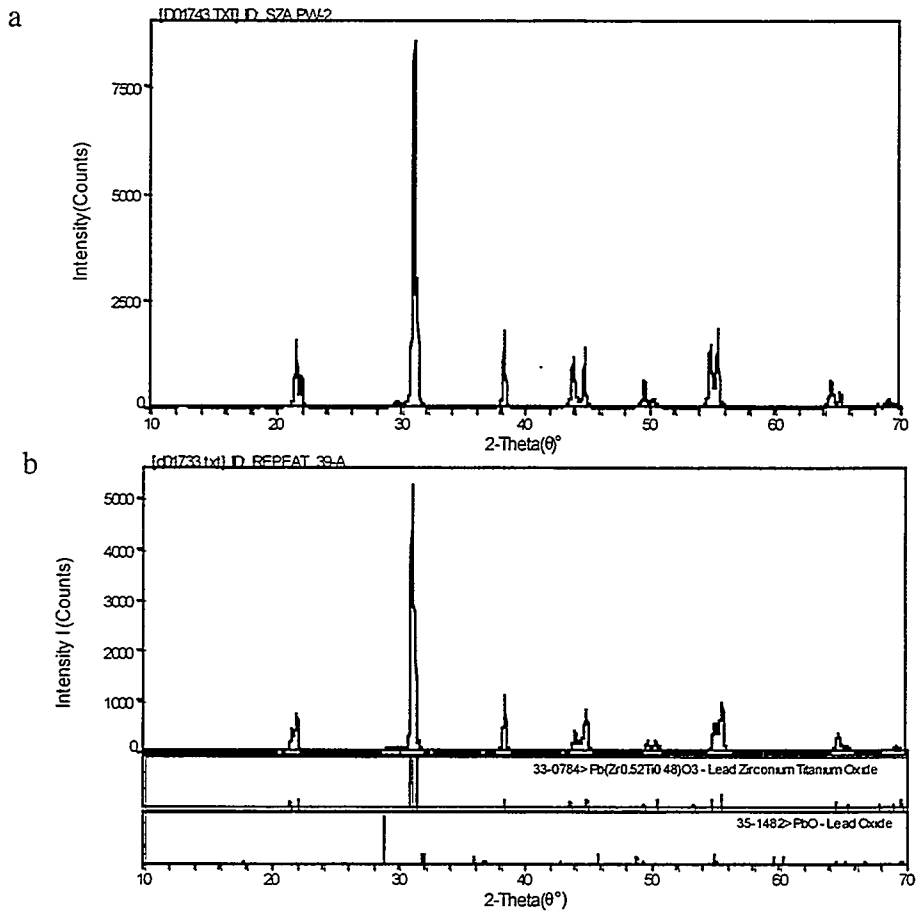

Figure 12. Room temperature x-ray diffraction patterns for $(Pb_{0.94}Sr_{0.06})(Zr_{0.53}Ti_{0.47})O_3$ discs fabricated from PW2 powders and sintered to a)1000°C for 1 h, or b) 1250°C for 3 h.

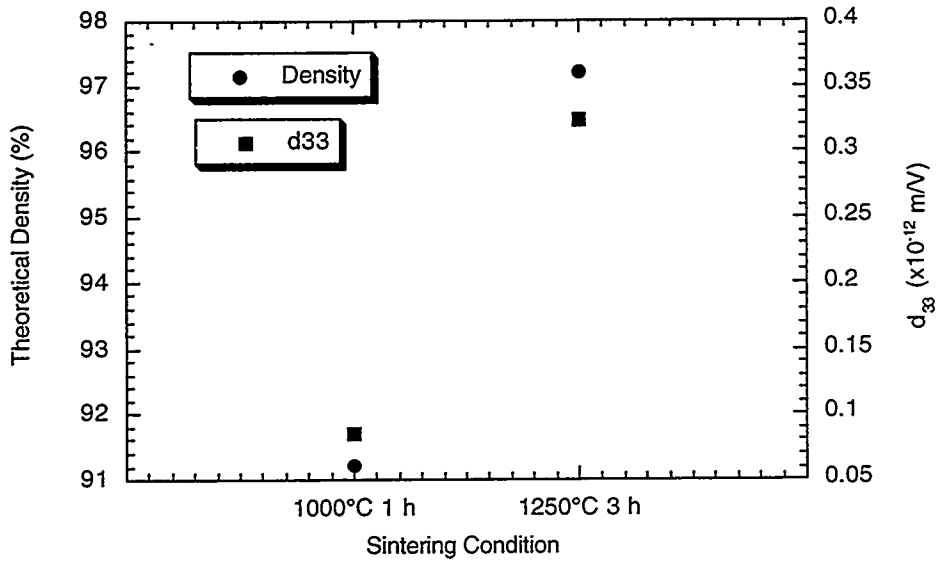

Figure 13. Density and d33 values for discs fabrciated from PW2 powders and sintered at 1000°C for 1 h or 1250°C for 3 h.

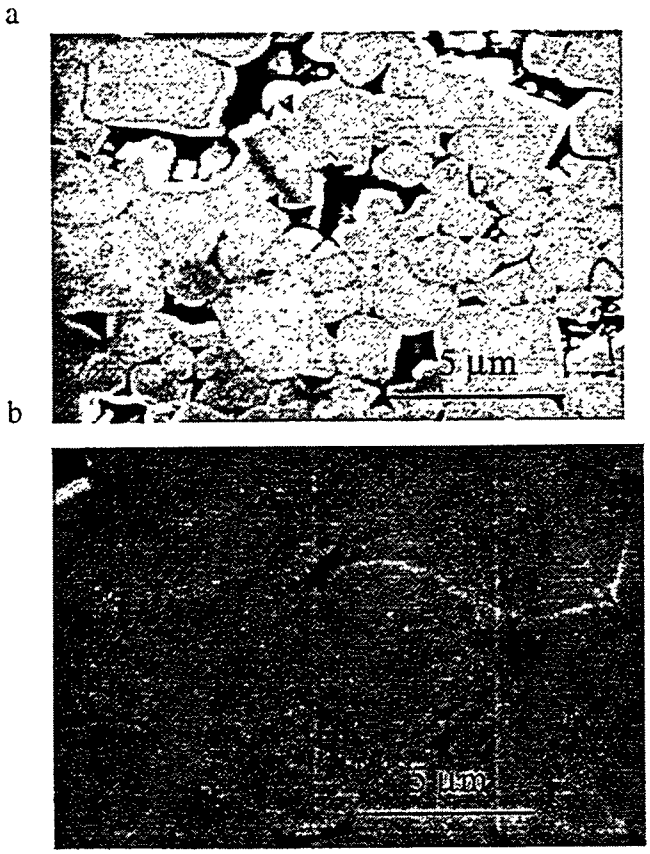

Figure 14. SEM micrographs of a) $(Pb_{0.94}Sr_{0.06})(Zr_{0.53}Ti_{0.47})O_3$ sintered at 1000°C for 1 h, or b) at 1250°C for 3 h.

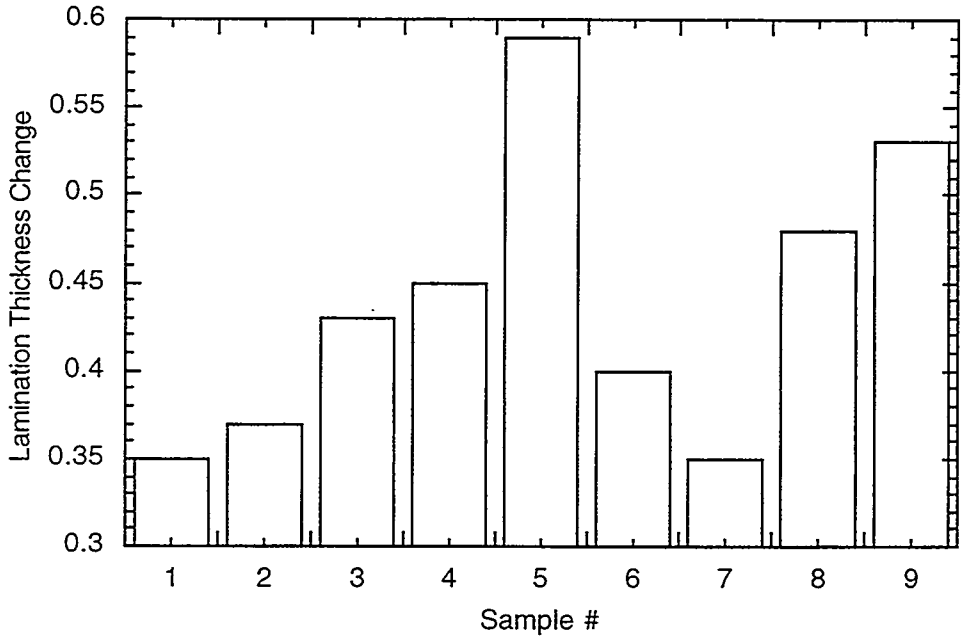

Figure15. Thickness change during lamination of PZT-4 tapes

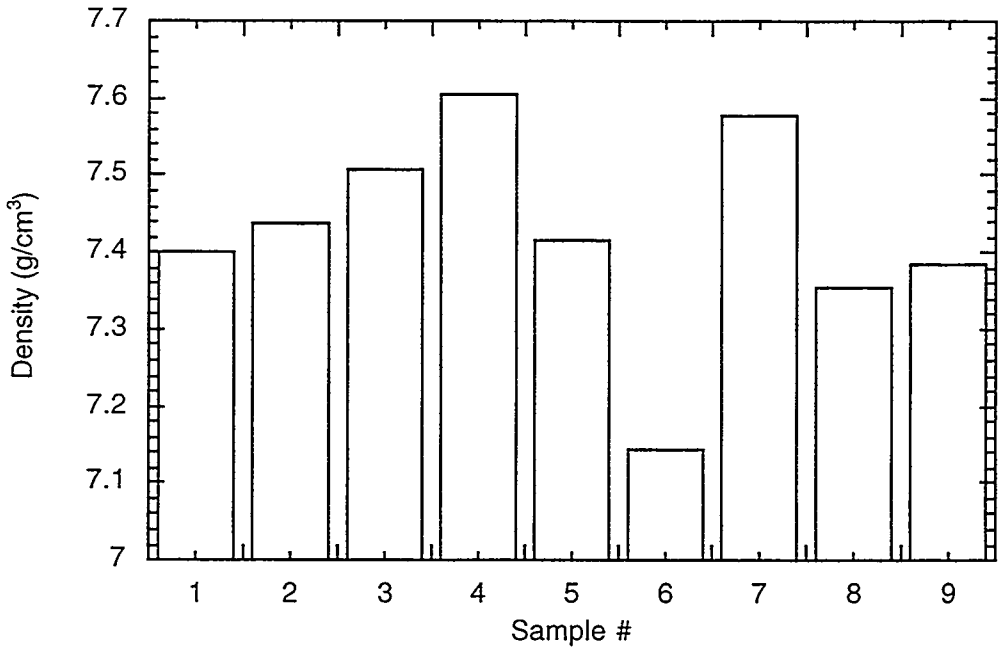

Figure 16. Sintered densities of PZT-4 laminated by different methods

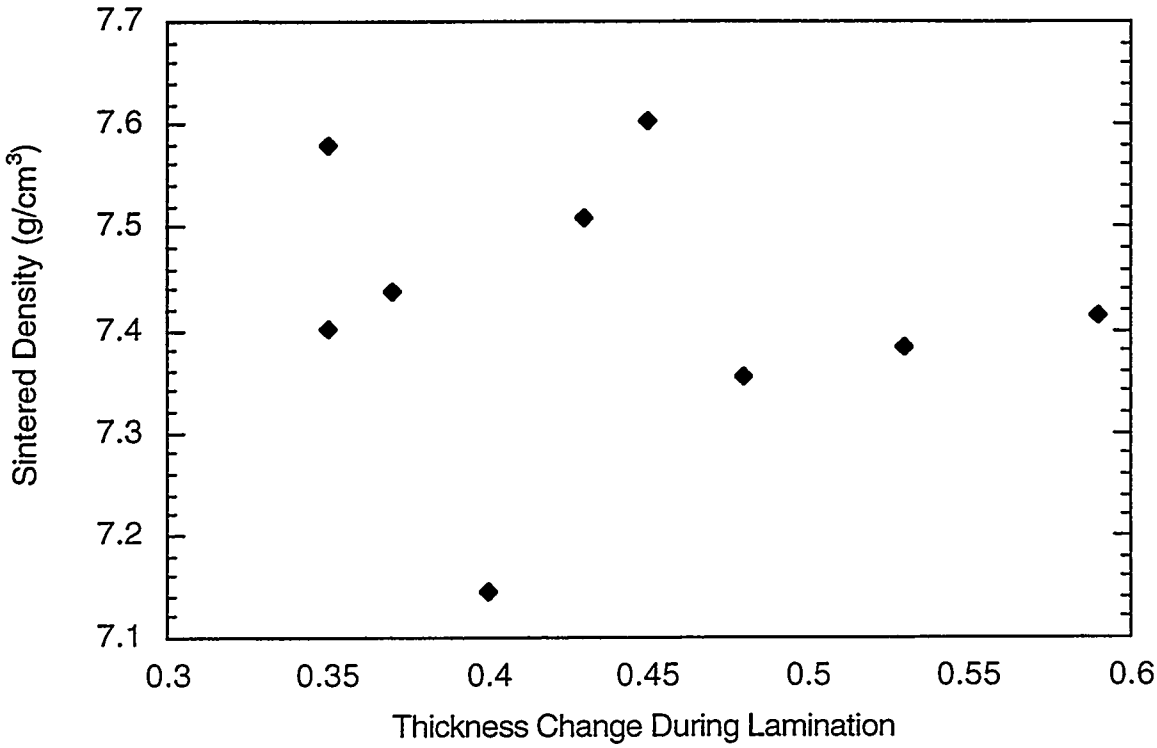

Figure 17. Lamination thickness change as a function of sintered density for PZT-4 laminates.

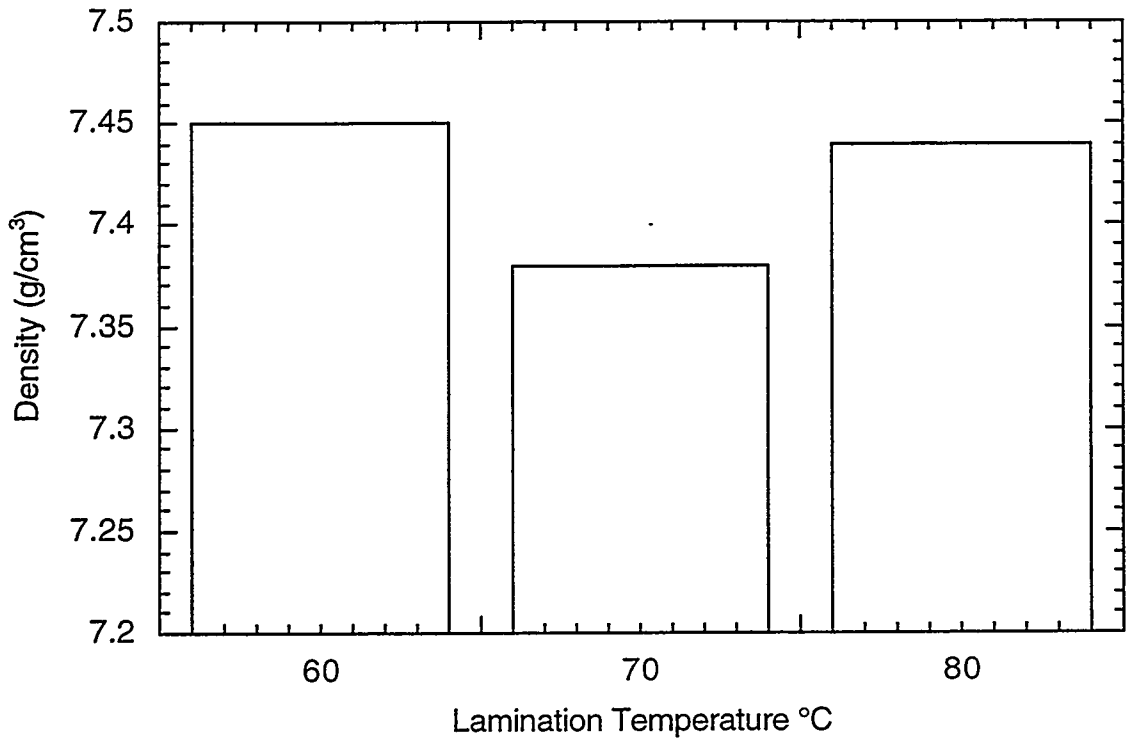

Figure 18. Sintered density as a function of lamination temperature for PZT-4 laminates.

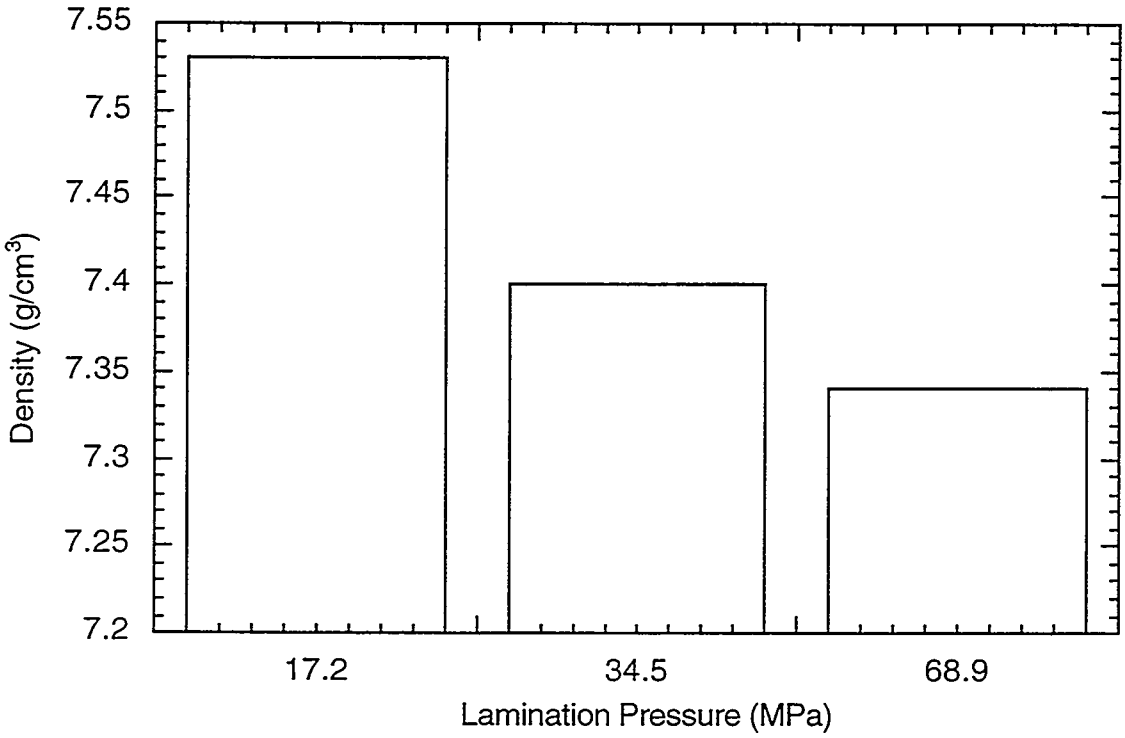

Figure 19. Sintered density as a function of lamination pressure for PZT-4 laminates.

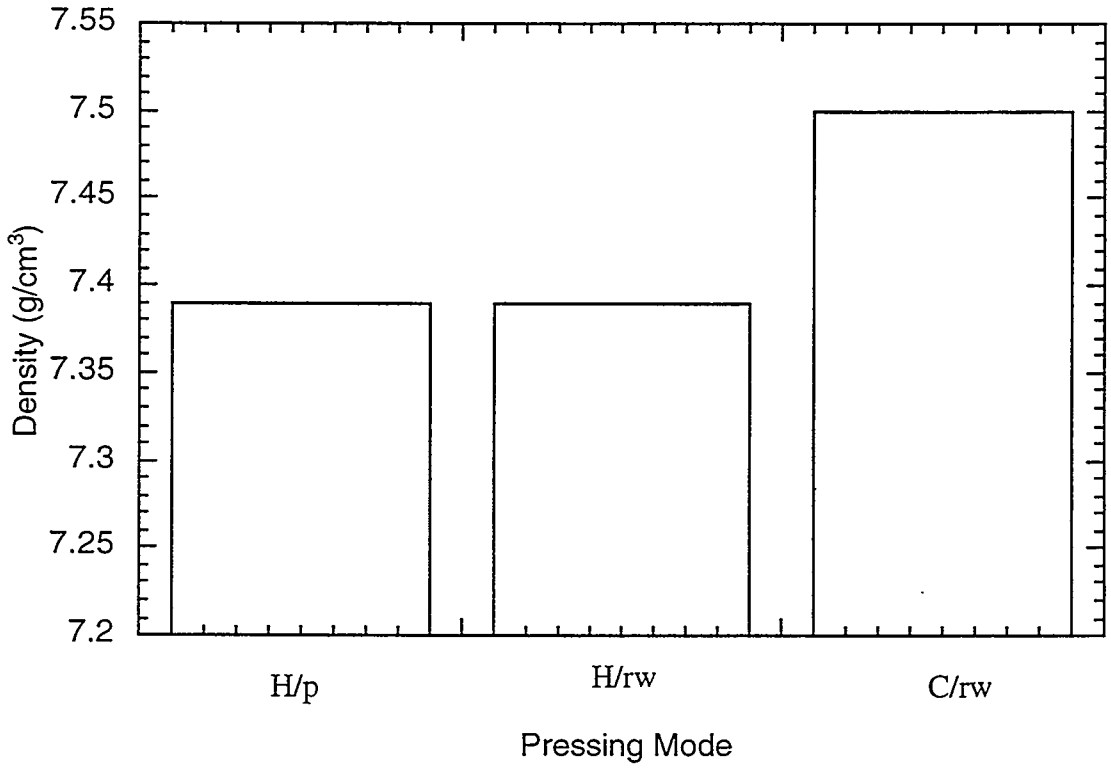

Figure 20. Sintered density as a function of pressing method for PZT-4 laminates.

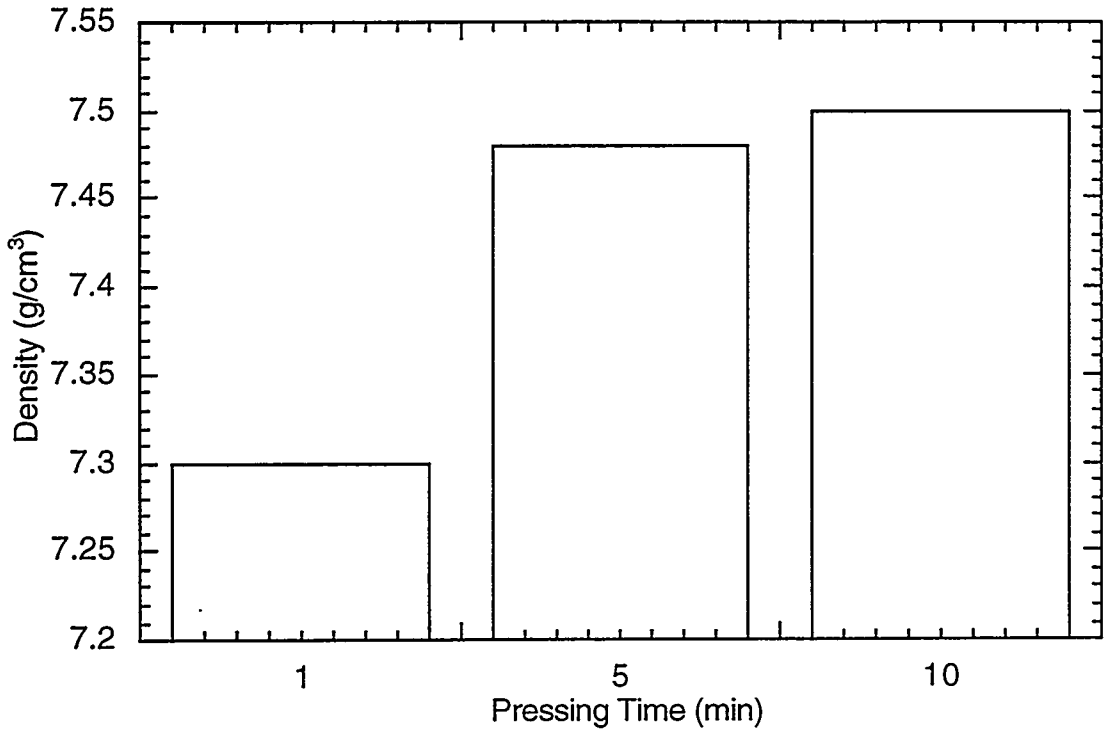

Figure 21. Sintered density as a function of pressing time for PZT-4 laminates.

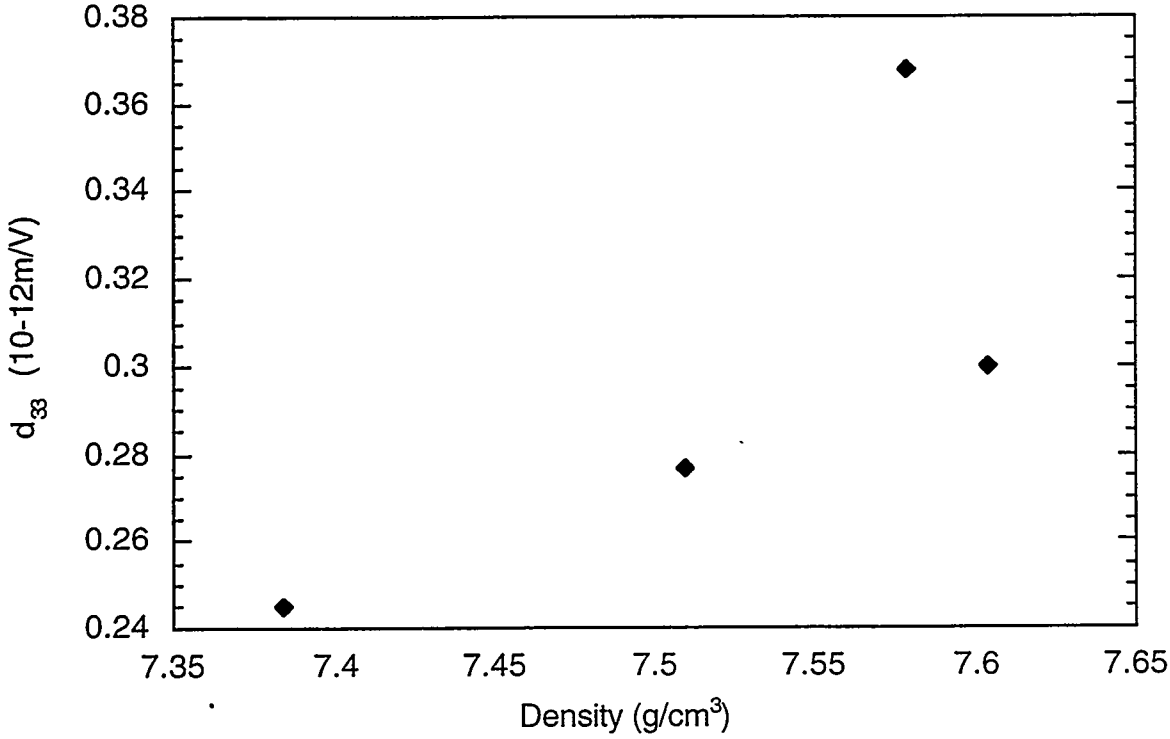

Figure 22. d_{33} values as a function of sintered density for PZT-4 laminates.

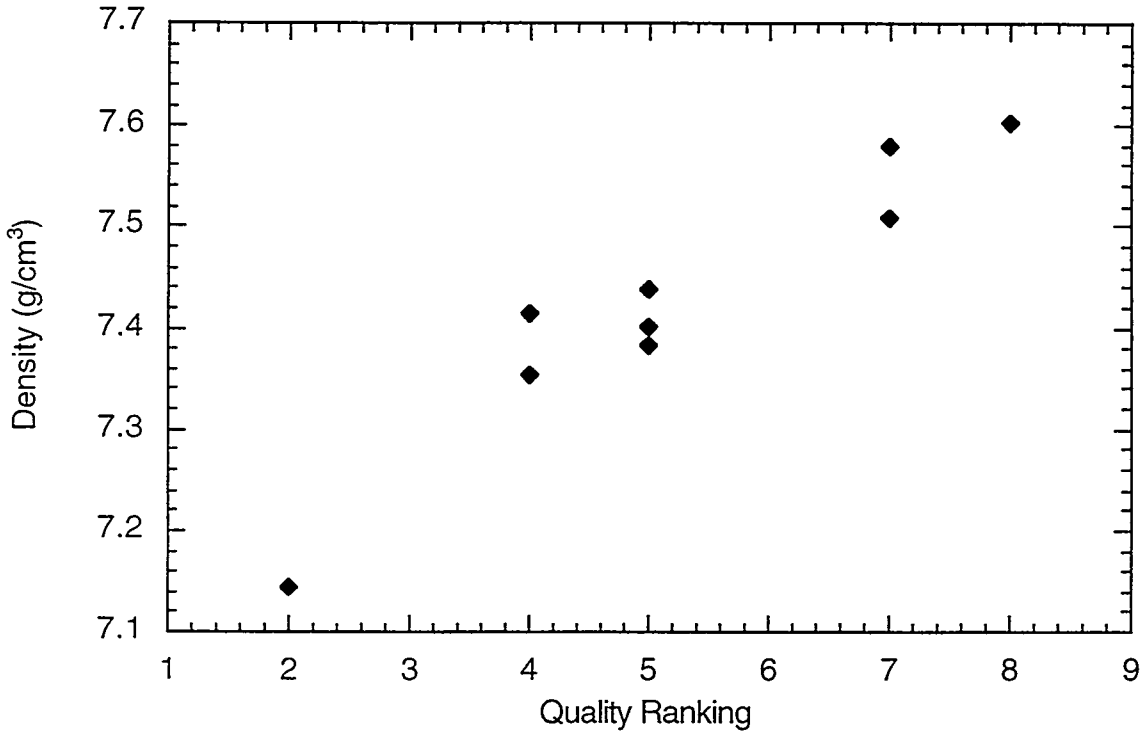

Figure 23. Sintered density versus quality ranking for sintered PZT-4 laminates.

LOW COST-HIGH TOUGHNESS CERAMICS

T. N. Tiegs, F. L. Goransson, F. C. Montgomery, P. A. Menchhofer and D. L. Barker
Oak Ridge National Laboratory
Oak Ridge, TN 37831

Objective/Scope

Significant improvement in the reliability of structural ceramics for advanced diesel engine applications could be attained if the critical fracture toughness (K_{Ic}) were increased without strength degradation. Early results from ORNL research showed that significant increases in fracture toughness could be achieved by manipulating the microstructure to promote toughening mechanisms such as crack bridging. Excellent properties were obtained in this manner for the alumina and mullite matrix systems reinforced with SiC whiskers. In silicon nitride, mechanical property improvements were achieved by promoting acicular or elongated grain growth and these provided significant toughening on the same order as the whisker reinforced materials. Currently, the project is initiating studies on toughening of ceramics by two methods: microstructure development in oxide-based ceramics, and incorporation of ductile intermetallic phases.

Technical Highlights

In-Situ Toughening of Oxide-Based Ceramics by Microstructure Development

Microstructure manipulation has been used to increase the fracture toughness of ceramics for many years. Mainly, this has been done in the silicon nitride-based systems where growth of acicular grains has been encouraged. Recently, oxide-based ceramics have been studied to achieve the same type of results observed with silicon nitride. Thus, because of the large potential, a study was initiated to develop in-situ toughened oxide-based ceramics.

While acicular grains can be grown in oxide-based matrices and modest improvements in toughness can be achieved, strong bonding between grains prevents toughening mechanisms to operate and significantly increase fracture toughness. Therefore, if any improvements in toughness are to be realized in oxides the grain boundaries must be modified so that debonding occurs. At the present time, samples are being fabricated that will test various methods to promote debonding at ceramic interfaces. Two methods will be initially investigated. These are: (1) modification of the matrix-intergranular phase chemistry, and (2) utilization of differences in thermal expansion between phases.

Aluminide-Bonded Ceramics

Previous studies have shown that the properties of the aluminide-bonded ceramics (ABC) are attractive for diesel engine applications and consequently, development of these materials was started. Issues to be studied include the fabrication of parts using cost-effective processing, effect of alloying elements on the properties and fabrication of near-net-shape parts for testing. Initially, a study was done to examine the sintering behavior of the aluminide-bonded ceramics at high binder contents. Most of the previous work on ABC's was done at binder contents of 10-30 vol. %. However, higher binder contents on the order of 30-50 vol. % are necessary for these composites to match the thermal expansion of steel.

Microstructure Development During Sintering - Future development of these materials is expected to involve tailoring of the processing to optimize the properties in composite systems with TiC. Consequently, a detailed study was done to understand the microstructure development during powder processing and sintering of Ni_3Al-bonded TiC cermets. The samples were fabricated by either of two methods: (1) sintering with prealloyed Ni_3Al powder where the alloying additives were

incorporated into the powders prior to gas atomization or, (2) reaction sintering with Ni and NiAl powders to form Ni_3Al in-situ. The results on the densification behavior and properties for the samples have been reported previously.

Microstructure development and densification for the composites occurs by typical liquid phase sintering mechanisms. Liquid formation can occur by the melting of the constituent powders or by reaction between the particles as the temperature is raised. The approximate melting points of the metal powders are: Ni - 1450°C; Ni_3Al - 1380°C; and NiAl - 1640°C. In the Ni-TiC system, a eutectic is predicted at ~1280°C [1]. The DTA results for both the sintering with prealloyed powders and the reaction sintering with elemental powders are shown in Fig. 1. For the prealloyed starting powder, a broad endotherm begins at ~1340°C and a sharp peak is observed at 1360°C corresponding to the melting of the IC-50 Ni_3Al alloy. In the case of the Ni/NiAl starting powders, a minor endotherm at ~1340°C is followed by a stronger one at ~1370°C which are both significantly different from the melting points of the constituents. Thus, in both cases, liquid formation occurs in the range of 1340 to 1370°C even though the starting powders are different.

X-ray analysis of the powders prior to heating and heated to intermediate temperatures reveals the reaction sequence that occurs (Figs. 2 and 3). The as-fabricated prealloyed Ni_3Al-TiC powder mixtures showed broad peaks for the Ni_3Al. This indicates that the Ni_3Al crystal structure of the as-fabricated powders was poorly crystalline and had many defects. In contrast, x-ray diffraction of the as-received Ni_3Al powders showed distinct peaks typical of highly crystalline materials. The change in structure is a result of the Ni_3Al powders being plastically deformed during the milling and mixing processing steps. As the composite powder mixtures are heated to 1200°C and above, the Ni_3Al peaks become narrower and more distinct, indicating recovery and defect elimination. Up to 1300°C there was no indication from the x-ray data of a reaction between the Ni_3Al and the TiC.

The Ni-NiAl powder mixtures for reaction sintering showed sharp peaks for the Ni and broad peaks for the NiAl. As before, the broad peaks indicate the NiAl was poorly crystalline and contained a substantial amount of defects incorporated during milling. After heating to 1200°C, no NiAl is observed. However, Ni_3Al (along with Ni and TiC) is apparent in the x-ray pattern. Evidently, the NiAl reacts readily with the Ni by solid state diffusion to form Ni_3Al well below the formation of any liquid phase. After heating to 1300°C, only Ni_3Al and TiC are observed in the x-ray pattern. From the DTA and x-ray results, the reason why liquid formation is similar between the prealloyed and reaction sintered powders can be explained. In both cases, Ni_3Al is involved and not any precursor. While Ni_3Al is there from the start with the prealloyed powders, the other case involves its formation in-situ at temperatures $\leq$1300°C.

X-ray analysis on the bulk surfaces of the sintered materials showed the presence of only TiC and Ni_3Al (Figs. 4 and 5). The TiC peaks for the materials sintered at 1400°C showed some minor peak broadening which is most likely indicative of the formation of the solid solution with W (from wear of the milling media) and development of the rim structure. At 1500°C, the TiC peaks were better defined, however, the peaks were shifted slightly also indicating the formation of a solid solution.

While the TiC peaks were easily discernible in all the x-ray patterns, the Ni_3Al peaks were quite variable in both width and intensity from sample to sample. The main reason for the broad Ni_3Al peak widths is believed due to the considerable solid solution that can occur in these composite systems. Quantitative EDX of the binder phase for a TiC-50 vol. % Ni_3Al sample fabricated by sintering with prealloyed Ni_3Al at 1500°C (DC-12) showed the following content (atomic %): Ni - 72.40; Al - 24.77; and Ti - 2.83. This corresponds to a composition of $Ni_{2.9}Al_{0.99}Ti_{0.11}$ and indicates the binder composition is altered by solution of the TiC into the liquid phase during sintering. Titanium is supposed to predominantly occupy aluminum sites when it is incorporated into the Ni_3Al structure [2]. However, based on the apparent stoichiometry of the binder, most of the substitution seems to be associated with the Ni sites. Such wide ranging substitutions would account for the broad x-ray peaks observed in the sintered specimens. It should also be noted that

because of the large difference in thermal expansions between the component phases, the Ni_3Al binder is under tension. Such stresses could also contribute to shifts in the observed x-ray patterns.

In general, the strongest Ni_3Al x-ray peaks, as expected, were associated with the samples with the high binder contents. However, in some cases, the Ni_3Al was barely detectable even though appreciable amounts were known to be present (Figs. 4a, 4c, 5a, and 5b). The only plausible explanation for such observations was that the Ni_3Al had some preferred orientation in the specimens that could be affecting the reflection intensities. X-ray patterns from the same specimen (DC-15) were taken both parallel and perpendicular to the thickness direction (Fig. 6). As shown, a significant difference in the Ni_3Al peak intensities is apparent. To estimate the degree of preferred orientation, rocking scans were performed at the Ni_3Al peak of $2\theta = 43.5°$. In a rocking scan, the specimen is rotated through the Bragg angle, while both the x-ray source and detector stay fixed. A rocking scan from a thick sample that possesses randomly oriented small grains is a continuous gaussian-shaped curve with a maximum intensity located at $2\theta/2$. The width of this rocking curve is a direct measure of the range of orientations of the grains within the irradiated area of the sample. Preferred orientation is evident when 'jagged saw-tooth' features are observed. The results, shown in Fig. 9 indicate the existence of some possible preferred orientation of the Ni_3Al. In particular, the rocking scans shown in Figs. 7a and 7d both exhibit varying x-ray intensity signifying some orientation is present. The pointed features in Figs. 7a and 7d are too broad to be from a single large grain and thus probably originate from a subset of grains or subgrains with their reflecting planes oriented about 7° away from the surface normal. In the case of the other rocking scans, the results were mixed. The specimen sintered at 1400°C (DC-15-2, Fig. 7b) reveals no apparent orientation effects, although the low count rate over the entire scan may have contributed to that observation.

Orientation effects can be caused by several morphologies, but one of the most common is the occurrence of large grains in the microstructure. Etching of the samples to determine the Ni_3Al grain size was inconclusive because of the difficulty in distinguishing the grain boundaries. However, optical observations at low magnification indicated that the Ni_3Al grains were quite large, on the order of millimeters, and extended over significant areas. This insinuates that the Ni_3Al grains encompass a multitude of TiC grains and are macro-features in comparison to the TiC. Although little information is available, grain sizes for the binder phase in WC-Co hardmetals have also been reported to be on the order of millimeters [3,4]. In addition, analogous microstructures have been observed in liquid phase sintered silicon nitride ceramic materials, where complex silicates, derived from the sintering additives, have been reported to extend over considerable distances (millimeters) and encompass multitudes of much smaller ß-Si_3N_4 grains [5].

The microstructures of TiC-40 vol. % Ni_3Al sample fabricated by sintering with prealloyed Ni_3Al (DC-10) and reaction sintered with Ni/NiAl mixtures are shown in Figs. 8 and 9, respectively. For both sintering routes, the TiC particles exhibit a 'core-and-rim' morphology caused by reaction of the liquid Ni_3Al with the TiC. Such 'core-and-rim' structures have been observed previously in TiC-Ni cermets. Energy dispersive x-ray (EDX) analysis of the core-rim structure revealed several observations that were similar to previous results on TiC-Ni-Mo cermets [3,6]. The central core region consists of the original TiC with no detectable other components. In the rim region, W was the major additional species observed and in most cases was the only other element present besides Ti and C. The W is from the wear of the milling media during processing. Wear of the media, as mentioned previously, contributed ~0.4 wt. % WC to each of the compositions. Preferential accumulation of the W in the rim structure on the TiC has been observed in other studies [3]. In some samples examined, Ni and Al were also observed near the outer regions of the rim structure. Generally, the Ni and Al were observed in the rim structure mainly in the reaction sintered specimens. Previous studies have shown that in some TiC-based cermets, the rim area can be divided into two parts [7,8]. An interior part that was developed during solid state diffusion and sintering, and an exterior part that is formed during liquid phase sintering and reprecipitation during cooling. Using that analogy, for the present TiC-Ni_3Al-(W) materials, the W is believed to diffuse readily into the TiC during the sintering cycle and probably reaches an equilibrium composition for

the (Ti,W)C solid solution. The Ni and Al get incorporated into the exterior rim region during reprecipitation onto the TiC particles during cooling. Additional detailed studies need to be performed to reach any definitive conclusions.

The effect of temperature and Ni_3Al content on the final grain size is shown in Fig. 10. As expected, larger grain sizes were noted at higher sintering temperatures and larger Ni_3Al contents. Interestingly, the reaction sintered materials had smaller grain sizes than the composites fabricated with prealloyed powders. Since time in the presence of the liquid phase was similar in both cases, the difference in grain size can be attributable to only a few possible differences: (1) solubility of the TiC; (2) diffusion in the liquid phase; or (3) kinetics of solution and reprecipitation at the TiC interface. The only significant difference between the Ni_3Al in the prealloyed versus the reaction sintered materials is the 0.6 wt. % Zr in the prealloyed powder. This small amount of Zr should have only a minor effect on the solubility of TiC and diffusion in the liquid phase. However, the Zr would act as a powerful oxygen getter in the system due to the high free energy of formation and stability of ZrO_2. This oxygen gettering could significantly influence the wetting between the TiC and the liquid phase and thus affect the solution-reprecipitation kinetics. Small amounts of surface oxygen are well known to adversely affect the wetting between carbides and molten metals and in a similar fashion, minor additions of Mo to Ni have been shown to reduce the contact angle with TiC from 17° to 0° [9-11].

The high temperature properties of these composites were measured and are summarized in Fig. 11. As shown, the materials using the prealloyed Ni_3Al exhibited good strength retention or strength improvements up to temperatures of 800°C. The reaction sintered materials, while having lower strength at room temperature, showed significant improvement at the elevated temperatures.

Effect of Ni_3Al Alloying Additives and Grain Refinement - Earlier work showed that the alloying additives affect the sintering behavior and properties of the aluminide bonded ceramics. Consequently, a series of samples was fabricated to determine the effect of alloying additives on the sintering behavior and properties of the aluminide-bonded TiC as indicated in Table 1. The results on the densification behavior, indent fracture toughness and indent hardness have been reported previously.

Large specimens were fabricated and machined into mechanical test specimens. The results on the room temperature flexural strength are summarized in Fig. 12. As shown, the strengths are relatively low compared to others reported previously for the TiC-Ni_3Al composites. However, these samples were fabricated by reaction sintering of elemental powders and the strengths for those types of composites are generally lower. DC-13 is the baseline reaction sintered material with no alloying additions. The only sample that showed any appreciable strength increase was the one containing appreciable amounts of Fe substitution (DC-25). The strengths at temperatures $\leq$800°C are shown in Fig. 13. As expected, increased strengths were observed at temperatures up to 500°C. At 800°C, significant decrease in strength was associated only with DC-25 containing large substitution of Fe into the binder phase.

The fracture toughness (by an indentation and fracture method) and hardness as measured on ground surfaces of the specimens are shown in Figs. 14 and 15, respectively. The fracture toughness was highest for the compositions containing Fe at various contents. Substantial toughness improvements were associated with the addition of Fe (Composition DC-25, $Ni_{1.50}Fe_{2.00}Al_{0.50}$). The toughness values were generally ~10 MPa$\sqrt{m}$ and confirms the excellent resistance to crack growth for these types of composites. As indicated, the hardness was generally in the range of 8 to 11 GPa. When examining the effect of the additive type, the highest hardness values were associated with the additions of Cr, Si, Mo, W and Co. This indicates the solid solution hardening effects of the alloy additions.

For certain applications, it is desirable that the grain size of the TiC be as small as possible. Attritor milling is a high energy process capable of fine grinding of the starting TiC powders. A

preliminary milling study to determine particle size reduction behavior was done and is summarized in Fig. 16. Two different milling media types were chosen. The zirconia media (3 mm diameter and milling at 500 rpm) showed greater TiC particle reduction than the tungsten carbide media (6.5 mm diameter and milling at 350 rpm). TiC powders produced by these conditions are being fabricated into Ni_3Al-based composites to determine the effect on grain size reduction in the sintered materials.

Previous work on hot-pressed materials showed that alloy type affects the properties of the composites. A series of specimens was fabricated to determine the sintering behavior and properties of TiC-40 vol. % Ni_3Al as shown in Table 2. The densification behavior of these materials is summarized in Fig. 17. At 1400°C, the non-aluminide alloys (NiCr and NiCrFe) produced composites with high densities. Inhibited densification was noted only for the composite utilizing IC-396M as the binder phase. This alloys contains significant amount of Mo which may decrease the densification. The mechanical properties will be determined for these samples.

Conventional TiC-based cermet processing uses other carbide additions to aid in densification and also to maintain small grain size. Several carbide additions were tested as shown in Table 3. The substitution was made on the basis of a 10 vol. % replacement of the TiC. The densification behavior is shown in Fig. 18. Only the Mo_2C addition appeared to significantly inhibit sintering. The mechanical properties will be determined for these samples.

Microstructure characterization of these samples revealed a core-rim structure very similar to ones described previously for other TiC-Ni_3Al composites. (Fig. 19). Energy dispersive spectroscopy (EDS) of the elemental distribution showed different behavior for the alloying additives. When Zr or Mo are included with the Ni_3Al alloy, they preferentially get incorporated into the rim structure along with the TiC during precipitation on the pure remnant TiC cores. Even though Zr and Mo are added in the alloy, none was observed remaining in the binder phase. On the other hand, when Cr is part of the Ni_3Al alloy, it resides in the rim structure and also in the Ni_3Al binder phase. Evidently, the Zr and Mo are strong enough carbide formers to predominate during precipitation of the TiC and are taken out of the liquid Ni_3Al. Conversely, the Cr is not as strong a carbide former and thermodynamically is stable in the binder phase.

Status of Milestones

On schedule.

Communications/Visits/Travel

Travel by T. N. Tiegs to attend the American Ceramic Society Annual Meeting in Indianapolis, IN, April 25-28, 1999.

Travel by T. N. Tiegs to attend the International Conference on Powder Metallurgy and Particulate Materials, Vancouver, BC, June 20-24, 1999 and present a paper entitled, "Microstructure Development During Sintering of TiC-Ni_3Al Cermets."

A CRADA was established with Coors Ceramics to investigate grain refinement in the TiC-Ni_3Al composite system.

Problems Encountered

None.

Publications

T. N. Tiegs, J. L. Schroeder, F. C. Montgomery, and D. L. Barker, "Microstructure Development During Sintering of TiC-Ni_3Al Cermets," to be published in Proceedings of International Conference on Powder Metallurgy and Particulate Materials, Vancouver, BC (1999).

References

1. Phase Equilibrium Diagrams, Vol. 10, A. E. McHale (ed.), Fig. 9017, pp. 345, Am. Ceram. Soc., Westerville, OH (1994).

2. C. T. Liu and J. O. Stiegler, "Ordered Intermetallics, ASM Handbook, Vol. 2, pp. 913-942, ASM Internat., Metals Park, OH (1990).

3. P. Ettmayer, "Hardmetals and Cermets," Annual Rev. Mater. Sci., Vol. 19, 145-164 (1989).

4. A. Doi, T. Nishikawa, and A. Hara, pp. 329-340 in Science of Hard Materials, R. K. Viswanadham, D. J. Rowcliffe, and J. Gurland (eds.), Plenum Press, New York (1983).

5. M. H. Lewis, "Crystallization of Grain Boundary Phases in Silicon Nitride and Sialon Ceramics," pp. 217-231 in Tailoring of Mechanical Properties of Si_3N_4 Ceramics," M. Hoffmann and G. Petzow (eds.), Kluwer Academic Pub., Boston, MA (1994).

6. J. K. Yang and H.-C. Lee, "Microstructure Evolution During the Sintering of a Ti(C,N)-Mo_2C-Ni," Mater. Sci. Eng., Vol. A209, No. 1-2, 213-217, (1996).

7. H. Yoshimura, T. Sugizawa, K. Nishigaki, and H. Doi, Int. J. Refractory Metals and Hard Metals, 33 [4] 170-174 (1983).

8. R. Warren, J. Mater. Sci., Vol. 3, 471-485 (1968).

9. L. S. Williams and P. Murray, "Bonding in Cermets," Metallurgia, 49, 210-217 (1954).

10. M. Humenik and N. M. Parikh, "Cermets and Physical Properties of Cermet Systems," J. Am. Ceram. Soc., 39, 61-62 (1956).

11. M. Humenik and T. J. Whalen, "Physiochemical Aspects of Cermets," pp. 6-49 in Cermets, Reinhold, New York (1960).

Table 1. Samples of aluminide-bonded TiC ceramics fabricated to determine the effect of alloying additives on the sintering behavior and properties of the aluminide-bonded TiC. All samples fabricated with 30 vol. % of the Ni_3Al binder phase by reaction sintering of elemental powders.

Specimen No.	Binder Composition	Substitution Site of Alloying Element
DC-22	$Ni_{2.85}Fe_{0.15}Al_{1.00}$	Both Ni and Al
DC-23	$Ni_{2.85}Fe_{0.20}Al_{0.95}$	Both Ni and Al
DC-24	$Ni_{2.40}Fe_{0.80}Al_{0.80}$	Both Ni and Al
DC-25	$Ni_{1.50}Fe_{2.00}Al_{0.50}$	Both Ni and Al
DC-26	$Ni_{2.85}Cr_{0.20}Al_{0.95}$	Both Ni and Al
DC-27	$Ni_{2.40}Cr_{0.80}Al_{0.80}$	Both Ni and Al
DC-28	$Ni_{3.00}Si_{0.20}Al_{0.80}$	Al Sites
DC-29	$Ni_{3.00}Ti_{0.20}Al_{0.80}$	Al Sites
DC-30	$Ni_{3.00}Mo_{0.20}Al_{0.80}$	Al Sites
DC-31	$Ni_{3.00}W_{0.20}Al_{0.80}$	Al Sites
DC-32	$Ni_{2.40}Co_{0.60}Al_{1.00}$	Ni Sites
DC-33	$Ni_{3.00}Zr_{0.20}Al_{0.80}$	Al Sites

Table 2. Samples of aluminide-bonded TiC ceramics fabricated to determine the effect of Ni_3Al-binder composition on the sintering behavior and properties of the aluminide-bonded TiC. All samples fabricated with 40 vol. % of the Ni_3Al binder phase by sintering of prealloyed powders.

			Binder Composition (wt. %)				
Sample ID	Binder Type	Particle Size (μm)	Al	Zr	Cr	Mo (or Fe)*	B
DC-43B	IC-50	<65	11.3	0.6	--	--	0.02
DC-44	IC-218	<44	8.7	0.2	8.1	--	0.02
DC-45	IC-264	<44	8.4	1.7	7.8	--	0.02
DC-46	IC-396M	<65	8.0	0.9	7.7	3.0	0.01
DC-53	NiCr	44-100	--	--	20	--	--
DC-54	NiCrFe	<44			14-17	6-10*	--

Table 3. Samples of aluminide-bonded TiC ceramics fabricated to determine the effect of different carbide substitutions on the sintering behavior and properties of the aluminide-bonded TiC. All samples fabricated with 40 vol. % of the Ni_3Al binder phase by sintering of prealloyed powders. The different carbides were substituted on the basis of 10 vol. % of the TiC.

Sample ID	Carbide Substitution
DC-43B	--
DC-50	TaC
DC-51	VC
DC-52	$Cr_{23}C_6$
DC-57	Mo_2C
DC-58	TiN

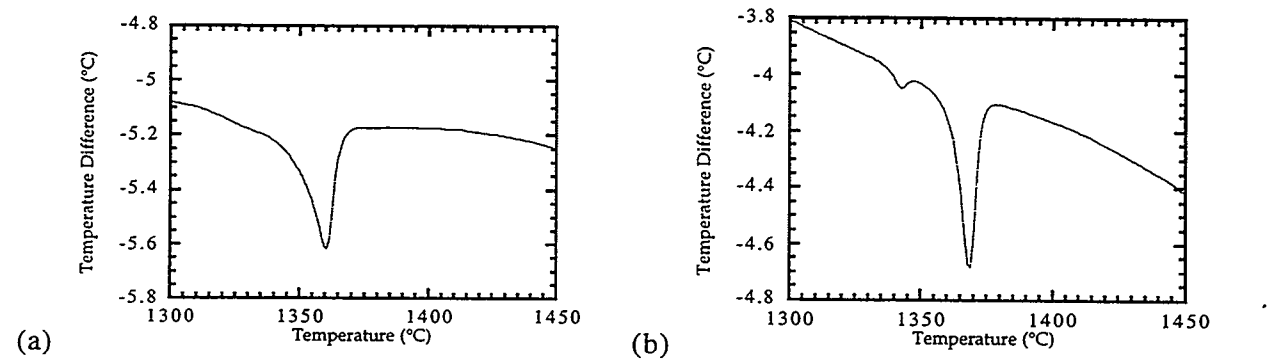

Fig. 1. DTA results on (a) prealloyed Ni_3Al-TiC (DC-11); and (b) Ni/NiAl-TiC (DC-14) mixtures.

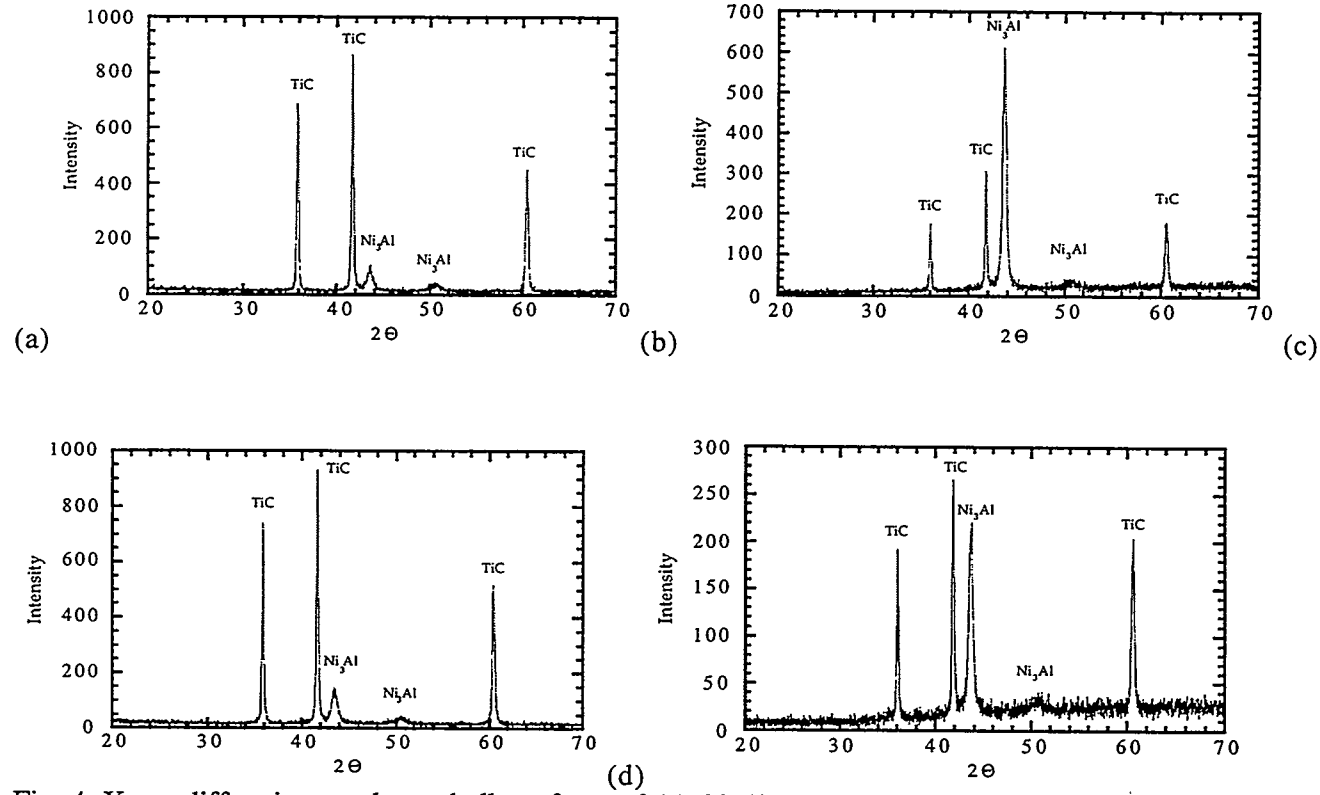

Fig. 4. X-ray diffraction results on bulk surfaces of (a) 30 % prealloyed Ni_3Al-TiC(DC-10); (b) 50% prealloyed Ni_3Al-TiC (DC-12); (c) 30 % reaction sintered Ni/NiAl-TiC (DC-13); and (d) 50 % reaction sintered Ni/NiAl-TiC (DC-15). All samples were sintered at 1400°C.

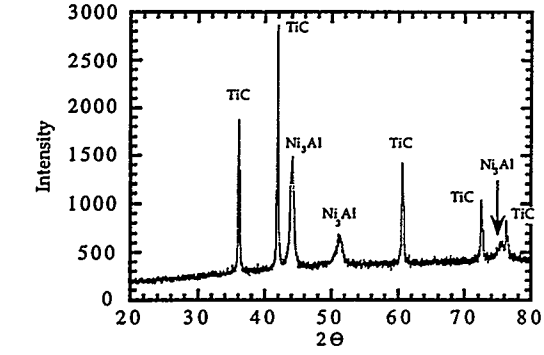

(a)

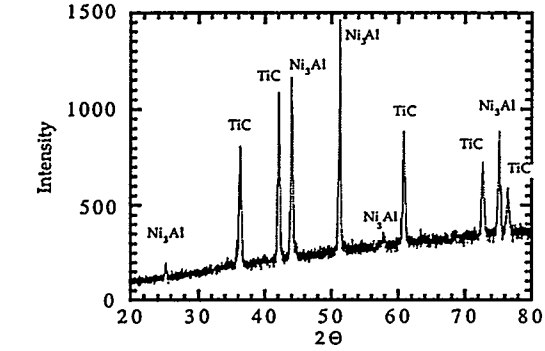

(b)

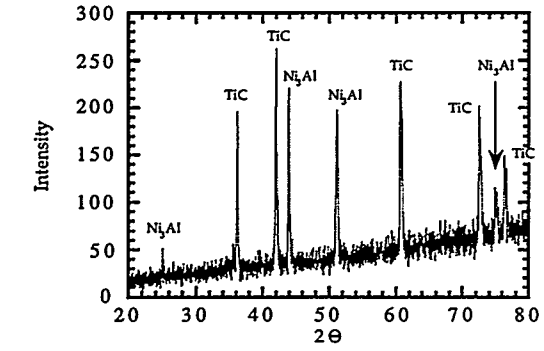

(c)

Fig. 2. X-ray powder diffraction results from prealloyed Ni_3Al-TiC mixtures (DC-11): (a) as-fabricated; (b) heated to 1200°C; and (c) heated to 1300°C.

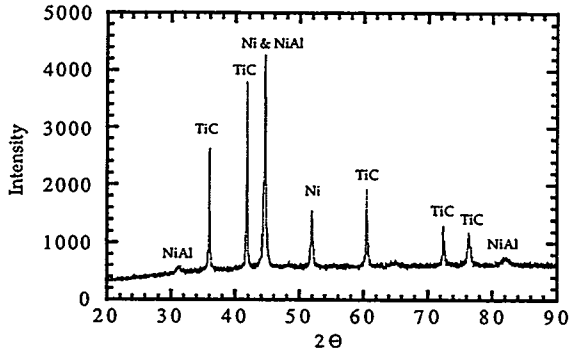

(a)

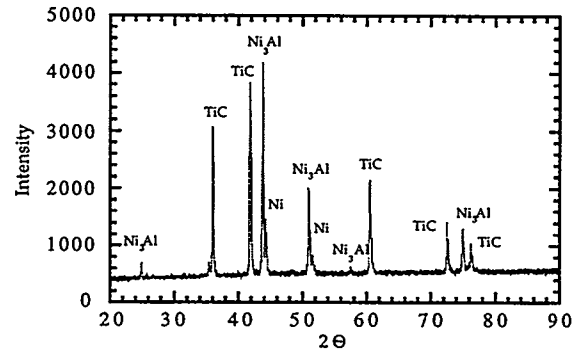

(b)

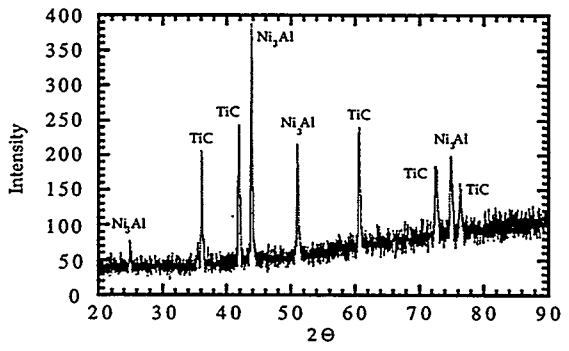

(c)

Fig. 3. X-ray powder diffraction results from reaction sintered NiAl/Ni-TiC mixtures (DC-14): (a) as-fabricated; (b) heated to 1200°C; and (c) heated to 1300°C.

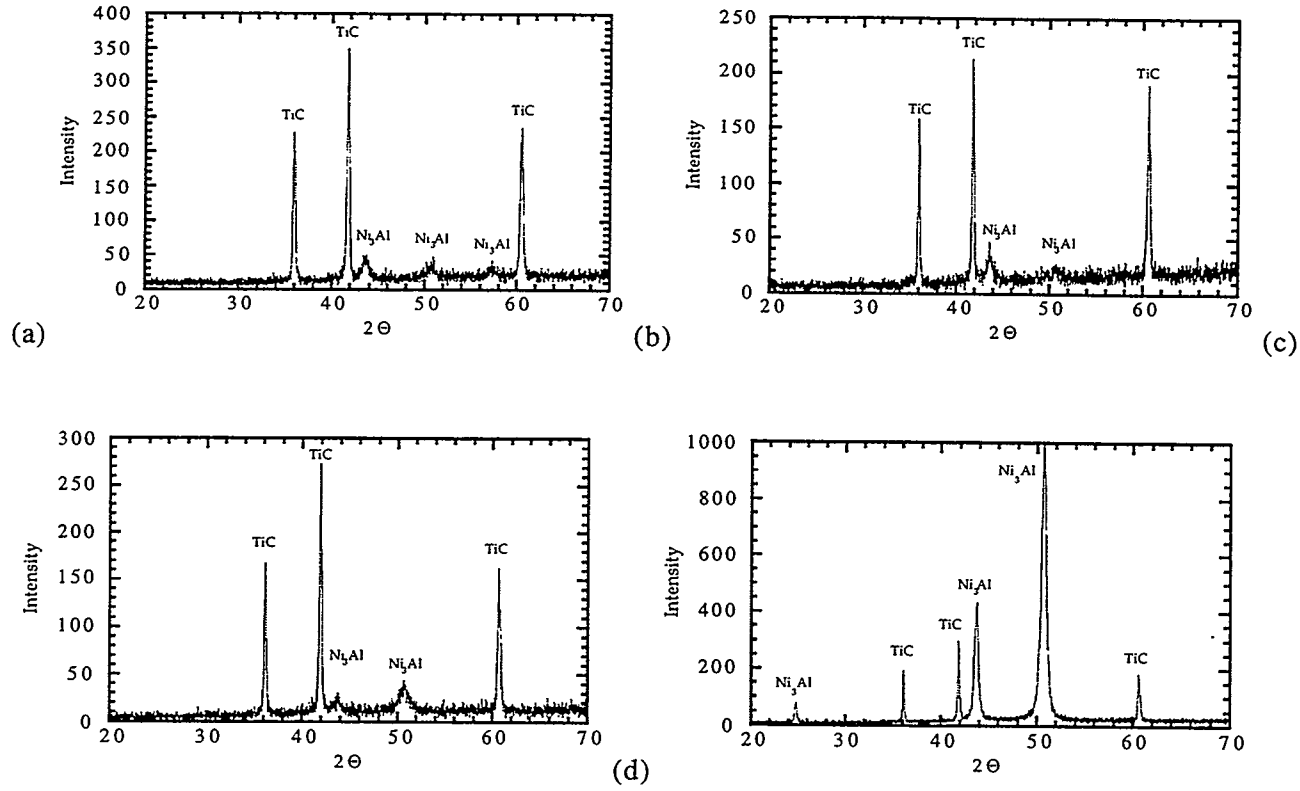

Fig. 5. X-ray diffraction results on bulk surfaces of (a) 30 % prealloyed Ni_3Al-TiC (DC-11); (b) 50% prealloyed Ni_3Al-TiC (DC-12); (c) 30 % reaction sintered Ni/NiAl-TiC (DC-13); and (d) 50 % reaction sintered Ni/NiAl-TiC (DC-15). All samples sintered at 1500°C.

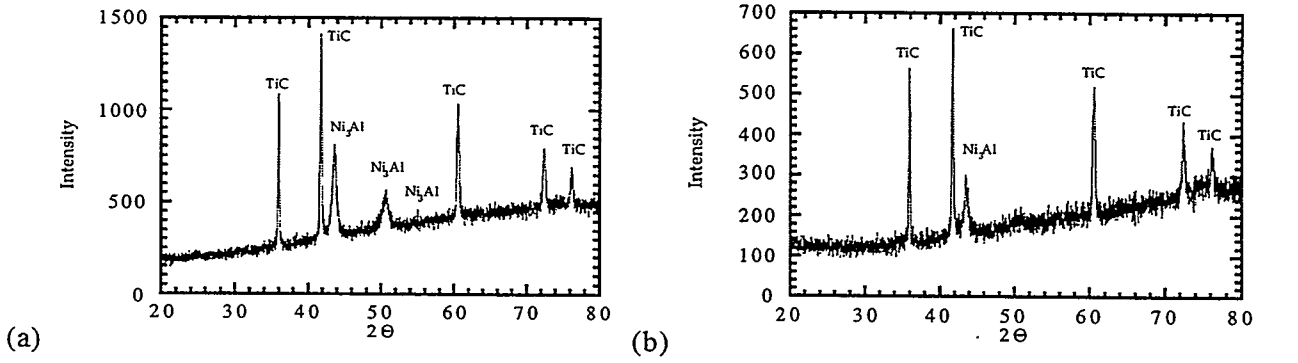

Fig. 6. X-ray diffraction results on bulk surfaces of (a) parallel, and (b) perpendicular to the sample thickness. Sample was 50 % reaction sintered Ni/NiAl-TiC (DC-15) sintered at 1400°C.

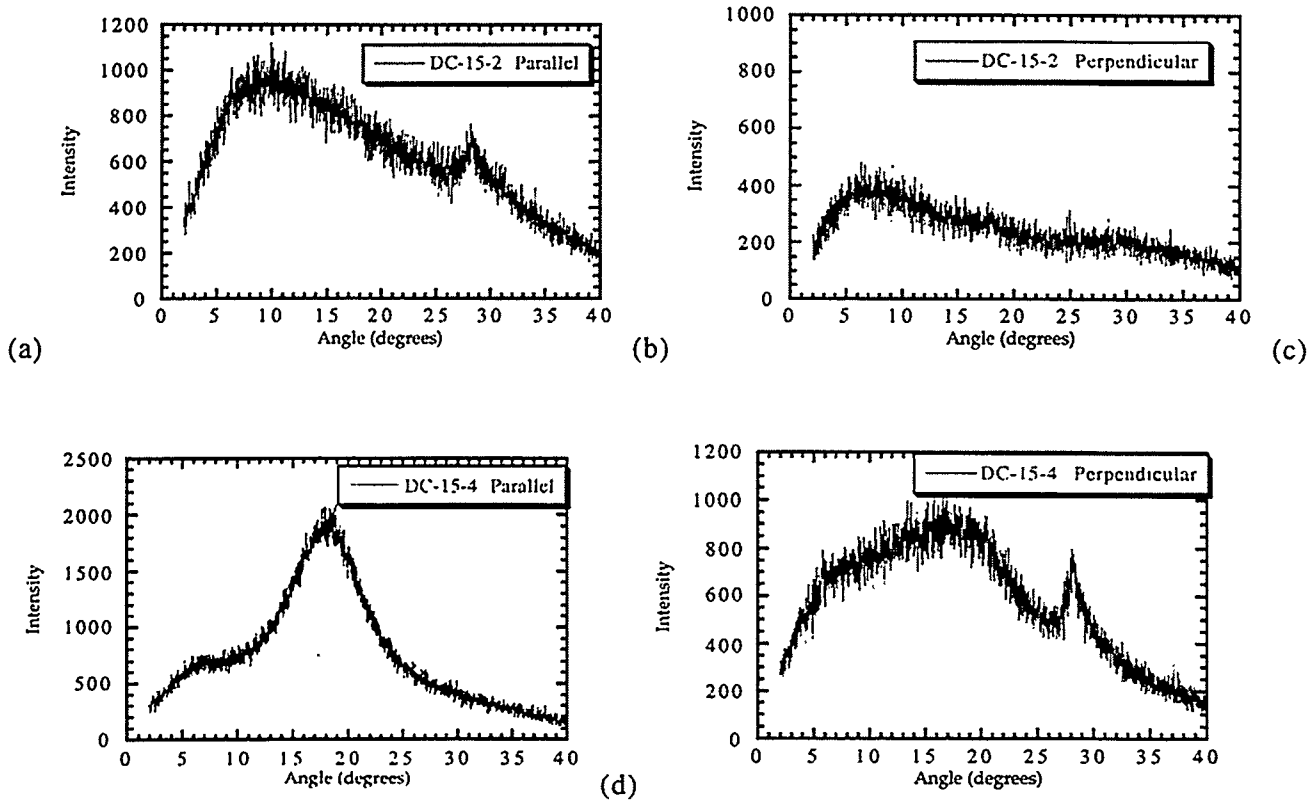

Fig. 7. X-ray rocking scans at $2\theta = 43.5°$ parallel to the sample thickness, (a) and (c); and perpendicular to the sample thickness, (b) and (d). Samples were 50 % reaction sintered Ni/NiAl-TiC (DC-15) sintered at 1400°C, (a) and (b); and at 1500°C, (c) and (d).

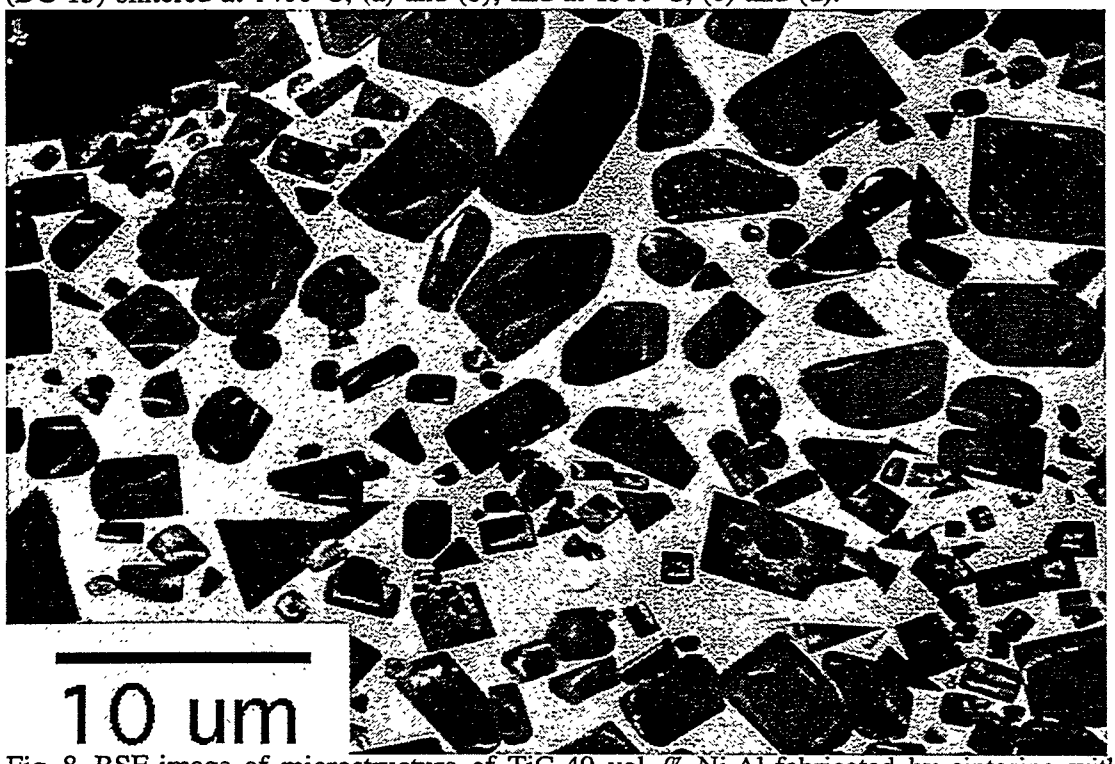

Fig. 8. BSE image of microstructure of TiC-40 vol. % Ni_3Al fabricated by sintering with prealloyed Ni_3Al (DC-11) at 1450°C. TiC particles exhibit a 'core-and-rim' morphology.

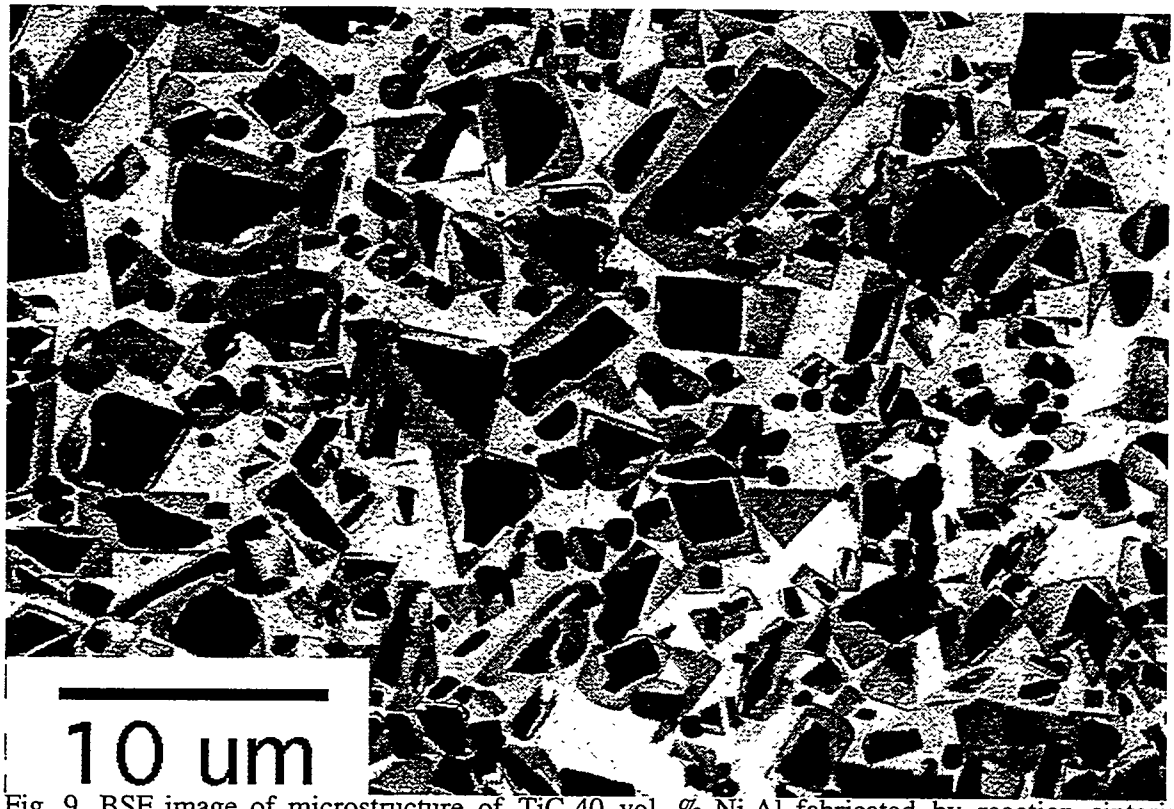

Fig. 9. BSE image of microstructure of TiC-40 vol. % Ni_3Al fabricated by reaction sintering with Ni/NiAl mixtures (DC-14) at 1450°C. TiC particles exhibit a 'core-and-rim' morphology.

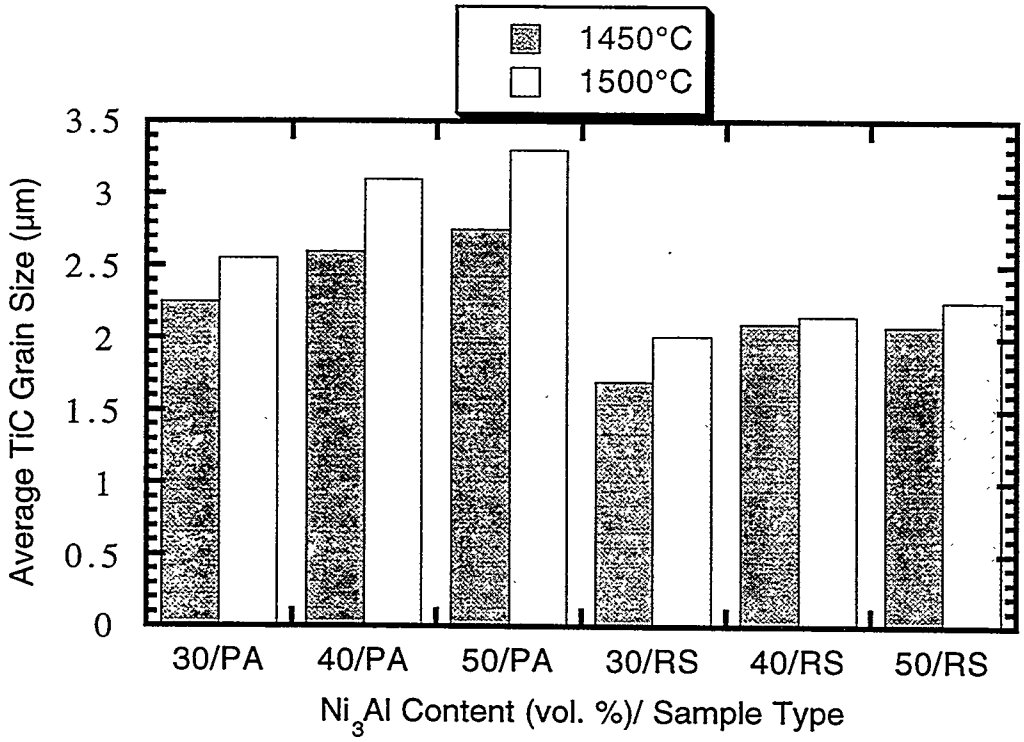

Fig. 10. Summary of average TiC grain size on Ni_3Al-bonded TiC composites fabricated using either prealloyed Ni_3Al powders (PA) or reaction sintered with elemental powders (RS). Sintering was done at the specified temperature.

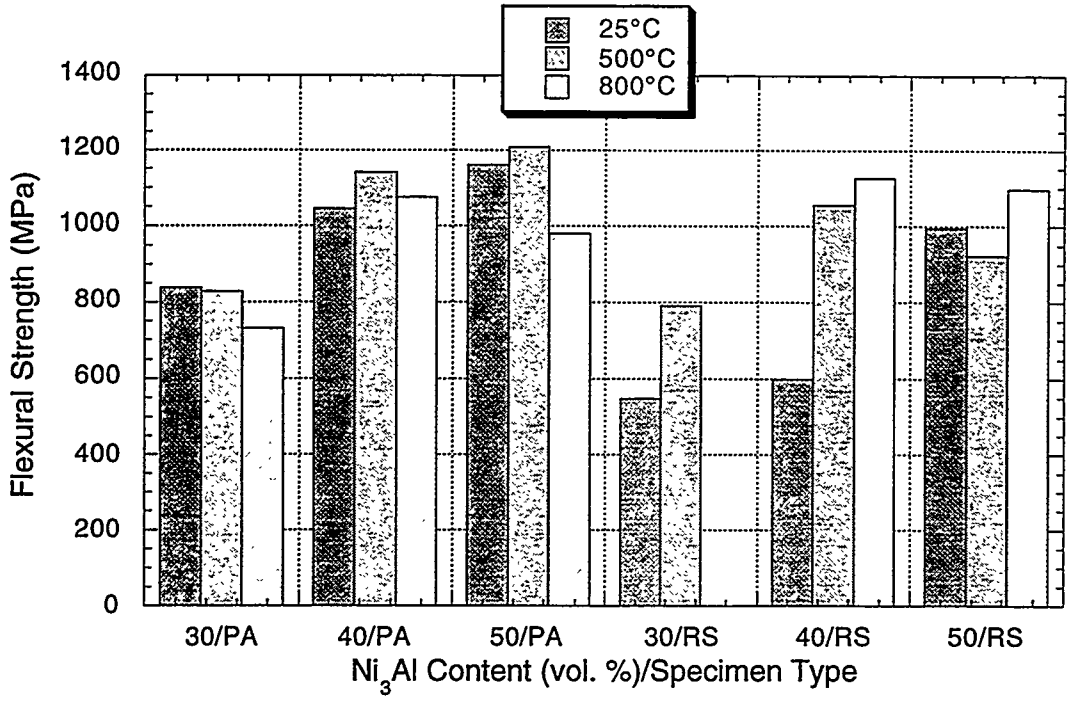

Fig. 11. Summary of results on the elevated temperature flexural strength of Ni_3Al-bonded TiC composites fabricated using either prealloyed Ni_3Al powders (PA) or reaction sintered with elemental powders (RS). The specimens were sintered at a temperature of 1450°C for 0.8 hour.

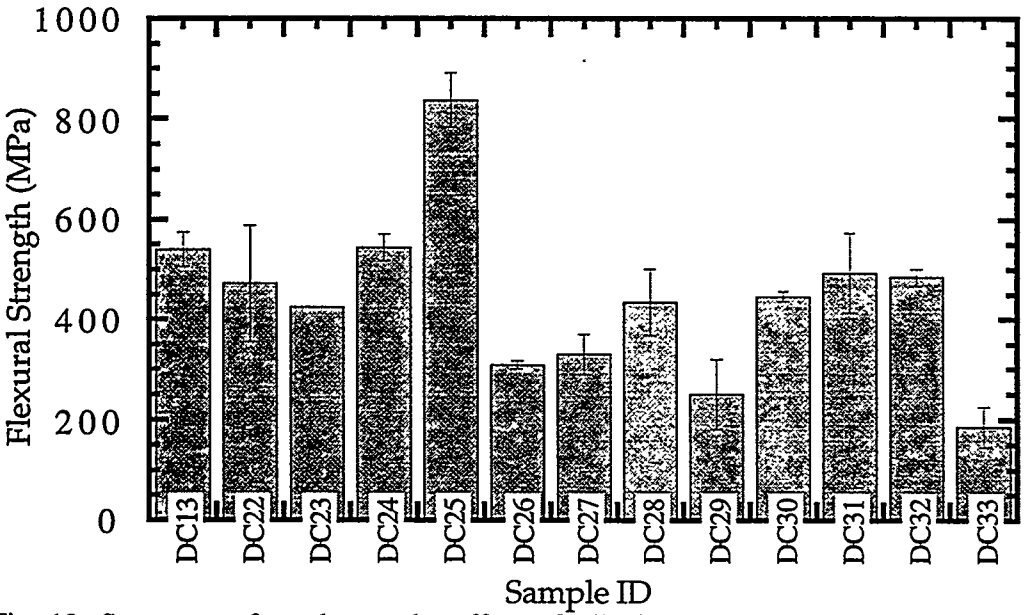

Fig. 12. Summary of results on the effect of alloying additives on the room temperature flexural strength of Ni_3Al-bonded TiC composites. The specimens were fabricated by reaction sintering with elemental powders (RS) at a temperature of 1450°C for 0.8 hour.

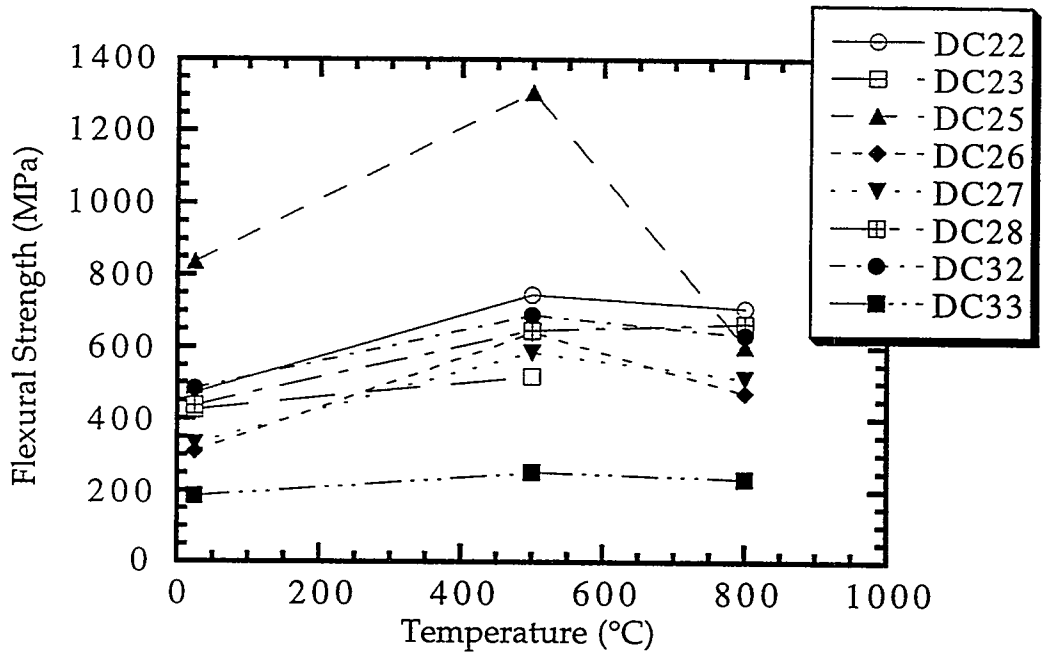

Fig. 13. Summary of results on the effect of alloying additives on the elevated temperature flexural strength of Ni_3Al-bonded TiC composites. The specimens were fabricated by reaction sintering with elemental powders (RS) at a temperature of 1450°C for 0.8 hour.

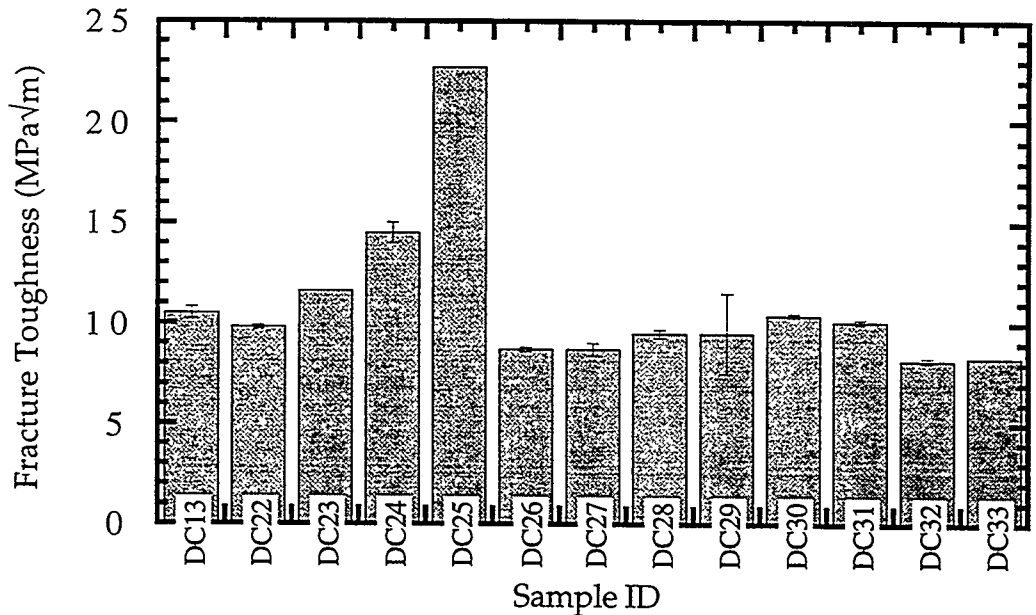

Fig. 14. Summary of results on the effect of alloying additives on the fracture toughness of Ni_3Al-bonded TiC composites. The specimens were fabricated by reaction sintering with elemental powders (RS). Sintering was done at a temperature of 1450°C for 0.8 hour.

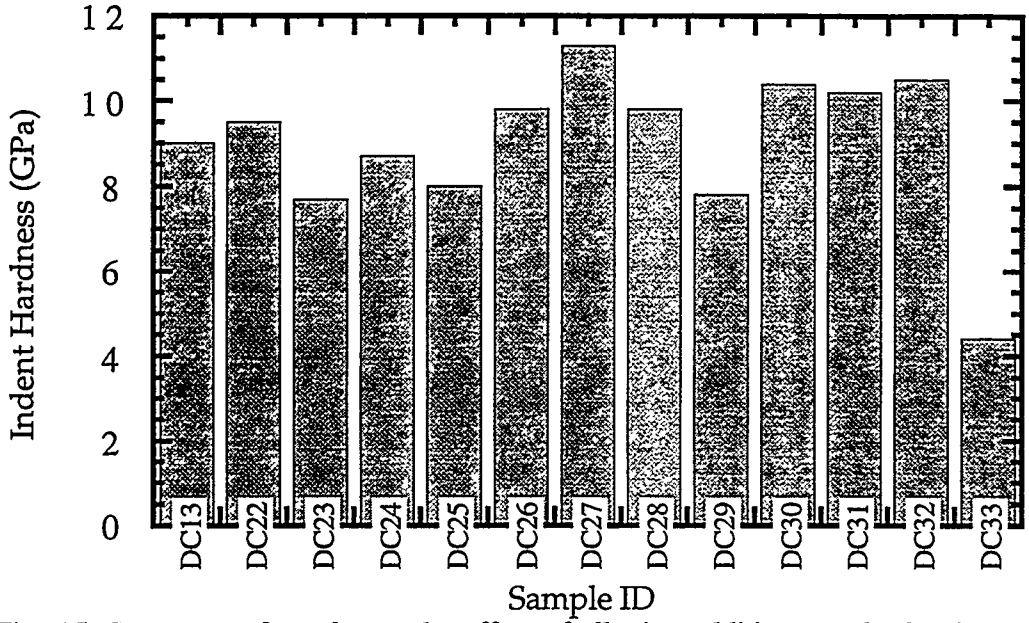

Fig. 15. Summary of results on the effect of alloying additives on the hardness of Ni_3Al-bonded TiC composites. The specimens were fabricated by reaction sintering with elemental powders (RS). Sintering was done at a temperature of 1450°C for 0.8 hour.

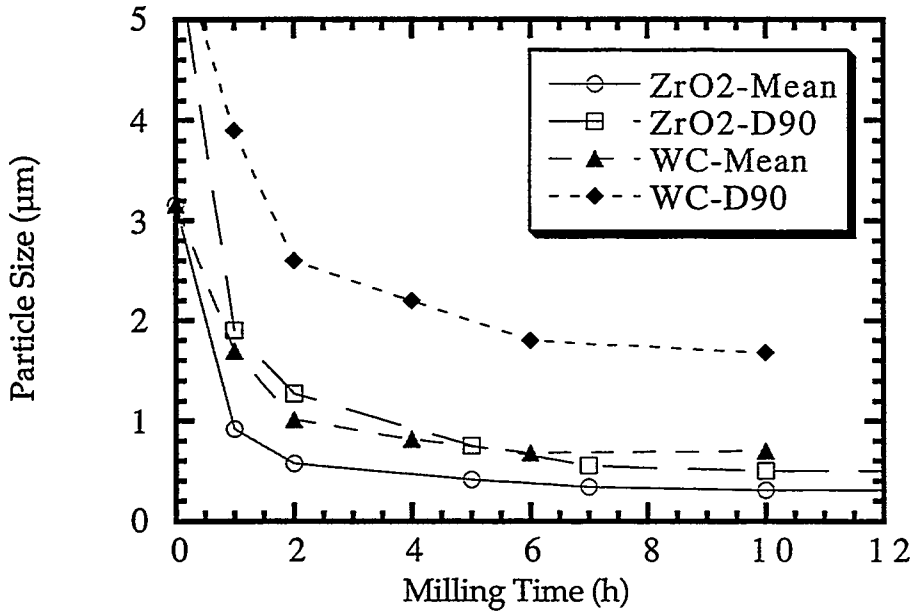

Fig. 16. Summary of results on the attritor milling of TiC powder with different media types and for various times.

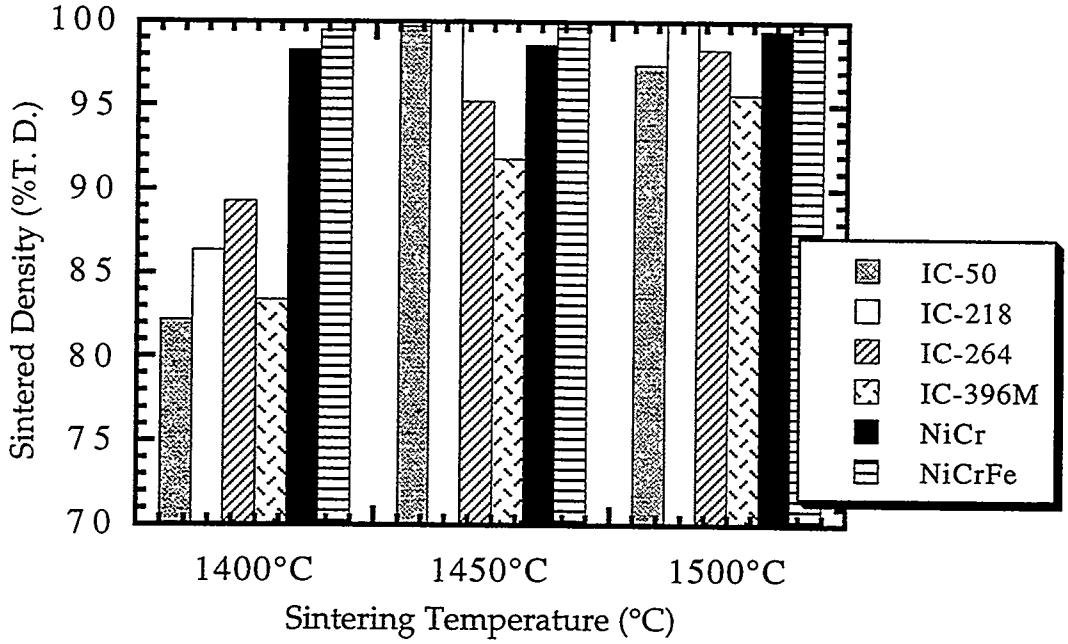

Fig. 17. Summary of densification behavior of TiC-40 vol. % Ni_3Al composites fabricated by sintering with different prealloyed binders. Sintering was done at the specified temperature for 0.8 hour.

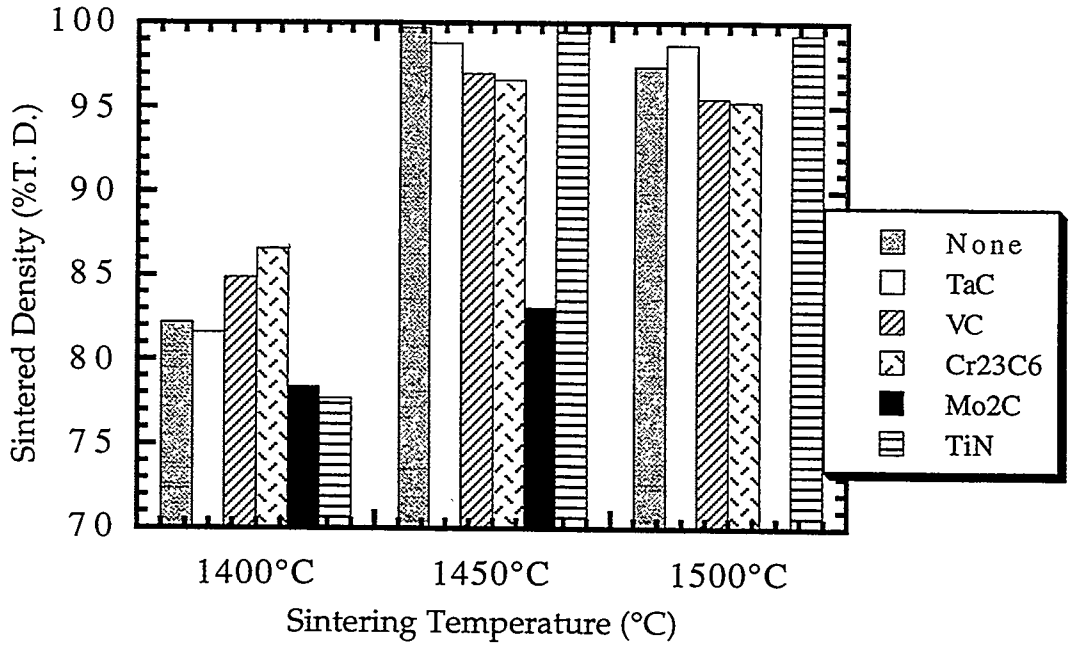

Fig. 18. Summary of densification behavior of TiC-40 vol. % Ni_3Al (IC-50 alloy) composites fabricated by sintering with different carbides substituted for 10 vol. % of the TiC. Sintering was done at the specified temperature for 0.8 hour.

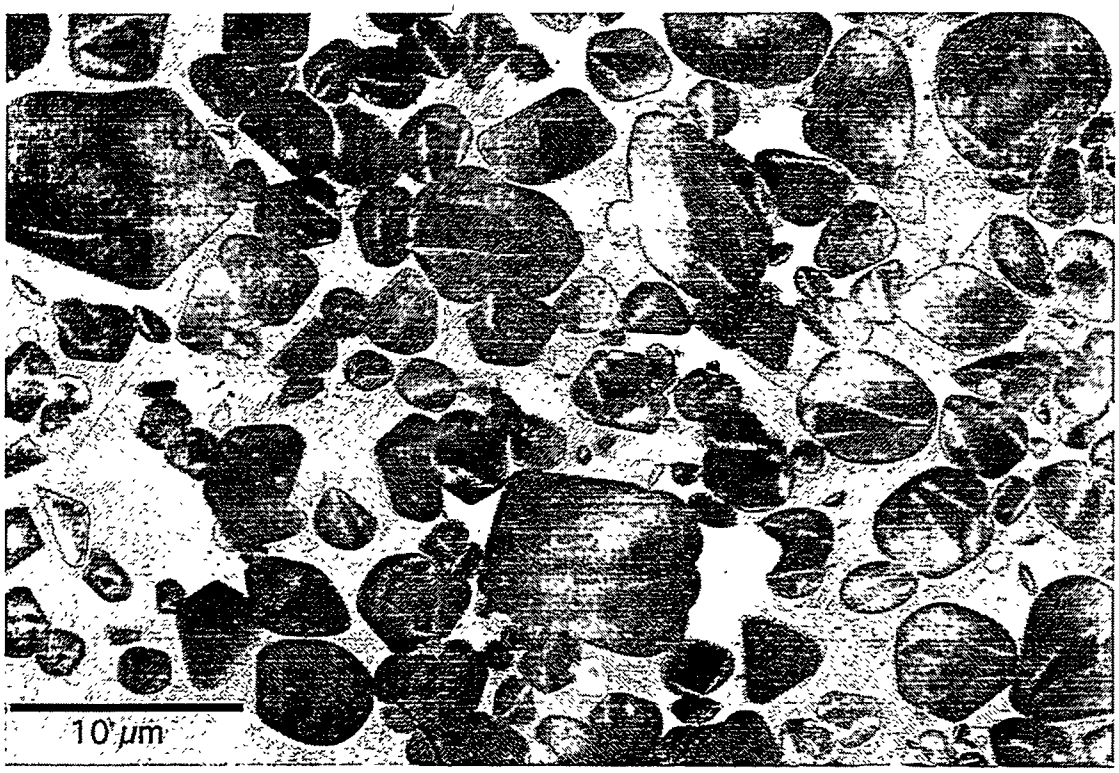

Fig. 19. BSE image of microstructure of TiC-40 vol. % Ni_3Al fabricated by sintering with prealloyed Ni_3Al (DC-46) at 1500°C for 0.8 h. TiC particles exhibit a 'core-and-rim' morphology.

Cost Effective Sintering of Silicon Nitride Ceramics (SIU-C)-
D. E. Wittmer, Southern Illinois University, Carbondale, IL 62901

Objective/Scope

The purpose of this work is to investigate the potential of cost effective sintering of Si_3N_4 and inter-metallic bonded carbides through the development of continuous sintering techniques.

Technical Highlights

Task 1. Refine Economic Model and Design for Chosen Furnace Configuration

This task was completed as reported in a previous semiannual report.

Task 2. Continue evaluation of sintering parameters on properties of selected Si_3N_4 compositions

Prototype Belt Furnace

Centorr Vacuum Industries, Inc. has redesigned the graphite hot zone to provide better insulation and thermal uniformity. The new hot zone was received and installed during this reporting period. The furnace was operated with the new graphite hot zone for over 150 hours with minimal affect on the insulation and marginal reactivity with the graphite heating elements. There was a fracture in one of the welds in the furnace chamber during one of the high heating/cooling rate experiments which was repaired in less than 24 hours and the furnace made operational again. There was minor damage to the furnace insulation in the third zone due to water contacting the insulation at a temperature of about 1500°C. The entire hot zone has been removed for inspection and will be reinstalled during the next reporting period.

1. Collaboration with Industrial Partners and Affiliates

Work continues according to plan to develop collaborations with industrial partners. Due to the proprietary/confidential relationships established, the results of these collaborations will be reported as part of their individual programs.

2. Silicon Nitride Valves for SAE Car

The Honda 600 cc engine, which is the prototype for the engine to be used in the SAE car competition, presently has over 8,000 road test miles on the silicon nitride valves and is routinely driven on an official race track. The performance data suggests that both mileage and horsepower have been improved by the addition of these valves, however further improvements can only be obtained through the addition of another camshaft.

4. Evaluation of Continuous Sintering of Silicon Nitride-Titanium Carbide

During this reporting period, the thermal shock resistance was determined for the baseline A3Y9 and selected composites containing TiC or TiN. The results are given in Table I. The test bars were standard type-B that were machined from billets that were continuous sintered at 1775°C for 2 h. These results show that the strength was significantly reduced by thermal shocking above 1000°C for the baseline A3Y9 and severely affected even at 1000°C for the composites containing TiC. The composites containing TiN were relatively unaffected for the thermal shock temperatures investigated. These results imply that even with only minor additions of TiN the thermal shock resistance can be improved. Previous results showed that this minor addition of TiN also improved the fracture toughness with only marginal decrease in flexural strength and also improved the densification.

More recently, a larger batch of the baseline A3Y9 containing 10 wt% TiN (pre-turbomilled for 24 hours) was prepared into discs. The discs formed are currently being dried and will be isopressed and sintered, during the next reporting period. Toughness and microstructures are presently being determined for a statistically significant number of test bars for both the TiN and TiC containing composites.

Task 3. Continue Evaluation of Low Cost Si_3N_4 Powders

Nothing to report this reporting period.

Task 4. Design and Construct Prototype Belt Furnace

This task has been completed.

Task 5. Continuous Sintering of Inter-metallic Bonded Carbides

During part of this reporting period, Frederik Goransson (MS student) was at ORNL preparing additional materials for comparison of batch to continuous sintering. Several different inter-metallic bonded TiC formulations were prepared. A partial list is

given in Table II. Figure 1 shows some of the density results for these formulations, following batch sintering at 1450°C and 1500°C. As seen from these results some of the formulations achieved greater than the estimated theoretical density at both sintering temperatures.

During this reporting period the results were completed on the comparison of continuous sintering (SIUC) and batch pressure sintering (ORNL). These results are given in Table III through XVI and shown graphically in Figures 2 through 7.

The results in Table III and Fig. 2 show that very high densities were obtained by both batch pressure and continuous sintering at 1450°C for many of the alloying elements. At this sintering temperature, continuous sintering produced higher densities for Si, Ti and Mo alloying elements, while batch pressure sintering produced higher densities for W, Co, and Zr. The poorest densification for either sintering method resulted when the alloying modifier was Zr.

By increasing the sintering temperature to 1500°C (Table IV and Fig.3), many of

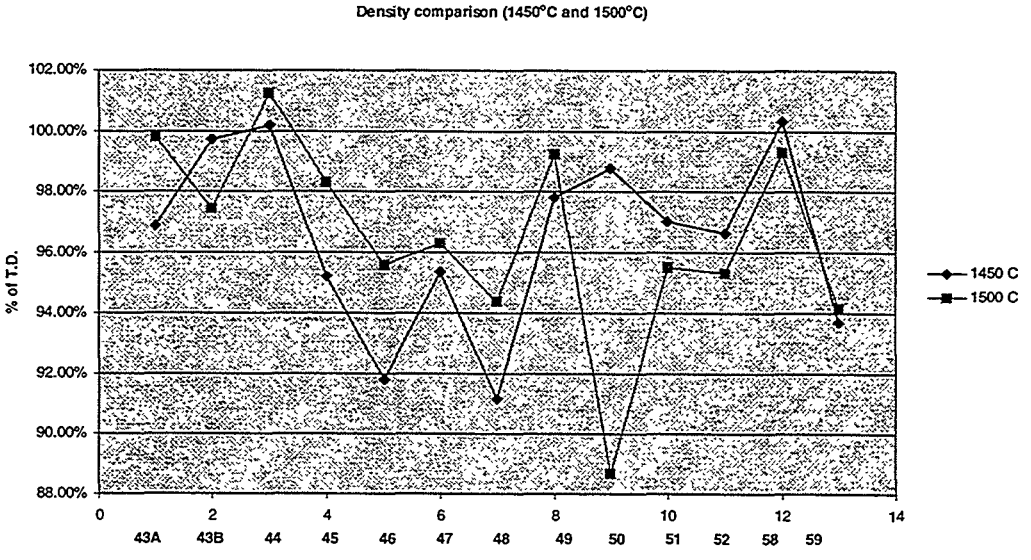

Figure 1. Sintering Results for Batch Pressure Sintering at ORNL

the densities were improved. At this sintering temperature, continuous sintering produced high densities for Fe, Si, and Ti alloying elements, while batch pressure sintering produced significantly higher densities for Mo and Co alloying elements. For batch sintering at this temperature, densities for Fe and W were significantly reduced.

Because the densities were low for both the Cr and Zr alloying modified alloys, the cermets containing these alloying modifiers were not tested for hardness and fracture toughness. A comparison of the results obtained for batch pressure and continuous sintering at 1450°C (Table V, Fig. 4 and Fig. 6) show that in general batch sintering produced higher hardness and marginally higher toughness for most of the alloying

modifiers. The exceptions were for Ti and Mo, where continuous sintering produced marginally higher toughness and similar hardness. The highest hardness was obtained for the W and Co alloying modifiers, while the highest toughness was obtained for Fe as the alloying modifier.

For sintering at 1500°C (Table VI, Fig. 5 and Fig. 7), the hardness increased slightly for Fe and Si alloying modifiers for continuous sintering, while for batch pressure sintering the hardness for all alloying modifiers it slightly decreased. For Si and Ti similar hardness and toughness were obtained for both sintering methods, while significantly higher toughness resulted for the Co alloying modifier with continuous sintering.

The microstructural results show that for all cases considerable solubility of the TiC existed during reaction sintering in both the batch pressure furnace and the continuous furnace.

From previous work, it was shown that pre-alloying produces cermets with larger TiC grain sizes. This may be due to (1) enhanced reactivity due to the presence of more surface oxygen on the powders during reaction sintering; (2) enhanced diffusion of Ti in the liquid phase; or (3) a kinetic effect due to solution and reprecipitation of the TiC in the liquid phase. The results show that the corners of the TiC have been rounded when using the using pre-alloyed Ni_3Al. This suggests that the points with highest radius of curvature were dissolved preferentially. In comparison, the cermets with Ni_3Al produced by reaction sintering show that the TiC surfaces appear to have been more uniformly reduced during sintering.

When Fe was used as an alloying element, it would appear that continuous sintering produced more reprecipitated TiC than batch pressure sintering. However, the overall solubility of the TiC in the binder phase appears to be increased by the addition of Fe. Similarly the addition of Mo and W as alloy modifiers appear to have had a major effect on the solubility of the TiC in the binder phase. Also, in general continuous sintering appears to have produced a finer TiC structure and a greater amount of reprecipitated TiC than batch pressure sintering.

The materials that were prepared at ORNL by graduate student Frederik Goranson were also continuously sintered in the belt furnace at SIUC using Ar. The purpose of this study was to continue to investigate and compare the properties of continuos sintered intermetallics to those produced by batch pressure sintering. In addition some preliminary investigations were conducted into the effects of higher heating and cooling rates on the properties and microstructure. These results are shown in Tables VII through XVI.

Tables VII through XV show that for sintering times of only 25 min, high densities were obtainable for both the baseline and some selected alloy formulations. Higher densities were generally obtained by batch pressure sintering, however continuous sintering parameters were not optimized for these sintering trials.

Tables VIII through XI show that for most of the formulations, high density was only achieved by batch pressure sintering. Again the continuous sintering parameters were not optimized for this part of the study because these were screening experiments and the number of samples was limited.

Table XII shows the results for the baseline prealloyed 30 vol% Ni3Al for three sintering temperatures and two sintering rates. These runs did not produce the expected results and will be repeated. It is suspected that the binder was not removed entirely prior to sintering, which caused out-gassing and bloating during sintering.

Table XIII and XIV show the results for two other commercial prealloyed Ni3Al alloys for two different sintering temperature and two sintering times. The higher sintering temperature produced higher density, but lower than expected. The higher heating rate and higher temperature, however produced the highest density. Therefore additional experiments are planned to further investigate the IC-50 alloy system.

Table XV gives the continuous sintering results for the reaction sintered alloy systems with 70 vol% TiC for three sintering temperatures and two sintering rates at each temperature. The specimens used for these trials were 1 in. diameter discs. Table XVI gives the results for the same alloy systems for larger billets for only one sintering temperature at the highest sintering rate. These results show that for some systems, the higher sintering rates produce higher density and these effects are dependent on the sintering temperature. Additional trials are planned for higher temperatures and heating rates for the alloy systems with the highest densities under the previous conditions.

Status of Milestones

1.	Refine Economic Model and Design for Chosen Furnace Configuration	Completed
2.	Continue Evaluation of Sintering Parameters on Properties of Selected Si_3N_4 Compositions	On Schedule
3.	Continue Evaluation of Low Cost Si_3N_4 Powders	On Schedule
4.	Design and construct prototype belt furnace	Completed
5.	Continuous sintering of inter-metallic bonded carbides	On Schedule

Problems Encountered

None

Publications and Presentations

D. E. Wittmer, F. Goranson, T. Tiegs, and J. Schroeder, "Aluminide-Bonded TiC Sintered by Two Methods," American Ceramic Society 101st Annual Meeting, April 29, 1999 in Indianapolis, IN.

J. Smith, D. E. Wittmer, M. Lee, and A. Migone, "Effect of TiC and TiN Additions on the Properties of Silicon Nitride Composites," American Ceramic Society 101st Annual Meeting, April 29, 1999 in Indianapolis, IN.

D. Wittmer, F. Goranson, T. Tiegs and J. Schroeder, "Comparison of Batch and Continuous Sintering of Aluminide-Bonded TiC," PMTECH '99, Vancouver, BC, June 20-24, 1999.

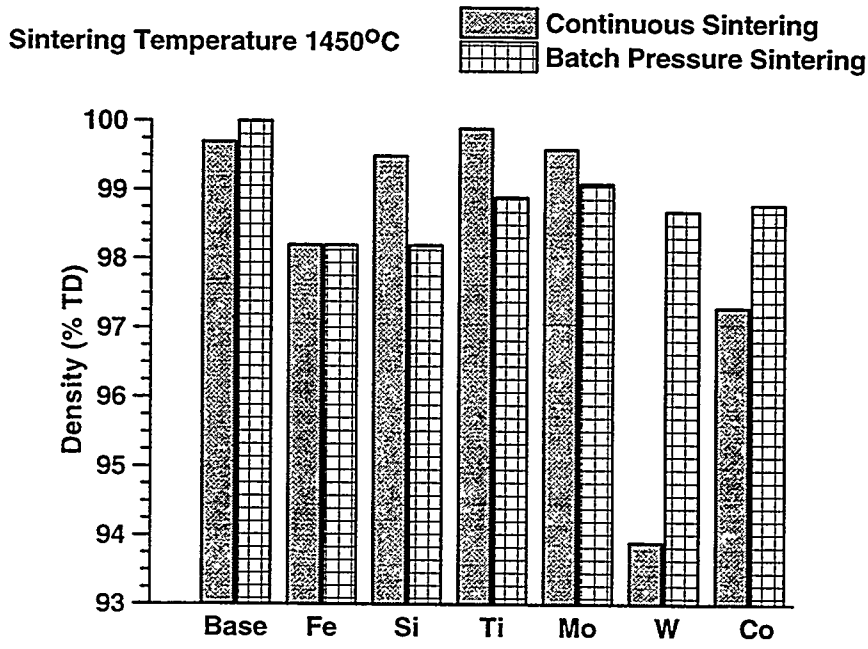

Figure 2. Density comparison for Ni_3Al-TiC with alloying additions batch pressure and continuous sintered in Ar at 1450°C.

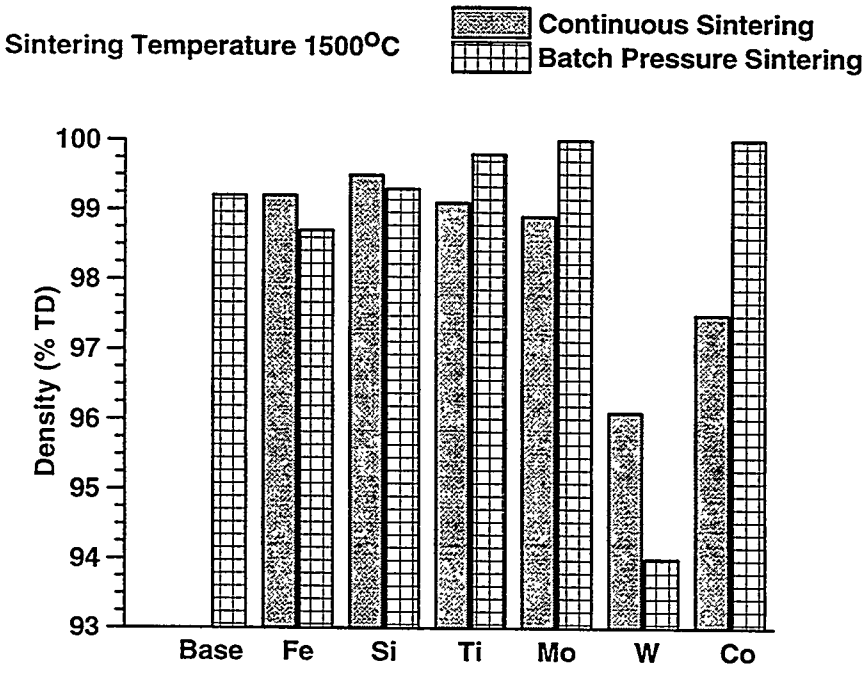

Figure 3. Density comparison for Ni_3Al-TiC with alloying additions batch pressure and continuous sintered in Ar at 1500°C.

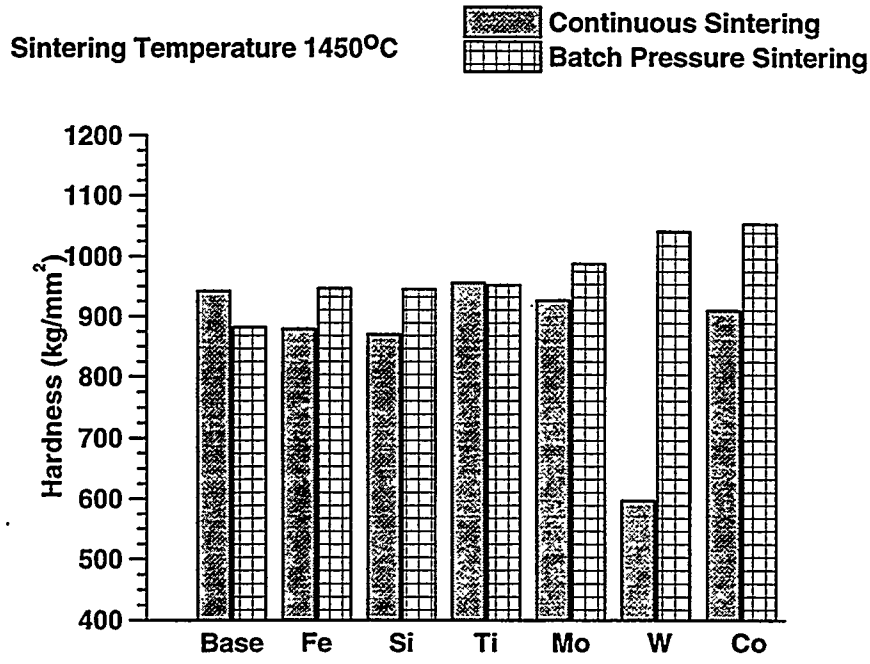

Figure 4. Hardness comparison for Ni_3Al-TiC with alloying additions batch pressure and continuous sintered in Ar at 1450°C.

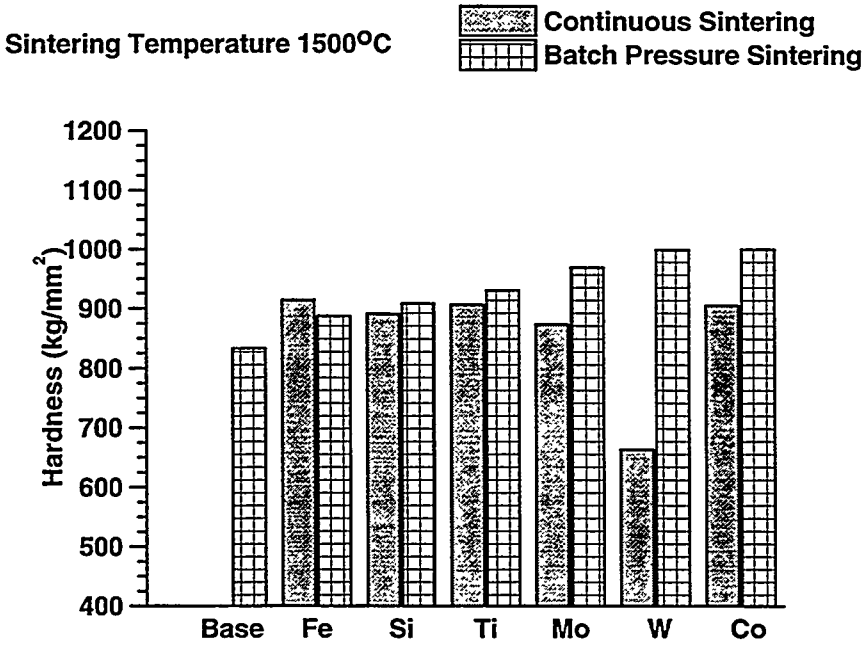

Figure 5. Hardness comparison for Ni_3Al-TiC with alloying additions batch pressure and continuous sintered in Ar at 1500°C.

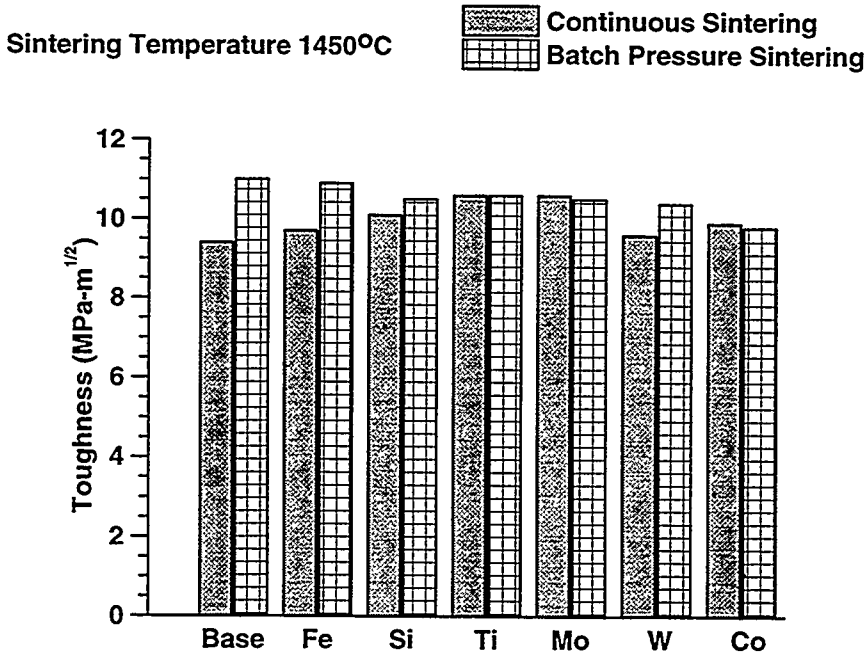

Figure 6. Fracture toughness comparison for Ni_3Al-TiC with alloying additions batch pressure and continuous sintered in Ar at 1450°C.

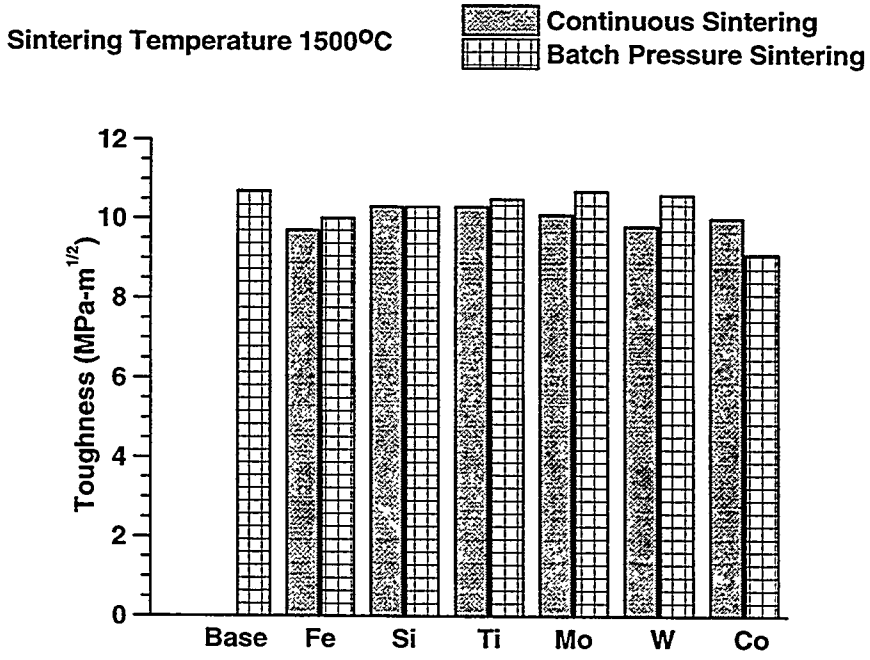

Figure 7. Fracture toughness comparison for Ni_3Al-TiC with alloying additions batch pressure and continuous sintered in Ar at 1500°C.

Table I. Thermal Shock Results for A3Y9 with 5 wt%TiC or 5 wt% TiN

Designation	Thermal Shock Temperature	Four-Point Flexural Strength (MPa)
Baseline A3Y9 Formulation	25 1000 1100 1200	1003 933 699 190
TC5 95/5 Premilled Starck TiC* (d = 0.77 μm) Pressure Cast and CIP'ed	25 1000 1100 1200	523 166 40 244
TC4 95/5 TiC from Dr. Koc Pressure Cast and CIP'ed	25 1000 1100 1200	713 551 187 257
TN3 95/5 Premilled Starck TiN* (d = 0.53 μm) Pressure Cast and CIP'ed	25 1000 1100 1200	923 963 894 851

* Commercial TiN provided by H.C. Starck

Table II. Formulations and processing for some additional TiC-cermets processed (Density results shown in Figure 1.)

DC-43 A	TiC, IC-50 (-200 mesh)	ball milled 89h
B	TiC, IC-50 (-200 mesh)	ball milled 24h
DC-44	TiC, IC-218 (-325 mesh)	ball milled 24h
DC-45	TiC, IC-264 (-325 mesh)	ball milled 24h
DC-46	TiC, IC-396M (-325 mesh)	ball milled 24h
DC-47	TiC, IC-50 (-200 mesh)	attritor milled 4h
DC-48	TiC, IC-50 (-200 mesh)	attritor milled 9h
DC-49	TiC, NiAl (X-form), Ni (Novamet 123), B (Alfa)	attritor milled 4h
DC-50	TiC, TaC (Alfa), IC-50 (-200 mesh)	ball milled 24h
DC-51	TiC, VC (Alfa), IC-50 (-200 mesh)	ball milled 24h
DC-52	TiC, $Cr_{23}C_6$ (Alfa), IC-50 (-200 mesh)	ball milled 24h
DC-53	TiC, NiCr (Alfa)	ball milled 24h
DC-54	TiC, NiCrFe (Alfa)	ball milled 24h
DC-55	TiC, Ti-48Al-2Cr-2Nb (-325 mesh)	ball milled 24h
DC-56	TiB_2, TiAl (same as in DC-55)	ball milled 24h
DC-57	TiC, Mo_2C (Alfa –325 mesh), IC-50 (-200 mesh)	ball milled 24h
DC-58	TiC, TiN (ICD), IC-50 (-200 mesh)	ball milled 24h
DC-59	TiC, IC-50 (-200 mesh, heat treated)	ball milled 24h

Table III. Sintering Results for Intermetallic-Bonded TiC at 1450°C for 50 min.

Intermetallic Phase	Continuous Furnace (SIUC)	Pressure Furnace (ORNL)
	% Target Density	
$Ni_{2.85}Fe_{0.20}Al_{0.95}$	98.2	98.2
$Ni_{2.85}Cr_{0.20}Al_{0.95}$	93.6	92.7
$Ni_{3.00}Si_{0.20}Al_{0.80}$	99.5	98.2
$Ni_{3.00}Ti_{0.20}Al_{0.80}$	99.9	98.9
$Ni_{3.00}Mo_{0.20}Al_{0.80}$	99.6	99.1
$Ni_{3.00}W_{0.20}Al_{0.80}$	93.9	98.7
$Ni_{2.40}Co_{0.60}Al_{1.00}$	97.3	98.8
$Ni_{3.00}Zr_{0.20}Al_{0.80}$	84.3	91.0

Table IV. Sintering Results for Intermetallic-Bonded TiC at 1500°C for 50 min.

Intermetallic Phase	Continuous Furnace (SIUC)	Pressure Furnace (ORNL)
	% Target Density	
$Ni_{2.85}Fe_{0.20}Al_{0.95}$	99.2	98.7
$Ni_{2.85}Cr_{0.20}Al_{0.95}$	95.1	97.2
$Ni_{3.00}Si_{0.20}Al_{0.80}$	99.5	99.3
$Ni_{3.00}Ti_{0.20}Al_{0.80}$	99.1	99.8
$Ni_{3.00}Mo_{0.20}Al_{0.80}$	98.9	100.3
$Ni_{3.00}W_{0.20}Al_{0.80}$	96.1	94.0
$Ni_{2.40}Co_{0.60}Al_{1.00}$	97.5	106.1
$Ni_{3.00}Zr_{0.20}Al_{0.80}$	86.7	95.8

Table V. Comparison of Vickers Hardness for Intermetallic-Bonded TiC Sintered in Ar at 1450°C for 50 min in a Continuous Furnace (SIUC) and a Pressure Furnace (ORNL)

Intermetallic Phase	50 kg Load			
	Continuous Furnace SIUC		Pressure Furnace ORNL	
	Hardness (kg/mm^2)	K_{IC} ($MPa \cdot m^{1/2}$)	Hardness (kg/mm^2)	K_{IC} ($MPa \cdot m^{1/2}$)
$Ni_{2.85}Fe_{0.20}Al_{0.95}$	879	9.73	946	10.93
$Ni_{3.00}Si_{0.20}Al_{0.80}$	870	10.05	945	10.50
$Ni_{3.00}Ti_{0.20}Al_{0.80}$	956	10.63	952	10.60
$Ni_{3.00}Mo_{0.20}Al_{0.80}$	927	10.59	988	10.51
$Ni_{3.00}W_{0.20}Al_{0.80}$	597	9.61	1042	10.44
$Ni_{2.40}Co_{0.60}Al_{1.00}$	910	9.86	1054	9.76

Table VI. Comparison of Vickers Hardness for Intermetallic-Bonded TiC Sintered in Ar at 1500°C for 50 min in a Continuous Furnace (SIUC) and a Pressure Furnace (ORNL)

Intermetallic Phase	50 kg Load			
	Continuous Furnace SIUC		Pressure Furnace ORNL	
	Hardness (kg/mm^2)	K_{IC} ($MPa \cdot m^{1/2}$)	Hardness (kg/mm^2)	K_{IC} ($MPa \cdot m^{1/2}$)
$Ni_{2.85}Fe_{0.20}Al_{0.95}$	914	9.66	887	10.04
$Ni_{3.00}Si_{0.20}Al_{0.80}$	891	10.34	908	10.27
$Ni_{3.00}Ti_{0.20}Al_{0.80}$	906	10.29	930	10.54
$Ni_{3.00}Mo_{0.20}Al_{0.80}$	873	10.09	969	10.67
$Ni_{3.00}W_{0.20}Al_{0.80}$	663	9.79	999	10.63
$Ni_{2.40}Co_{0.60}Al_{1.00}$	905	9.95	1000	9.08

Table VII. Results for Continuously Sintered TiC Bonded with 30vol% Reaction Sintered Ni3Al (baseline composition).

Sintering Temperature (°C)	Sintering Time 50 min (belt speed 0.75"/min)	Sintering Time 25 min (belt speed 1.5"/min)
	% Target Density	
1450	89.9	84.8
1500	97.8	92.2
1550	99.1	98.9
1600	-------	99.7

Table VIII. TiC Bonded with 40vol% Prealloyed Ni3Al Milled with ZrO_2 Media Sintered at 1450°C.

Alloy compound	Continuous Furnace, 25 min (SIUC)	Continuous Furnace, 50 min (SIUC)	Batch Pressure Furnace, 50 min (ORNL)
	% Target Density		
IC 50*	90.4	94.5	99.7
IC 218**	92.6	99.5	100.2
IC 264***	90.9	96.6	95.2
Ni_3Al ****	85.9	94.8	97.8
NiCr	97.2	98.0	93.6
NiCrFe	100.0	99.9	101.8

* IC 50 - Ni-Al-Zr-B (baseline)
** IC 218 - Ni-Al-Zr-Cr-B
*** IC 264 - Ni-Al-Zr-Cr-W-B
**** Reaction Sintered, attrition milled for 4h

Table IX. TiC Bonded with 40vol% Prealloyed Ni3Al Milled with ZrO_2 Media, Sintered at 1500°C.

Alloy compound	Continuous Furnace, 25 min (SIUC)	Continuous Furnace, 50 min (SIUC)	Batch Pressure Furnace, 50 min (ORNL)
	% Target Density		
IC 50*	93.1	93.6	97.4
IC 218**	98.6	97.8	101.2
IC 264***	96.7	95.8	98.3
Ni_3Al ****	93.1	93.7	99.2
NiCr	98.1	98.4	99.5
NiCrFe	100.7	99.4	100.3

* IC 50 - Ni-Al-Zr-B (baseline)
** IC 218 - Ni-Al-Zr-Cr-B
*** IC 264 - Ni-Al-Zr-Cr-W-B
**** Reaction Sintered, attrition milled for 4h

Table X. TiC Bonded with 40vol% Prealloyed Ni3Al Milled with ZrO_2 Media, Sintered at 1450°C.

Alloy compound	Continuous Furnace, 25 min (SIUC)	Continuous Furnace, 50 min (SIUC)	Batch Pressure Furnace, 50 min (ORNL)
	% Target Density		
IC 50[1] †	65.6	85.5	96.9
IC 396M ††	83.5	85.2	91.8
IC 50[2]	78.4	86.4	95.7
IC 50[3]	84.5	81.2	91.1
TaC - IC 50	84.6	86.9	98.8
VC - IC 50	83.3	85.9	97.0
$Cr_{23}C_6$ - IC 50	76.8	75.6	96.6
Ti-48Al-2Cr-2Nb	70.1	71.6	72.8
TiB_2 - Ti-48Al-2Cr-2Nb	64.5	65.9	61.6
Mo_2C - IC 50	85.8	90.2	83.1
TiN - IC 50	77.9	85.2	100.3
IC 50 †††	82.6	85.6	93.7

† IC 50 - Ni-Al-Zr-B (baseline)
†† IC 396M - Ni-Al
††† Heat Treated
1 Ball milled for 89h
2 Attrition milled for 4h
3 Attrition milled for 9h

Table XI. Sintering Results of TiC Bonded with 40vol% Prealloyed Ni3Al Milled with ZrO_2 Media, Sintered at 1500°C.

Alloy compound	Continuous Furnace, 25 min (SIUC)	Continuous Furnace, 50 min (SIUC)	Batch Pressure Furnace, 50 min (ORNL)
	% Target Density		
IC 50 [1] †	88.6	91.6	99.8
IC 396M ††	85.5	84.5	95.6
IC 50 [2]	90.4	90.9	96.3
IC 50 [3]	89.6	92.6	94.4
TaC - IC 50	85.1	86.0	88.7
VC - IC 50	87.3	89.0	95.5
$Cr_{23}C_6$ - IC 50	76.5	75.5	95.3
Ti-48Al-2Cr-2Nb	73.4	73.2	blew up
TiB_2 - Ti-48Al-2Cr-2Nb	76.1	75.5	blew up
Mo_2C - IC 50	88.4	92.5	not sintered
TiN - IC 50	85.5	90.1	99.3
IC 50 †††	82.0	82.0	94.2

† IC 50 - Ni-Al-Zr-B (baseline)
†† IC 396M - Ni-Al- ..... ??????????????
††† Heat Treated
1 Ball milled for 89h
2 Attrition milled for 4h
3 Attrition milled for 9h

Table XII. Sintering Results for Continuously Sintered TiC Bonded with 30vol% Prealloyed Ni_3Al (baseline).

Sintering Temperature (°C)	Sintering Time 50 min (belt speed 0.75"/min)	Sintering Time 25 min (belt speed 1.5"/min)
	% Target Density	
1450	80.7	67.4
1500	89.6	79.0
1600	------	93.9

Table XIII. Sintering Results of TiC Bonded with 40vol% Prealloyed Ni3Al Milled with WC Media. Sintered at 1450°C.

Alloy compound	Continuous Furnace, 25 min (SIUC)	Continuous Furnace, 50 min (SIUC)
	% Target Density	
IC 50	81.2	88.0
Mo_2C - IC 50	84.6	87.1

Table XIV. Sintering Results of TiC Bonded with 40vol% Prealloyed Ni3Al Milled with WC Media. Sintered at 1500°C.

Alloy compound	Continuous Furnace, 25 min (SIUC)	Continuous Furnace, 50 min (SIUC)
	% Target Density	
IC 50	96.0	93.2
Mo_2C - IC 50	86.6	82.9

Table XV. Sintering Results for TiC Bonded with 30vol% Reaction Sintered Ni_3Al.

Alloy compound	1450°C		1500°C		1550°C	
	0.75"/ min	1.5"/ min	0.75"/ min	1.5"/ min	0.75"/ min	1.5"/ min
	% Target Density					
$Ni_{2.85}Fe_{0.2}Al_{0.95}$	91.0	83.6	96.3	93.1	97.3	97.4
$Ni_{1.50}Fe_{2.0}Al_{0.50}$	97.7	98.0	97.7	98.1	97.6	97.6
$Ni_{3.00}Ti_{0.2}Al_{0.80}$	84.3	81.7	96.7	93.1	96.0	98.9
$Ni_{3.00}Mo_{0.2}Al_{0.80}$	92.2	89.0	94.5	90.3	97.0	91.9
$Ni_{3.00}W_{0.2}Al_{0.80}$	90.0	87.2	91.2	88.7	93.1	88.7
$Ni_{2.40}Co_{0.6}Al_{1.00}$	95.4	94.2	90.3	94.1	95.3	94.3

Table XVI. Sintering Results for TiC Bonded with 30vol% Reaction Sintered Ni_3Al, Large Samples. Sintered 25 min at 1550°C with Belt Speed 1.5"/min

Alloy compound	% Target Density
$Ni_{2.85}Fe_{0.2}Al_{0.95}$	94.8
$Ni_{1.50}Fe_{2.0}Al_{0.50}$	97.7
$Ni_{3.00}Ti_{0.2}Al_{0.80}$	98.5
$Ni_{3.00}Mo_{0.2}Al_{0.80}$	96.2
$Ni_{3.00}W_{0.2}Al_{0.80}$	89.7
$Ni_{2.40}Co_{0.6}Al_{1.00}$	96.6

DIESEL PARTICULATE TRAP DEVELOPMENT

J. C. McLaughlin, D. Butz, R. A. Lowden, and D. P. Stinton
Oak Ridge National Laboratory
Oak Ridge, TN 37831-6063

Objectives/Scope:

Traps and filters are being developed to effectively control diesel particulate emissions from large trucks and other heavy vehicles. The particulate traps are necessary to comply with impending regulations and to alleviate public concerns over particulate emissions. An acceptable particulate trap must be efficient in removing the fine carbon particles from the exhaust gas stream, and must be able to be regenerated (cleaned) while in service. The filters must also be robust to withstand the rigors of vehicle use. Due to the high exhaust gas flows associated with heavy vehicle diesel engines, the filtration systems are large and thus can be difficult to heat resistively for regeneration. These factors necessitate the development of novel filter materials and heating means to produce an acceptable particulate removal system.

A candidate particulate removal system, conceived by Industrial Ceramic Solutions and Microwave Materials Technologies, utilizes a microwave regenerated ceramic filter system. The filter is fabricated from a flat sheet paper product composed of silicon carbide fibers, oxide fiber fillers, and various organic binders. The ceramic paper is formed into a corrugated cylindrical cartridge shape and rigidized employing a ceramic binder. The SiC fibers were included to couple with the microwaves and thus heat to regenerate the filter. Heating was found to be slower than desired and non-uniform. The corrugated structure was then coated with a thin layer of silicon carbide using chemical vapor infiltration to enhance coupling with the microwaves and thus improve heating rate and uniformity. Although initial results have been promising, the composition of the filter media, i.e. quantity of SiC fiber, and thickness and chemistry of the SiC coating, has not been optimized. It is the purpose of this task to optimize the composition and structure of the filter material for strength, coupling, uniformity and efficiency of heating, and filtration.

Technical Highlights:

As described in earlier reports, flat rectangular samples of a ceramic filter paper product, procured from Industrial Ceramic Solutions (ICS) is being infiltrated with SiC employing chemical vapor infiltration. The purpose of the infiltration is to improve the microwave coupling of the product to enhance heating rate and uniformity for use in a diesel particulate trap. Tests indicated a weight gain of ~ 27% produces the best combination of strength, stiffness, heating, and filtration. Deposition conditions and times were altered to produce the desired densities and the results are summarized in Tables 1 through 3.

Although uniformity and reproducibility have been improved as shown in the tables, there were some concerns regarding the relationship between initial paper density and weight gain after infiltration with SiC. Typically a low-density fibrous structure will gain less weight during chemical vapor infiltration than one of higher density. A higher density usually reflects higher fiber fraction thus greater surface area. The same coating deposition rate generally produces a greater weight gain in a sample of a given volume with a higher fiber content because of the greater surface area. The opposite has been observed for a portion of the filters. Higher density parts gained less weight than lower density specimens (e.g. samples 11 and 17).

Table 1. Infiltration of Filter Material with SiC (1.5 h run time)

Sample	Position in Furnace	As-Received (g)	After Binder Removal (g)	After Infiltration (g)	Wt. Gain (g)	% Wt. Gain
10	top, center	3.3164	3.3164	3.8603	0.5439	16.4
11	middle, center	3.5429	3.5429	3.9888	0.4459	12.6
12	bottom, center	3.3456	3.3456	3.9539	0.6083	18.2
Average						15.7 ± 3.3

Table 2. Infiltration of Filter Material with SiC (2.0 h run time)

Sample	Position in Furnace	As-Received (g)	After Binder Removal (g)	After Infiltration (g)	Wt. Gain (g)	% Wt. Gain
13	top, center	3.0151	3.0151	3.7772	0.7621	25.3
14	middle, center	2.9918	2.9918	3.7754	0.7836	26.2
15	bottom, center	3.7663	3.7663	4.7602	0.9939	26.4
Average						26.0 ± 5.4

Table 3. Infiltration of Filter Material with SiC (1.0 h run time)

Sample	Position in Furnace	As-Received (g)	After Binder Removal (g)	After Infiltration (g)	Wt. Gain (g)	% Wt. Gain
16	top, center	3.4108	3.4108	3.8246	0.4138	12.1
17	middle, center	3.5934	3.5934	3.9486	0.3552	9.9
18	bottom, center	2.9735	2.9735	3.4924	0.5189	17.5
Average						13.2 ± 8.2

Detailed characterization of the as-received paper and infiltrated samples has been conducted. "High density regions" were observed within the samples with the greatest pre-infiltration densities. These areas contained significant quantities of the binder used during paper processing. The binder is a preceramic polymer that is used to provide good strength and stiffness before and after heat treatment. The binder readily wets the fibers in the paper, and appears to densify some regions while sealing off others. These phenomena hinder the diffusion of gases and thus prevent the deposition of SiC. The binder also coats and bridges many of the fibers in these regions, lowering surface area. Additional ceramic paper samples with improved structures are being procured from the manufacturer.

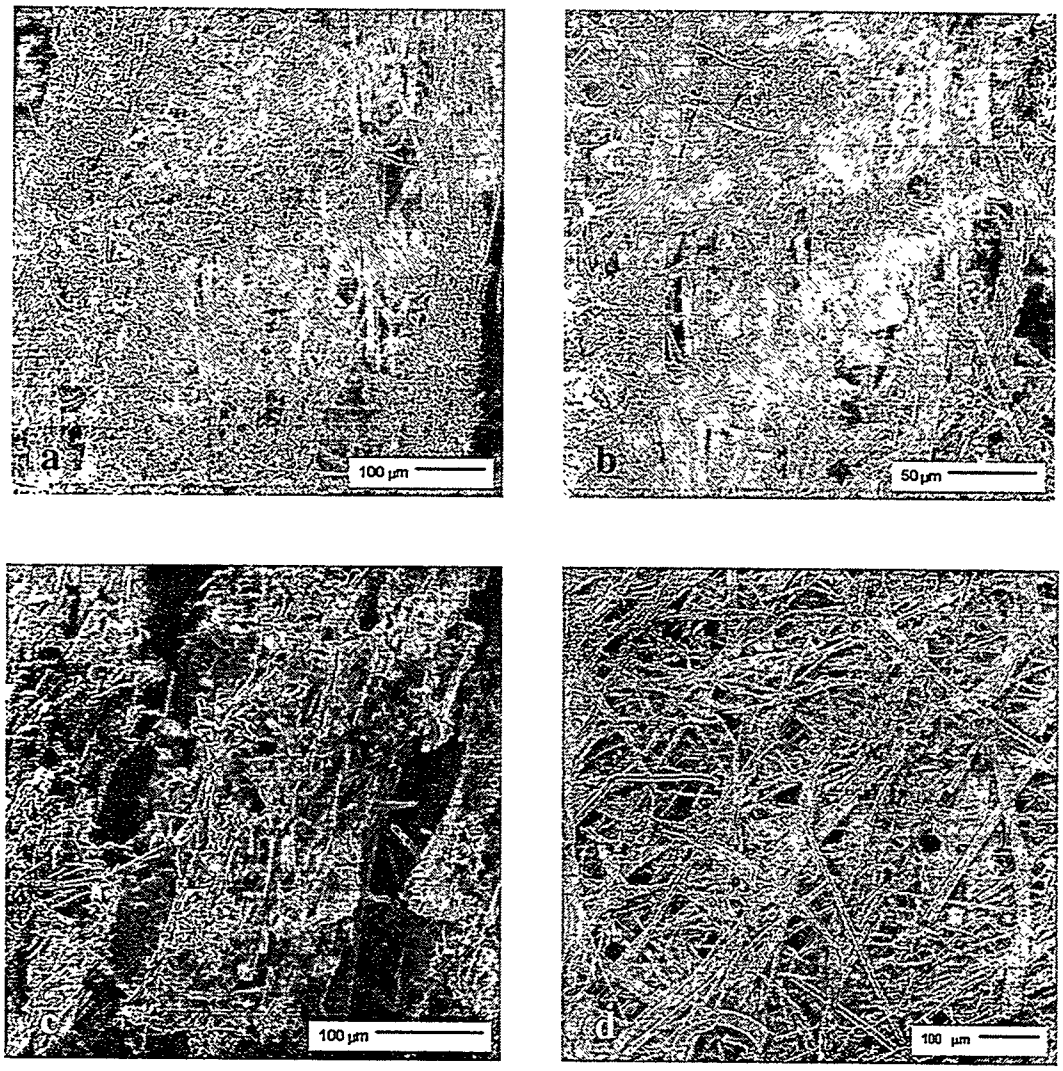

Figure 1. Photomicrographs of the ceramic paper product before and after chemical vapor deposition of a thin SiC layer: (a) cross-section before infiltration, (b) plan view before infiltration, (c) cross-section after infiltration - 26% wt. gain, and (d) plan view after infiltration – 26 % wt. gain.

Status of Milestones:

On schedule

Communications/Visits/Travel:

None

Problems:

None

Publications:

None

ADVANCED MANUFACTURING TECHNOLOGY

Durability of Diesel Engine Component Materials

Peter J. Blau, B. C. Dumont, R. D. Ott, and R. L. Martin
Oak Ridge National Laboratory

Objective/Scope

The objective of this effort is to enable the development of more durable, low-friction moving parts in diesel engines for heavy vehicle propulsion systems by conducting friction, lubrication, and wear analyses of advanced materials, surface treatments, and coatings. The scope of materials and coatings is broad and includes any metallic alloy, intermetallic compound, ceramic, or composite material which is likely to be best-suited for the given application. Parts of current interest include valves, valve guides, and scuffing-critical components, like fuel injector plungers. Hot scuffing is a primary surface damage mode of interest. Bench-scale simulations of the rubbing conditions in diesel engine environments are used to study the accumulation of surface damage, and to correlate this behavior with the properties and compositions of the surface species. The effects of mechanical, thermal, and chemical factors on scuffing and reciprocating sliding wear are being determined, and the results will be used to refine material selection strategies for durability-critical engine components.

Technical Highlights

High-Temperature Scuffing of Diesel Engine Components.

(a) High temperature scuffing test apparatus. Construction is proceeding on a new, high-temperature scuffing test rig at ORNL, but its completion has been delayed due to a re-evaluation of the design. The preliminary design of the scuffing test system utilized an actuating extension arm to rotate the specimen shaft through a preset angle. When conducting preliminary tests, significant lateral loads were apparently being applied to the load cell due to its location with respect to this extension arm. Based on this analysis, we concluded that redesigning it in such a way that the rotational motion of the shaft is converted into a purely linear motion can eliminate this problem.

After evaluating several options, Dr. Ott developed a solution, and new parts have been designed. These are being ordered or fabricated. As much of the original apparatus as possible is being retained in order to minimize the cost of the redesign and to reduce the time for completion. When construction is completed, baseline tests will be conducted at room temperature. The test temperature will then be increased toward the expected operating temperature range of 650-750° C.

(b) Characterization of materials to be used in baseline high-temperature scuffing tests. Based on discussions with diesel company engineers, four materials were selected for the initial round of tests. Obtained in rod form, these materials were microstructurally characterized by optical microscopy, scanning electron microscopy (SEM), and image analysis. The four baseline materials and their compositions are as follows:

(1) Stellite 6B™.

Chemical Analysis

Co	Cr	Ni	W	Mn	Si	Mo	Fe	N	C	S	P
Bal.	29.76	2.48	3.78	1.46	0.55	0.06	2.65	0.01	1.02	<0.01	<0.01

(2) Nitronic 60™.

Chemical Analysis

Fe	Cr	Ni	Mn	Si	C	Cu	Mo	P	S	N
bal.	16.5	8.25	8.07	4.09	0.065	0.53	0.36	0.028	0.01	0.15

(3) Gall-Tough.™

Chemical Analysis

Fe	Cr	Ni	Mn	Si	C	P	S	N
Bal.	15-18	4-6	4-6	3-4	0.15 max	0.04	0.04	0.08-0.2

(4) Silicon nitride NT-551. A commercially-produced, Si_3N_4–based, hot-pressed ceramic material with a bimodal grain size distribution.

The Vickers micro-indentation hardness numbers of the four materials, are as follows:

Table 1. Vickers Microindentation Hardness* of Specimen Materials

Material	Average HV (GPa)	Standard deviation (GPa)
Stellite 6B™	4.65	0.30
Nitronic 60™	2.91	0.09
Gall-Tough™	3.01	0.10
NT-551	16.13	0.92

*300 grams-force indenter load

Reciprocating, Crossed-cylinders Wear Test Method is Developed

A new, reciprocating crossed cylinders test method has been developed in order to obtain preliminary wear data on candidate anti-scuffing materials. Fixtures have been fabricated to allow a current ORNL wear testing machine to be used conduct these experiments using the same size and type of specimen that will be used in the high-temperature scuffing apparatus. Wear measurements are performed using a laser-based surface profiling system. Wear tests are currently being conducted on the four materials described above. Results will be provided in future reports.

New Staff Member Joins the Project..

Dr. Ronald D. Ott, a new ORNL staff engineer, has joined the project team. Dr. Ott received a B.S. degree in mechanical engineering, and M.S. and Ph.D. degrees in Materials Science from the University of Alabama at Birmingham. From 1994-97, he was a Graduate Fellow at the High Temperature Materials Laboratory where he conducted dissertation-oriented research on the statistical evaluation of machining effects on sub-surface damage to structural ceramics. Prior to joining ORNL in August, he was a Post Doctoral Research Engineer at the University of Alabama, Center for Materials for Information Technology, where he performed studies to optimize thin film overcoats for rigid magnetic hard disks. His work at ORNL will focus on tribology, surface micro-mechanics, and machining technology. He is now participating in the design and use of the scuffing testing system for selecting wear-critical diesel engine materials.

Future Plans

a) Re-design work for the high-temperature, oscillatory scuffing rig will continue and baseline tests will be started as soon as the construction is complete.

b) A series of reciprocating crossed-cylinders wear tests on four candidate anti-scuffing materials will be completed within the next reporting period.

b) P. Blau will attend a boundary lubrication focused workshop at Caterpillar, Inc., and present an invited talk on running-in.

Status of Milestones

Completion of the baseline tests has been delayed pending the redesign and construction of the high-temperature scuffing test system, as described above.

Communications/Visitors/Travel

None

Problems Encountered

None

Publications and Presentations

1. B. Dumont, P. J. Blau, and G. M. Crosbie* (1999) "Reciprocating Friction and Wear of Two Silicon Nitride-Based Ceramics Against Type 316 Stainless Steel," was accepted for publication in *Wear* (* Ford Motor Company, Dearborn, Michigan.)

Laser Scatter Methods for Detecting Subsurface Machining Damage in Ceramics – Jiangang Sun, William A. Ellingson, (Argonne National Laboratory), and Rajan Tandon (Caterpillar Inc.)

Objective/scope

Emission reduction in diesel engines designated to burn fuels from several sources has lead to the need to assess ceramic valves to reduce corrosion and emission. Machining costs remain the single most costly item in production. The primary objective of this program is to develop a laser-based elastic optical scattering procedure which would provide a direct (near real-time) method to detect machining induced damage in monolithic ceramics. Median and lateral crack detection are of primary importance. The laser-based elastic optical scattering program is being executed in three steps. The first step is to optimize the elastic scattering procedure by examining specimens machined using innovative machining techniques. The second step involves correlation of the elastic scattering results with mechanical properties in "real" machined ceramic specimens. The final step involves the development of a prototype instrument to be evaluated for on-line implementation in a production environment.

Technical progress

1. Calibration of New Tunable Laser

During this period we purchased a new motorized monochromater. This monochromater can determine the spectral intensity of the laser beam in a specified wavelength range with complete computer control. Its primary wavelength region is between 450 and 1600 nm and wavelength resolution is 0.5 nm. We have developed a LabView program for automated data acquisition for this monochromater. This new monochromater was then used to calibrate the wavelength of the Ti:sapphire tunable laser. Currently, the first optics set is installed in the tunable laser, which allows for wavelength tuning between 700 and 850 nm with a micrometer setting between 0 and 8. Figure 1 shows a typical spectral distribution of the laser beam when the micrometer setting is placed at 4. The central beam wavelength is determined at 797.5 nm and the band width at ~2.5 nm. Calibration curves of the laser wavelength with the micrometer setting are shown in Fig. 2, including a generic curve from the manufacturer, a curve measured with an older model monochromater, and the curve measured by the new motorized monochromater. It is seen that the new experimental data are much more consistent than the older data, but they are approximately same.

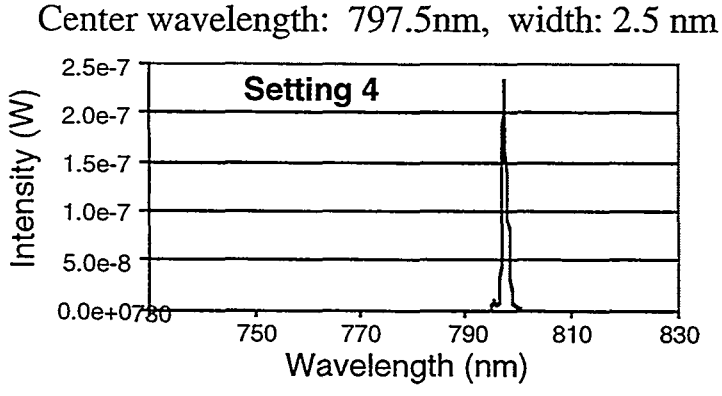

Figure 1. Wavelength distribution of Ti:sapphire laser output measured with the new motorized monochromater.

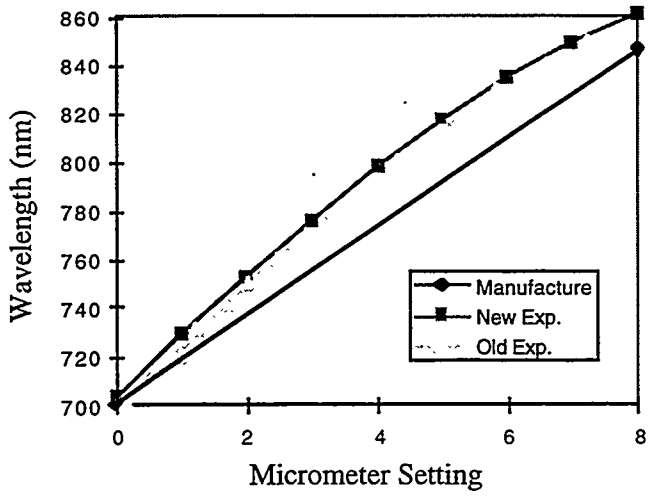

Figure 2. Wavelength calibration curves of the CW Ti:sapphire laser.

2. Optical Transmission of Si_3N_4 Ceramics

The Ti:sapphire tunable laser was used to determine optical transmittance as functions of wavelength and depth of penetration with step-wedges of several Si_3N_4 materials. Our previous transmission study showed that optical transmission, and hence penetration depth, increases with wavelength. If this were true, longer wavelengths could detect deeper defects, thereby increasing detection sensitivity.

The theoretical equation that governs how light is transmitted through a material is as follows:

$$I(x) = I_o * e^{-\alpha x} \tag{1}$$

where I_o is the initial intensity of the light entering the material, I(x) is the transmitted intensity of the light that leaves the material, α is the linear attenuation coefficient, and x is the thickness of the material through which the light is propagating. Equation (1) can be written as

$$\text{Ln}\,(I(x) / I_o) = -\alpha x \tag{2}$$

The experimental setup is shown in Fig. 3. The laser light was directed into an attenuating beam splitter to reduce the initial intensity of the beam. The light was then coupled into a fiber optic cable and exited the cable through a collimating lens. The light was then incident upon the step-wedged ceramic sample. The transmitted light finally entered the integrating sphere where the light intensity is measured by an optical detector.

Figure 4 shows the optical transmission results for Ceralloy 147 and SiAlON Si_3N_4 ceramics. The linearly fitted lines follow Eq. (2). It is evident that transmitted intensity increases as the wavelength is increased at all depths for both materials. In the Ceralloy 147 sample, some of the points are not completely on the regression line. This is due to a small curvature of the sample. This curvature does not allow for the sample to be placed flat against the integrating sphere. Consequently, the data points will respond to this curvature with a small fluctuation.

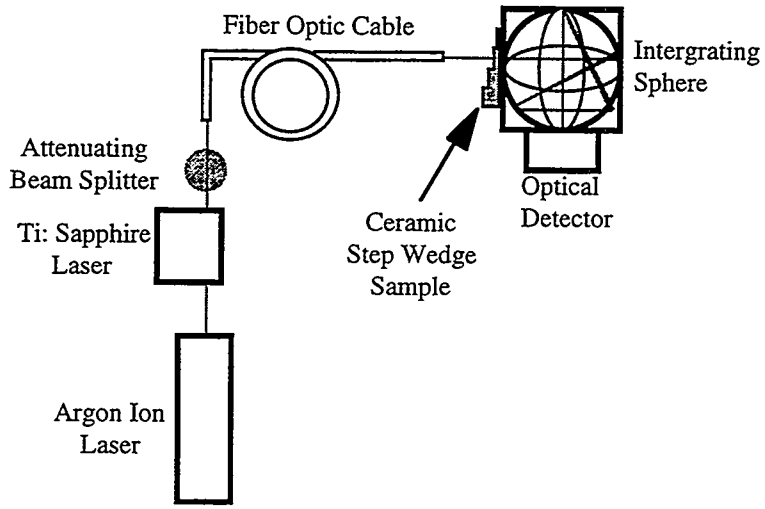

Figure 3. Experimental setup for measuring optical transmission of step wedges of ceramic materials.

Figure 5 shows the linear attenuation coefficient α as a function of wavelength for Ceralloy 147 and SiAlON Si_3N_4 ceramics. The trend in these data indicates that, over this wavelength range, the magnitude of the linear attenuation coefficient decreases with the wavelength, or there is less attenuation at longer wavelengths. This result is consistent with our previous observation.

The data shown in Figs. 4 and 5 cover a wavelength range of 633 through 850 nm. When the second optics set for the Ti:sapphire laser is installed, the optical transmission data over the wavelength between 850 and 1000 nm will be obtained.

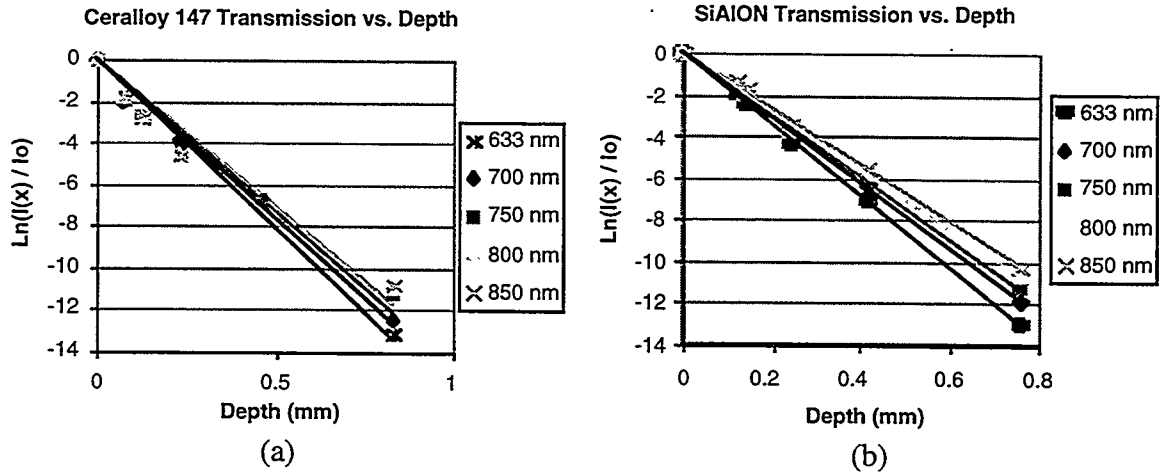

Figure 4. Optical transmission as a function of specimen thickness for (a) Ceralloy 147 and (b) SiAlON Si_3N_4 ceramics.

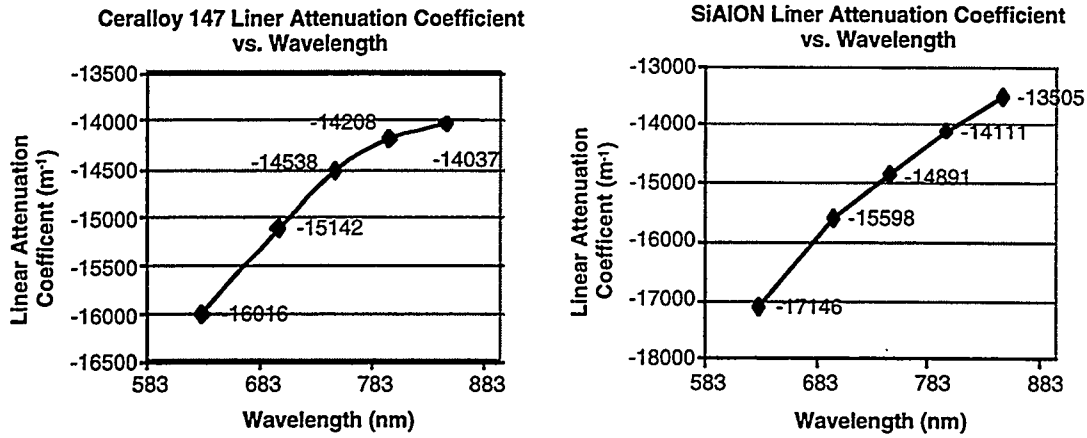

Figure 5. Linear attenuation coefficient α as a function of wavelength for (a) Ceralloy 147 and (b) SiAlON Si_3N_4 ceramics.

3. Elastic Optical Scattering Results

Our current laser scatter system was designed for use with an optical wavelength of 633 nm, i.e., for He-Ne lasers. The optical components have narrow-wavelength band and will lose their efficiency significantly when the wavelength is changed. Therefore, broad-band (700 to 1000 nm) optical components are needed to setup a new laser scatter system for the Ti:sapphire tunable laser. During this period we have ordered and received new broad-band optics and assembled a new laser scatter system.

The first tests we conducted were measurement of subsurface back-scattered light as a function of ceramic thickness using a set of step-wedge samples as shown in Fig. 6. These tests also serve as detection of subsurface lateral cracks at various depths. As illustrated in Fig. 6, while the front surface appeared uniform across the entire wedge, the steps machined into the back surface provided a ceramic/air interface in the subsurface material to simulate a subsurface lateral crack. Figure 7 shows the scatter (sum) images of three Si_3N_4 ceramic step-wedges of GS44, NT164, and SiAlON obtained previously with the He-Ne laser (at wavelength 633 nm), with the images of the thinnest steps on the left, and Fig. 8 shows the corresponding images obtained with the new Ti:sapphire laser at wavelength 850 nm.

Figure 9 plots the averaged back-scattered intensity at wavelengths of 700 and 850 nm for these three ceramics as a function of thickness with best-fit lines to an exponential attenuation behavior. The intensity was normalized by the asymptotic value when the depth approaches infinity. Although this inspection indicates the relative interaction of a ceramic/air interface beneath the surface of a ceramic component, it is only an approximation of a subsurface crack or pore. If an actual lateral defect were present in the subsurface material, the increase in back-scattered intensity would be even greater, owing to the additional scatter from the material beneath the defect.

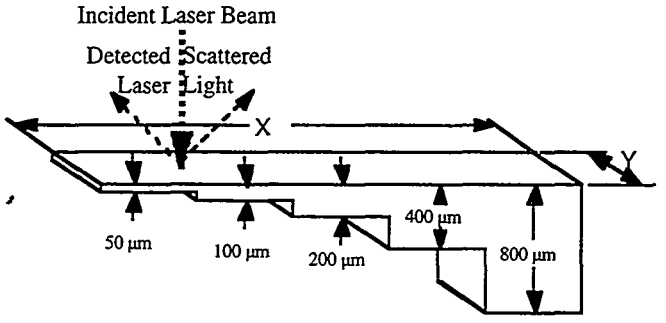

Figure 6. Drawing of a step-wedge used to determine subsurface-lateral-defect sensitivity of laser scatter analysis.

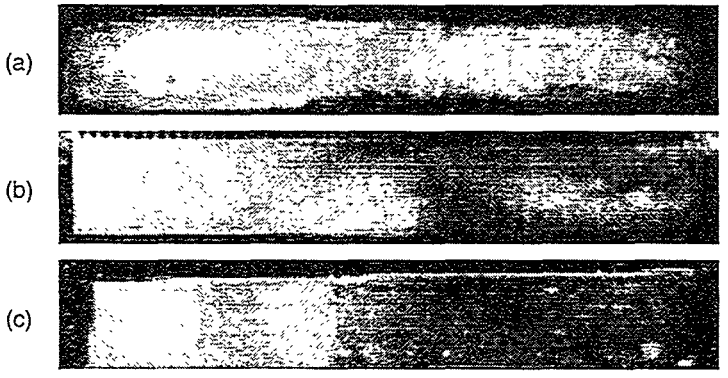

Figure 7. Subsurface laser scatter images of three Si_3N_4 step-wedges obtained at wavelength of 633 nm: (a) GS-44, (b) NT164, and (c) SiAlON.

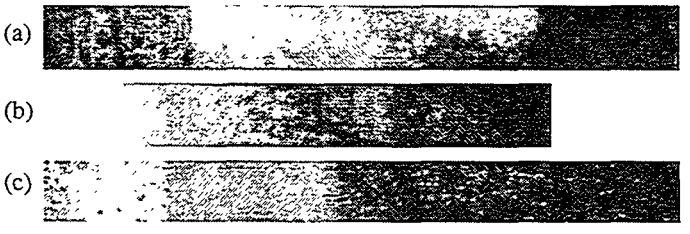

Figure 8. Subsurface laser scatter images of three Si_3N_4 step-wedges obtained at wavelength of 850 nm: (a) GS-44, (b) NT164, and (c) SiAlON.

Two trends of the measured data can be observed from Fig. 9. (1) The back-scattered light intensity decreases when the depth becomes very thin. This is because there is not enough material to produce scatter light back to the detectors when the material is too thin. The intensity decrease occurs for GS44 ceramic when the thickness is <123 μm at both wavelengths 700 and 850 nm, and an indication of this trend is seen for SiAlON at the wavelength 850 nm. (2) The back-scattered intensity increases with the increase of the laser wavelength, especially in the thicker materials. For GS44 ceramic, for example, when the step thickness is >120 μm the detected back-scatter intensities (above the background intensity or the asymptotic value) at 850 nm wavelength are considerably higher than those obtained at 700 nm. For other two materials, similar results can be found. This result indicates that longer wavelength light has higher sensitivity on detecting deeper defects within the subsurface of ceramics.

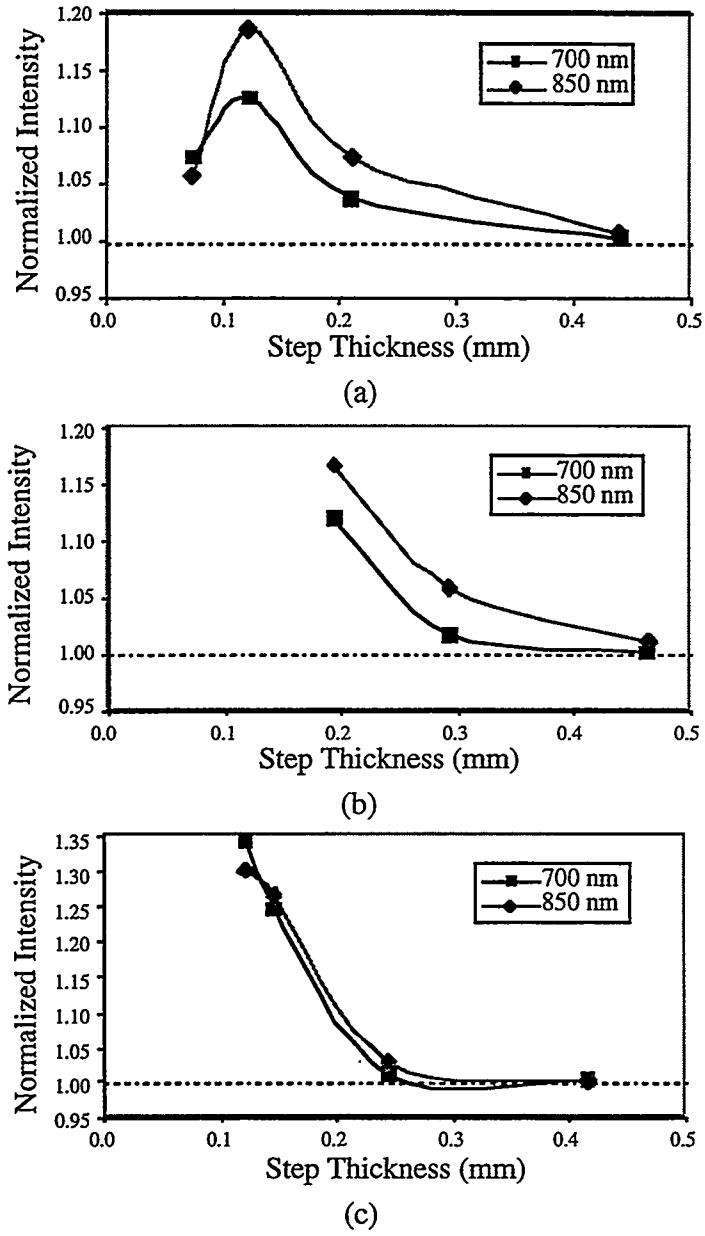

Figure 9. Plots of back-scattered intensity as a function of subsurface interface depth for ceramics (a) GS-44, (b) NT164, and (c) SiAlON.

Currently we are preparing to change the optics in the Ti:sapphire laser so that the laser can be operated in the wavelength range of 850 nm to 1000 nm. The laser scatter system will then be setup after this modification. We expect that the wavelength effect on defect depth detection will be most sensitive at the higher wavelengths. This work will be reported in the next period.

A meeting has been arranged with Dr. R. Tandon of Caterpillar, Inc. in Mossville, IL on October 4th. We will discuss the direction and details of the collaborative works between ANL and CAT during this meeting. A modified milestone schedule for the current project will be derived from these discussions.

4. Automation for On-Line Inspection with Optical Scattering

   We did not devote any effort to this part of the project this period.

5. Impact Acoustic Resonance

   We did not devote any effort to this part of the project this period.

Status of Milestones

Current ANL milestones are on or ahead of schedule.

Communications/Visits/Travel

Travel:

1. W. A. Ellingson J. G. Sun will visit Caterpillar Technical Center in Mossville, IL on October 4th to discuss project details.

Communication:

1. Discussions have been taking place with Eaton Corporation and St. Gobain Industrial Ceramics to obtain additional machined specimens with carefully controlled machining conditions.

Problems Encountered

None this period.

Publications

J. G. Sun, W. A. Ellingson, J. S. Steckenrider, and S. Ahuja, 1999, "Application of Optical Scattering Methods to Detect Damage in Ceramics," in *Machining of Ceramics and Composites*, Part IV: Chapter 19, eds. S. Jahanmir, M. Ramulu, and P. Koshy, Marcel Dekker, New York, pp. 669-699.

E. Z. Zanoria, T. R. Watkins, K. Breder, L. Riester, M. Bashkansky, J. Reintjes, J. G. Sun, W. A. Ellingson, and P. J. Blau, 1998, "Assessment of Techniques for Characterizing the Surface Quality of Ground Silicon Nitride," *J. Mat. Eng. & Performance*, Vol. 7, No. 4, pp. 533-547.

J. G. Sun, M. H. Haselkorn, and W. A. Ellingson, 1998, "Laser Scattering Detection of Machining-Induced Damage in Si_3N_4 Components," in *Nondestructive Characterization of Materials VIII*, ed. R. E. Green Jr., Plenum Press, New York, pp. 365-370.

W. A. Ellingson, J. A. Todd, and J. G. Sun, Optical Method and Apparatus for Detection of Defects and Microstructural Changes in Ceramics and Ceramic Coatings, applied for a U.S. patent in May 1999.

INTERMETALLIC-BONDED CERMETS

P. F. Becher and C. G. Westmoreland
Oak Ridge National Laboratory
Oak Ridge, TN 37831-6068

Objective /Scope

The goal of this task is to develop materials for diesel engine applications, specifically for fuel delivery systems and wear components (e.g., valve seats and turbocharger components). This will require materials with a minimum hardness of 11 GPa and a thermal expansion coefficient of between 10 to 15 x 10^{-6}/°C over the temperature range of 25° to 300°C. The material should also have excellent corrosion resistance in a diesel engine environment, a flexure strength in excess of 700 MPa, and a fracture toughness greater than 10 MPa$\sqrt{m}$ to ensure long term reliability. The material should also be compatible with and not cause excessive wear of the steel counter face. The upper temperature limit for fuel delivery systems applications is 540°C, and for the other wear applications, the limit is 815°C. Finally, the total material processing costs for these advanced materials should be competitive with competing technologies such as TiN or other ceramic coatings on high speed tool steels.

Technical Highlights

Recent processing studies have focused on achieving full density in TiC-Ni_3Al cermets that have submicron TiC grain sizes and contain up to 40 vol. % Ni_3Al binder phase by pressureless sintering at temperatures $\leq$ 1450°C. In the April 1999 Bimonthly Report, we showed that the addition of < 2 wt. % molybdenum to the cermet did enhance the wetting of the submicron TiC powders by the Ni_3Al and improve its sinterability. However, medium pressure (~ 15 MPa) hot pressing still had to be employed to obtain fully dense cermets with Ni_3Al contents of 40 vol. %. This stimulated studies of the influence of TiC powder characteristics on the pressureless sintering behavior of the cermets.

The sinterability of the cermets produced from two commercial and several experimental submicron TiC powders have been evaluated in comparison to a commercial fine (~2 micron) TiC powder. The characteristics of these powders are shown in Table I. It became apparent that the sintering behavior of the cermets was influenced by the TiC powder characteristics. Initial trials with the attritor milled JNM submicron TiC powder revealed that the melt infiltration sintering process that proved so successful with cold pressed preforms of the Kennametal 001-767 powder was going to have to be modified if not abandoned. However, subsequent studies using the JNM-007 TiC powder were successful in sintering mixed powder preforms containing ~ 2 wt. % molybdenum that had been cold isostatically pressed to increase the green densities. Fully dense cermets with submicron TiC grain sizes and Ni_3Al contents of 40 vol. % have now been achieved by pressureless sintering in a mild vacuum at $\leq$ 1450°C. This was achieved by

sintering a preform prepared by ball milling JNM TiC-007 powder plus 2 wt. % Mo with alloy powder (IC-50), followed by cold uniaxial pressing the mixture at ~ 100 MPa and finally cold isostatically pressing at ~ 200 MPa. There was evidence for TiC grain growth with increase in sintering temperature, but submicron TiC grain sizes were achieved even with a sintering temperature of 1450°C.

However, this was not the case with the Furukawa TiC grade N powders. This powder was found to contain a significant fraction of agglomerates which caused the green density of the cermets to be low (Note that the other powders did not exhibit extensive or hard agglomerates). Attritor milling was used reduced these. Even after eliminating the agglomerates in the Furukawa TiC-N powder, the sintered densities of cermets of the same compositions were consistently lower as compared to those achieved with the JNM TiC-007 powder, Figure 1.

The experimental submicron TiC powder could be densified but required increased sintering temperatures, which lead to significant grain growth. The result being that the TiC grain sizes in the cermets were ~ 5 μm instead of the submicron TiC grain size desired.

The question then arose as why the densification response of the cermets was diminished in these two cases. Two features of the powder could be responsible. Both the presence of hard agglomerates and increased the oxygen content of these powders could hinder densification. This was suggested due to the fact that the as-received experimental powders exhibited high oxygen contents, and the Furukawa powder contained large agglomerates. To test, the Kennametal powder was attritor milled to reduce its average particle size. After attritor milling the Kennametal 001-767 TiC powder size was reduced the mean particle size to ~ 0.5 μ, which is similar to that of both the commercial submicron TiC powders. However, the oxygen content of the powder increased to 3.9 wt. %. The densities of cermets produced with this submicron Kennametal TiC powder were $\leq$ 90 % of theoretical. Thus, it would appear that TiC powders with both submicron particle size and lower oxygen content (< 3 wt. %) are required.

To date, the wear and scuffing results for the TiC-Ni_3Al cermets are very promising. The excellent wear response of these cermets is also combined with the high toughness and fracture strengths. However, a key aspect of the application of the TiC-based cermets is the economics of the raw materials and fabrication procedures. The success of quite standard powder metallurgical processing methods combined with pressureless sintering demonstrated in the fabrication of dense TiC cermets containing up to 40 vol. % Ni_3Al is very encouraging as these offer low cost approaches. The cost of raw materials, especially submicron TiC powders, is certainly a critical aspect. The costs of the submicron TiC powders that have been available are at least an order of magnitude too high. Current studies are concerned with producing lower cost submicron TiC powders with sufficiently low oxygen contents (< 3 wt. %) to fabricate dense cermets by pressureless sintering. Initial work has explored the effects milling low cost commercial powders with typical mean particle sizes 0f ~ 2 μm. Attritor milling using fine grained yttria stabilized zirconia milling media in isopropanol has shown promise by reducing the ratio of TiC powder to milling media. Substitution of higher density tungsten carbide media in place of zirconia will be examined next to enhance the milling process. Other options for milling commercial, low cost TiC powders are also being explored with powder suppliers.

Table I. Characteristics of TiC Powders

TiC	Total C Wt. %	As-Received Oxygen Wt. %	As-Received Mean Particle Size µm	Mean Size, µm Attritor Milled 4–8 h	Wt. % Oxygen Attritor Milled 4–8 h
Commercial					
Submicron					
JNM TiC-007	19	1.7	0.85	–	–
Furukawa TiC-N	19.4	1.6	1.1 Agglomerates	0.5	–
Experimental	19.6	2.63	0.3	–	–
Fine					
Kennametal TiC-001-767		0.7	2.6	0.5	3.9

- Data from powder producer.

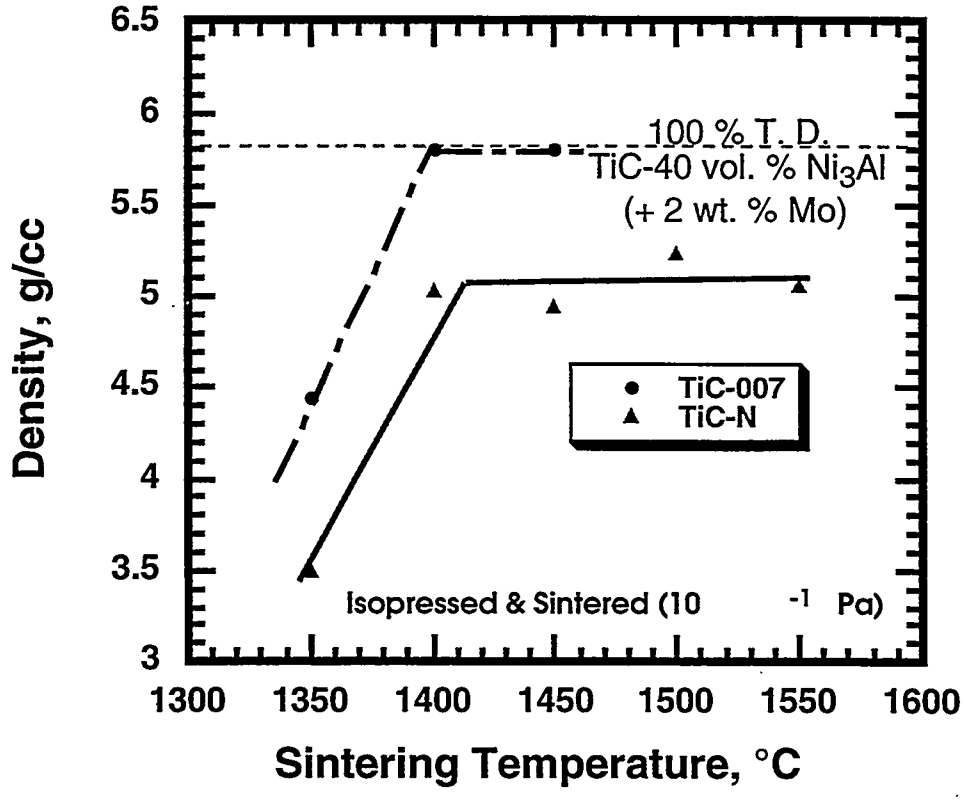

Figure 1. Sintering response of commercial submicron TiC powders.

Status of Milestones
On Schedule

Communication/Visits/Travel
Review meeting was held (08/18/99) with Tom Yonushonis and Paul Becker of Cummins Engine Company, Jim Stephan of Advanced Technologies, and Terry Tiegs of ORNL to discuss progress on processing of cermet materials.

Problem Encountered
None

Publications
None

COST EFFECTIVE MACHINING OF CERAMIC ENGINE COMPONENTS

S. B. McSpadden, Jr.
T. O. Morris

Oak Ridge National Laboratory
Box 2008, Building 4515
Oak Ridge, Tennessee 37831-6069

Objective/Scope

To develop and demonstrate optimized, cost-effective grinding processes for the production of ceramic components for use in diesel engines.

Technical Highlights

Long-Term Performance Testing of the Norton Sceptre™ Metal Bond Diamond Grinding Wheel on the Weldon Cylindrical Grinder

The Norton Sceptre™ Metal Bond diamond grinding wheel is a commercially available product developed during a five-year, multiphase, cooperative project between Norton Company and the DOE Office of Transportation Technology as part of the Cost Effective Ceramic Machining initiative. (The project was entitled *Innovative Grinding Wheel Design for Cost-Effective Machining of Advanced Ceramics,* as described in Request for Proposal No. SM037-87.)

Tests were performed at the Oak Ridge National Laboratory's Machining and Inspection Research User Center to investigate the long-term behavior of the wheel while grinding advanced ceramic materials under aggressive conditions. These tests were in addition to extensive in-house and external beta testing that had already been performed during the development of the wheel. The tests were conducted jointly by Norton and ORNL personnel under the High Temperature Materials Laboratory (HTML) User Program. Norton Company was particularly interested in demonstrating that the segmental design of the wheel would provide consistent performance over the life of the wheel in terms of gradients within the segments.

Long-term grinding tests were performed using the Weldon Model AGN5 cylindrical grinder shown in Figure 1(a). The tests were conducted in approximately 20-hour stages, with a dimensional inspection of the wheel profile at the end of each 20-hour period.

Cylindrical grinding of silicon nitride button-head tensile rod specimens was selected as a particularly demanding application because it includes both straight OD-plunge grinding and OD-contour grinding. This type of grinding operation taxes both the flat sections and the leading edge of the wheel. Because the test parts are real-world components with complex geometry rather than simple cylindrical shapes, the resulting data are much more difficult to analyze. For example, wheel wear and grinding ratio measurements involved the analysis of complex profiles rather than measurement of simple steps. The composite material removal rate (MRR) is also difficult to compute because the grinding cycle involves complex paths, dwell times, direction reversals, and changes in traverse rate. Although an attempt was made to analyze and present data for G-ratios, MRR, etc., many of the results of this test are qualitative. Setup of the specimens on the Weldon grinder is shown in Figure 1(b).

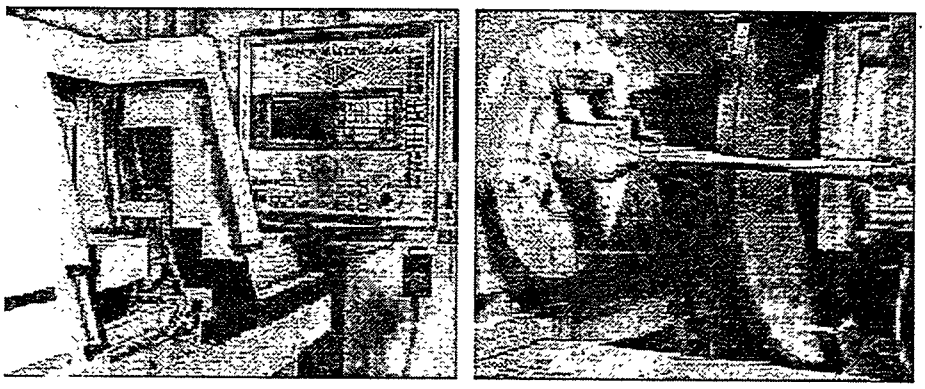

Figure 1(a). The Weldon Model AGN5 Cylindrical Grinder at the ORNL Machining and Inspection Research User Center. 1(b). Silicon nitride button head tensile specimens being profile-ground between centers on the Weldon cylindrical grinder.

The experimental parameters are shown in Table 1. During the course of the experiment, force, power, and spindle vibration were monitored periodically using Labview™-based instrumentation. Part roundness, size and surface inish were also monitored.

Table 1. ORNL Experimental Parameters.

Wheel Description	Norton Scepter™ 1A1SA; Norton Number: D-2MXL1994-.25	
Wheel Size	16 in. diameter X 0.5 in. wide X 5.0002 bore	
Workpiece Material	Allied Signal GS-44 Si_3N_4 (high-performance silicon nitride)	
Spindle Speed	16000 SFPM (3820 RPM)	
Typical conditions during plunge grinding mode	In-feed rate: Up to 2.0 inch/minute over 0.375" width ($0.94\ in^3$ / min MRR in GS-44 Si_3N_4)	
Typical conditions during profile grinding mode	Straight path: 25 in./min. 0.001 in. depth of grind	Contour path: 4 in./min. 0.001 in. depth of grind
Coolant	Type: Milacron Cimtech™ 500, approximately 20:1	
	Flow rate: Approximately 16 gal./min	
Truing Procedure (using hydraulic rotary truing device)	Truing interval:	At initial setup only
	Truing wheel speed:	2400 RPM
	Grinding wheel speed:	1000 RPM
	In-feed:	0.0002" per pass
	Traverse rate	5 inches per minute
	Roll type	Beck 4" diameter roll #SDW10042-1 with 0.125" corner radius.
Dressing Procedure (using Norton 38A 220-HVBE dressing stick)	Stick dress after initial truing, and then only as needed	

One of the most important facets of the test was the determination of grinding ratios (volume of workpiece material removed divided by the change in volume of wheel). The wheel exhibited an extremely low wear rate throughout the tests, which made accurate calculation of G-ratios difficult. The parts were weighed at the beginning and end of each grinding operation. Knowing the density of the

workpiece, the volume of material removed during the test could be easily calculated. The profile of the grinding wheel was measured on a very accurate coordinate measuring machine (CMM) at the beginning of the test, and approximately every twenty hours thereafter. The differences in profile geometry were used to calculate the volume of abrasive material removed from the wheel. An attempt was made to calculate the G-ratio from these measurements. Results calculated after 40 and 60 hours 3110 and 3500, respectively. Due to difficulties in measuring the wheel profile, measurement uncertainty was a significant concern. For this reason, results are not presented for the 20 and 80-hour measurements. For the 80-hour measurement, the measured wheel wear was less than the measurement uncertainty of the CMM. The measurement indicated (erroneously) that the wheel cross-section actually *increased* in size between the 60 and the 80-hour measurement. Such results indicate the need for improved techniques for measuring wheel wear in a laboratory environment.

At the end of approximately 80 hours of grinding, the wheel was sent back to Norton Company for non-destructive evaluation of the wheel's condition. No abnormalities were detected. Because the wheel wear was extremely low up to this point, approximately 0.100 inch of abrasive material was deliberately removed from the wheel at Norton in order to evaluate consistency of wheel performance throughout the life of the abrasive. The wheel was then returned to ORNL for further testing.

Subsequent testing of the wheel consisted of approximately 10 hours of plunge grinding into Si_3N_4 specimens at in-feed rates of up to 2.0 inches per minute. This corresponded to a material removal rate of approximately 2.5 in^3/in of wheel width. Measured values for spindle horsepower as a function of in-feed rate are shown in Figure 2.

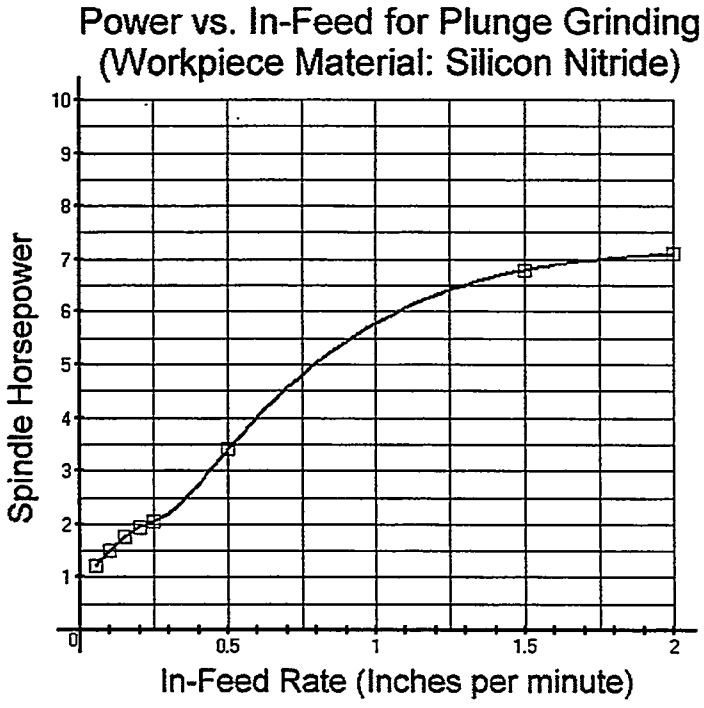

Figure 2. Spindle power as a function of in-feed rate.

Conclusions from the ORNL tests

- The wheel performed well throughout the tests, needing only occasional dressing.
- The wheel appears to have excellent form-holding characteristics.
- The calculated grinding ratios were consistently very high. (Some measurements yielded results as high as 8,000 on silicon nitride. However, accurate measurements were very difficult to achieve because of the extremely low wheel wear.)
- Part geometry and surface finish were at least as good as we typically achieve with vitrified bond diamond wheels.

The design and performance goals for the Scepter™ Diamond Wheel were met, and it is now commercially available from Norton Company. Extensive testing has demonstrated that the wheel's capability and performance in grinding a variety of ceramics surpasses that of both vitrified and resin bonded wheels, and that wheel life over resin counterparts is greatly extended. Because of these demonstrated advantages, Norton Company believes that the market will embrace the wheel as the "wheel of choice" for grinding engineered ceramics.

Cummins Engine CRADA Extended

An existing CRADA with Cummins Engine Company Fuel Systems Division has been extended for 24 months to allow a more in-depth investigation of the machining characteristics of Zirconia used in fuel system components. Activities will include machining under various conditions, as well as mechanical properties characterization, tribological studies, and residual stress studies. Current machining efforts in the Cummins CRADA are oriented toward process improvements in their fuel systems area.

Caterpillar CRADA Activities Continue

The machining portion of the CRADA with Caterpillar Incorporated is proceeding as outlined. The machining to date has consisted of evaluating several machining parameters (down feed, table speed, wheel surface speed, and abrasive diamond grit size of the grinding wheels) that comprise three different machining conditions on the Nicco creep feed surface grinder. Residual stress measurements were made on several samples to rank the severity of the machining conditions by evaluating the degree of sub-surface compressive and tensile stresses introduced by the machining process

The experimental trihedral, vertical spindle, ultrasonic machining center was received from Caterpillar. Ownership of this machine was transferred to the HTML's Machining and Inspection Research User Center as part of Caterpillar's in-kind contribution to the recently expanded CRADA with ORNL. This machine has been installed and tested for correct operation. Minor modifications are being made, including the addition of a small heat exchanger in the hydraulic system to prevent overheating after prolonged operation.

Mr. Jeff Bougher, of Caterpillar, participated in machining activities during his visit to the HTML in August. He received first hand experience, which provided him insight on the procedures involved in machining ceramics. Another area of interest to Caterpillar and to the HTML is the condition of the grinding wheel prior and subsequent to the machining of the ceramic components. A technique has been developed using dental impression material that allows an imprint of the grinding wheel to be made quickly, without removing the wheel from the spindle. Caterpillar is currently evaluating the technique by examining wheel segments and their mating imprints using scanning electron microscopy (SEM) and the Rodenstock laser surface profiling instrument. This allows a direct comparison of the mating surfaces and will determine the validity of the technique. The results from the wheel/imprint comparison will be prepared for publication.

Equipment Upgrades

Two dimensional inspection instruments are being upgraded to add new capabilities and to replace obsolete computer systems that were not Y2K-compliant. The Legend Integrated Metrology Center (a coordinate measuring machine) was outfitted with a new computer, new motion controller boards, and new control/analysis software. The instrument is back in service and its performance has improved dramatically. The Taylor Hobson Talysurf Series 100 Surface Profile Analyzer was returned to the factory for repair and upgrade. The instrument should be back in service within the next two months.

Consignment agreements were finalized with Cincinnati Machine Tool and with Milacron, Inc. who are now separate organizations since the sale of the Machine Tool Division by the old Cincinnati Milacron Marketing Company to UNOVA. These consignments involve the loan to ORNL of a RK Centerless Grinder by Milacron, Inc. and a Sabre Vertical Spindle Grinder by Cincinnati Machine tool.

Communications/Visits/Travel

Lawrence O'Rourke visited Caterpillar to receive training on an experimental trihedral, tripod, 3-axis, ultrasonic machining center. Ownership of this equipment is is being transferred to the HTML's Machining and Inspection Research User Center as part of Caterpillar's in-kind contribution to the recently expanded CRADA with ORNL. The machine will be used for general ceramic machining studies, and may be extremely useful for small hole drilling in ceramic materials.

Darryl Gust, of Cummins Engine Company, visited the HTML to discuss elements of the recently extended Cummins CRADA. Mike Bowling, also of Cummins, visited the HTML to participate in ongoing machining studies being conducted jointly by Cummins, the HTML, and Dr. Albert Shih, of North Carolina State University.

Joe Piccone and Keoni Denison, of Norton Company, visited the HTML to participate in long-term testing of the Sceptre™ metal bonded diamond grinding wheel.

Jeff Bougher of Caterpillar made several visits to the HTML to coordinate the CRADA efforts and to participate in ongoing machining studies.

Mike Bowling of Cummins Engine visited the HTML several times to participate in CRADA activities involving process improvements in the machining of fuel system components.

Sam McSpadden and Lawrence O'Rourke visited Milacron, Inc., in Cincinnati to discuss the manufacture of superabrasive grinding wheels and to tour the coolant test Milacron's coolant test facilities. Sam McSpadden visited the University of Massachusetts to hear a doctoral dissertation based on the "Smart grinding wheel."

Publications

None.

TESTING AND CHARACTERIZATION

Task Title: Computed Tomography
Principle: W. A. Ellingson, R. Koehl, H.R. Lee, H.P. Engle, Argonne National Laboratory

Objective/Scope

The primary objective of this work is to develop nondestructive evaluation/characterization (NDE/C) technology to: (1) assure reliability of fabrication of advanced materials and manufacturing methods; (2) provide a method for reliable component surveillance during use; and, (3) as a method to provide data for lifetime prediction. These efforts are focused on materials for reciprocating engines as part of the heavy vehicle propulsion materials effort. Initially effort was focused on aspects of valve train technology in a cooperative effort with Caterpillar and Honeywell Ceramic components (Formerly AlliedSignal ceramic Components. Specifically, use of ceramic valve guides was under consideration as means to develop a self-lubricating valve guide. Another part of this work has been to begin to develop collaborations with industrial partners to address fuel delivery aspects of reciprocating engines primarily as part of advanced manufacturing technology. Use of femto-second lasers for example for drilling holes in fuel injector nozzles is one subject of interest. NDE/C development for fuel delivery systems has now become the focus of this work and will be the focus of future reports.

Technical Highlights

The technical highlights will be described in two main areas: (1) a discussion of the CRADA work on the amorphous silicon X-ray detector, and (2) completion of the X-ray densitomtery of the GS-44/Chopped carbon fiber valve guides.

1. CRADA—
Evaluation of an Amorphous Silicon X-ray Imaging Detector

A. MX-1024 flat-panel detector

A.1. Spatial resolution produced by MX-1024 detector

Image resolution of the detector was determined by its modulation transfer function (MTF). A line pair (LP) phantom was used, as shown in Fig. 1-a, which is the normalized X-ray projection image of the LP phantom. The phantom was mounted directly on the surface of detector to isolate the blurring effect due to any extended size of x-ray source (which is ~50 μm). By calculating the image contrast at different position of LP phantom, with the equation given by

$$I.C. = \frac{I_{\max} - I_{\min}}{I_{\max} + I_{\min}} \qquad (1)$$

where I.C. is image contrast, and I_{max} and I_{min} arethe image intensity values at the maximum and minimum respectively.

The MTF was developed as shown in Fig. 1-b. The MTF shows that the detector can achieve 140-μm (3.6 LP/mm) resolution at half maximum image contrast and a resolution of approximately one pixel (100 μm) for 20% maximum image contrast.

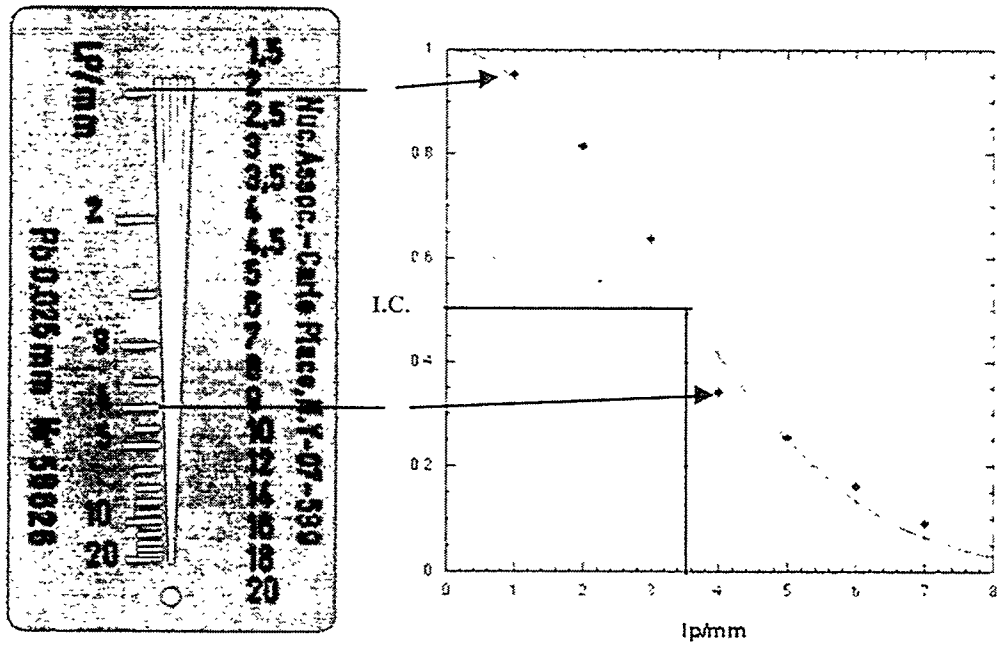

Fig. 1. Determination of spatial resolution using LP phantom. (a) Projection X-ray image of LP phantom when placed on detector (650x350 pixels^2). (b) 20-frame average line pair resolution.

To determine the resolution of a 3-D reconstructed image, a phantom sample made of monolithic Si_3N_4 was used, which has a diameter of 20.3 mm and 12.6-mm height. The phantom sample had 9 artificial holes, that is, three sets of three different diameters of 0.33, 0.66, and 0.508 mm. 720 projection images were taken within a full range of rotation, 360 degrees, at 120 kVp/ 0.4mA. Each projection has a size of 400 x 300 pixels^2, and the entire scan took about 1 hour. Figure 2-a represents a projection image of the sample while figure 2-b does a 2-D slice reconstruction at the level indicated by an arrow in Fig. 2-a. To evaluate the spatial resolution, a line profile was generated (see Fig. 3) across one of the holes in the CT image shown in Fig. 2-b. The 0.508-mm hole was selected. The point spread function (PSF) can been determined by differentiating the curve fit of the line profile. Finally, by applying Fourier transformation on the point spread function, as shown in Fig. 3, the MTF of the CT reconstruction image can be generated in frequency domain, which has the same concept of the MTF from the projection of the LP phantom. Here, 2 f/mm corresponds to one LP/mm. The resolution of the reconstructed image is compatible to that of the projection image, which is ~140 μm at half maximum contrast.

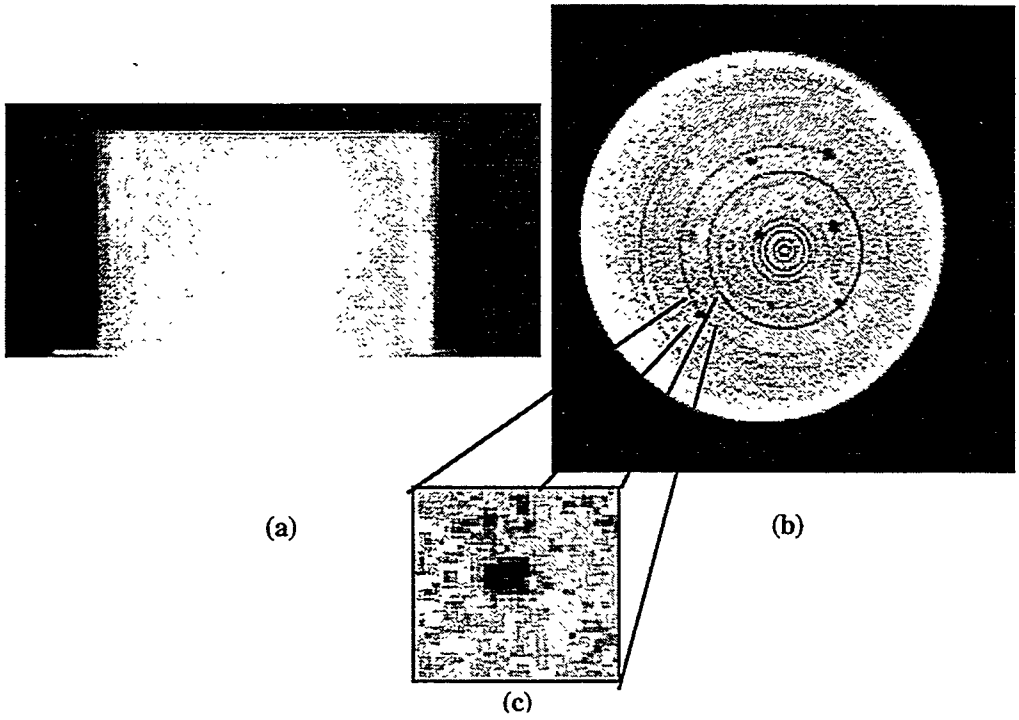

Fig. 2. X-ray images. (a) Projection X-ray image of silicon nitride (Si_3N_4) cylinder hole phantom. (b) CT reconstruction image of Si_3N_4 cylinder hole phantom (a). (c) Magnified image of part hole phantom. (b).

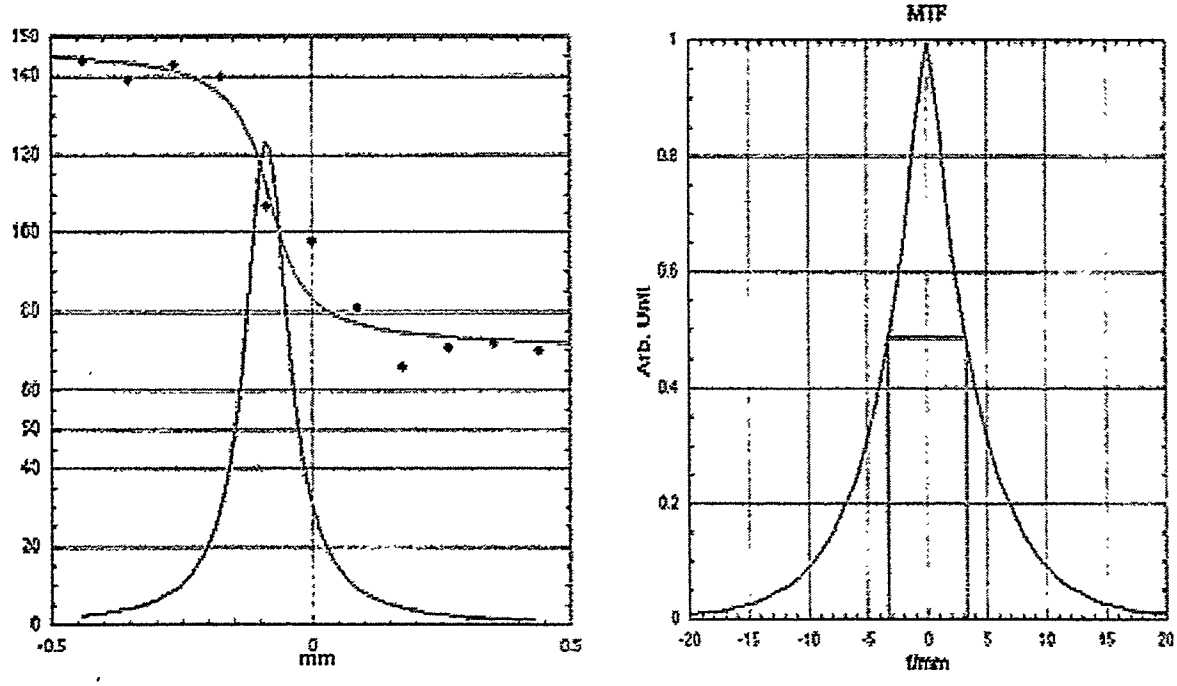

Fig. 3. Determination of MTF. (a) Line profile across 0.508-mm hole from image of Fig. 3-b. The point spread function appears as gaussian shape. (b) MTF derived from point spread function shown in (a).

A.2. XCT reconstruction of pre-sintered hot-gas filter

For a preliminary experiment to test the functionality of the XCT scanner with the MX-1024 detector, we used a pre-sintered hot-gas filter. Considering the limitation of our cone-beam reconstruction algorithm, which can be operable within a beam-diverging angle of < 6 degrees, we located the sample at ~ 80 cm from the X-ray source (the diameter of the sample is ~ 7 cm). For a CT scan, 360 projections, shown as Fig. 4, over 360° were taken at an X-ray setup of 120 kVp/ 0.4 mA. The acquisition time for the entire scan of 360 projections took a half hour and the imaging processing to interpolate bad pixels (previously mentioned in the late report) with neighboring-pixel values was done in ~2.5 hrs.

Figure 5 is one reconstruction image with ~100-μm resolution. The reconstruction time for one slice took ~1.5 min. At this time, we could not completely remove the beam-hardening effect. Because our X-125 X-ray source cannot generate X-ray photons at energies high enough to produce a high SNR at the sample position described above, we could not apply a filtering system to reduce beam hardening. The reconstruction could not provide information of density distribution, but can define internal defects with a resolution of ~100 μm.

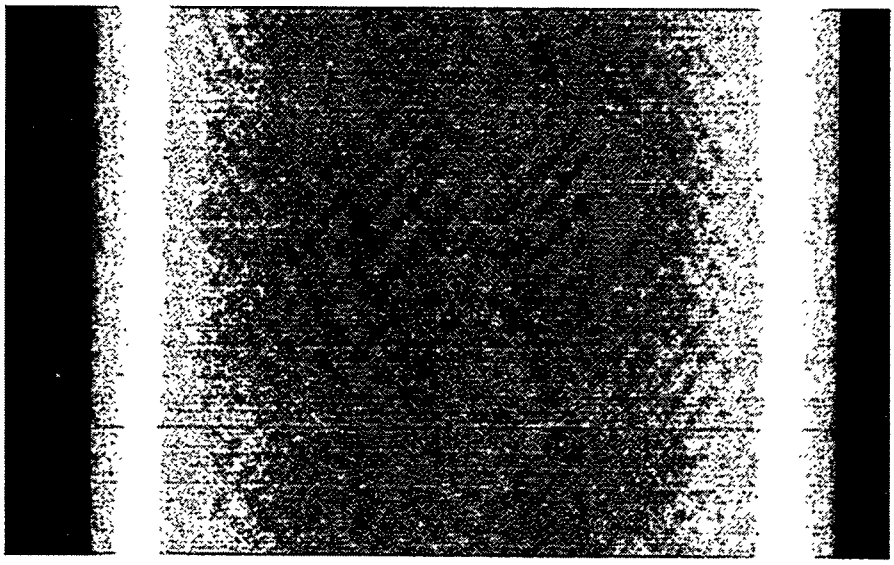

Fig. 4. Typical projection X-ray image of fiber pre-formed ceramic composite: image size is 800 x 500 pixels^2.

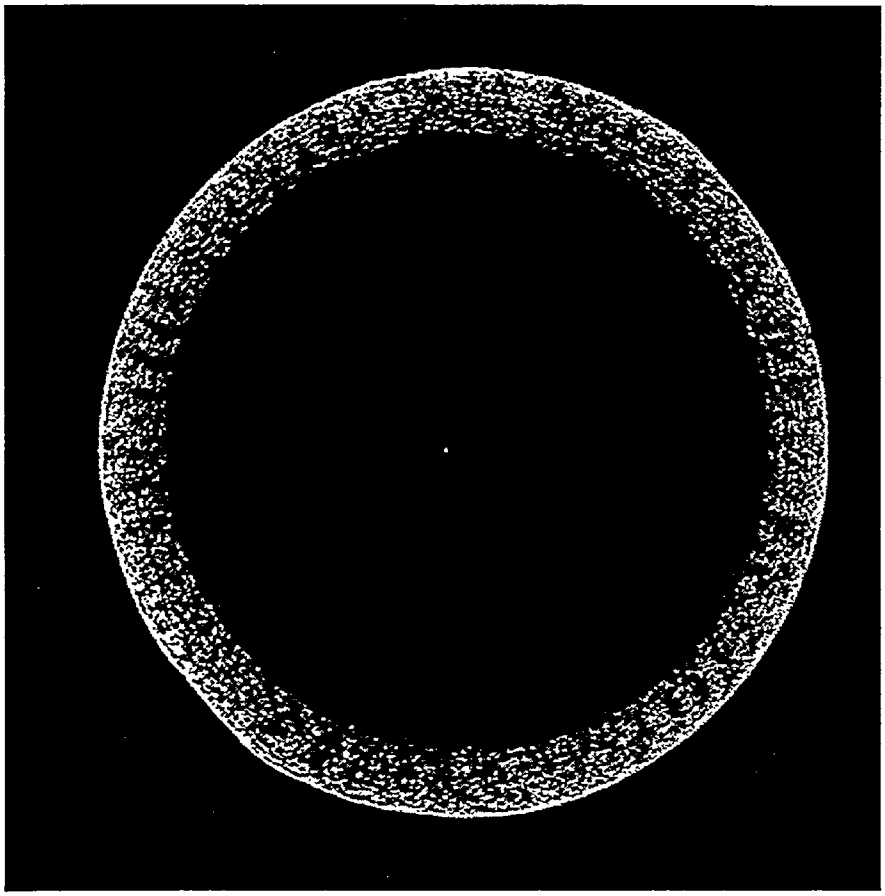

Fig. 5. X-ray image reconstruction of ceramic composite pre-formed tube: The size of the reconstructed image is 800 x 800 pixels^2 and each pixel represents the physical size of 100 x 100 μm^2.

B. NewRID-512 Detector (8" x 8")

B.1. Installation of PCI frame grabber

The new 8" x 8" detector RID 512-400 was delivered this period with a Heimann Electronics PCI frame grabber along with the corresponding software program HIS.EXE, implemented under WINDOW'95™ for continuous measurement tasks. Additional software modules are available in the CSL (Customer Software Library) to implement the detector in customers imaging software. The heart of the detector is a flat panel based on amorphous silicon (a-Si) technology forming a 204.8-mm^2, image-sensing photodiode array with 512 x 512 pixels. The resolution results in a pitch of 400 μm. This light-sensitive photodiode array is coupled to Lanex™ scintillator that responds to X-rays. The installation of the frame grabber with the software was completed, and the practical use of the software to operate the detector was verified. Figure 6 is an X-ray transmission image of a composite, boron plate, which was obtained by the new flat panel detector with an X-ray setup of 100 kVp/ 0.3 mA.

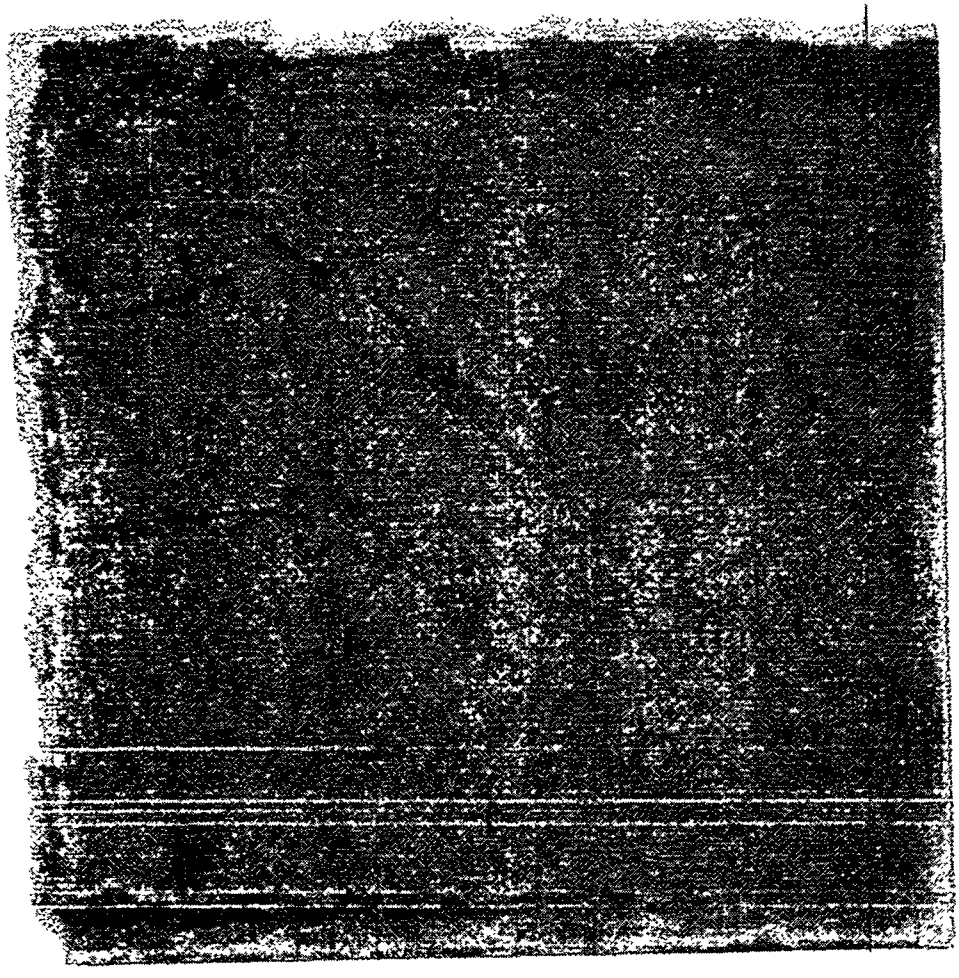

Fig. 6. X-ray transmission image of composite, boron plate, captured with the new 8" x 8" RID-512 amorphous silicon detector.

B.2. Development of interface code for CT operation

The main goal in utilizing the flat-panel detector is for CT applications. Because the CT-scan code was done in Labview, it is necessary to develop a Labview interface to synchronize data acquisition with CT-scanning motion. Because the RID-512 has a sensor array and an interlace sequence different from the MX-1024, it was necessary to modify our existing interface code by developing a new algorithm to deinterlace captured images. Figure 7 is an X-ray projection image captured by the new RID-512 detector driven with the newly developed interface code. An XCT system is now available for utilizing the 8" x 8" detector.

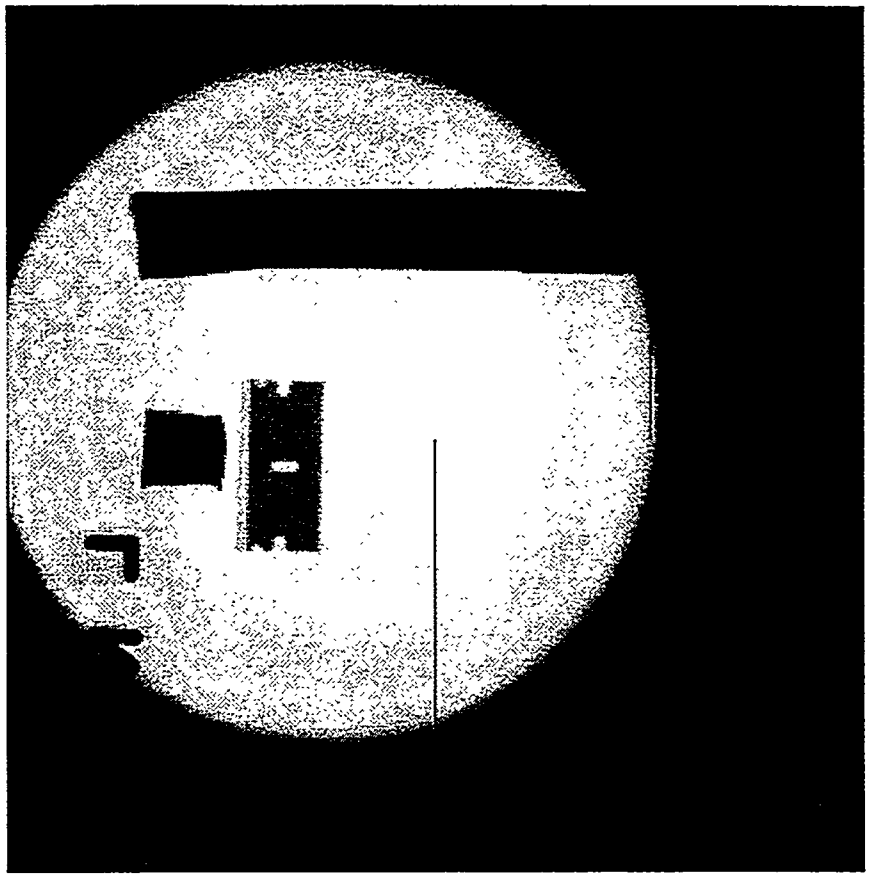

Fig. 7. Projection X-ray image obtained by Labview interface code using new 8" x 8" RID-512 α-Si detector.

B.3. X-ray Densitometry of Diesel Engine Valve Guides

We concluded the study on the chopped carbon fiber/Si_3N_4 diesel engine valve guides this period. Honeywell Ceramic Components provided the destructive data analysis for all test samples. These data, obtained at axial locations L/4, L/2, and 3L/4 were compared to the density data obtained nondestructively by 3D x-ray tomography. These data are combined and shown below in Table 1.

Table 1. Comparison between destructive and nondestructive density values for C/Si_3N_4

	A-S Lot No.	C97285	ANL Series 1		A-S Lot No.	C98116	ANL Series 2
Sample ID	ANL (g/cc)	A-S (g/cc)	Difference	Sample ID	ANL (g/cc)	A-S (g/cc)	Difference
1-2-7.5-1/4	2.34	1.744	0.60	2-1-7.5-1/4	2.53	1.724	0.81
-1/2	2.35	1.720	0.63	-1/2	2.53	1.734	0.80
-3/4	2.33	1.691	0.64	-3/4	2.47	1.714	0.76
1-2-10.0-1/4	2.28	1.687	0.59	2-1-10.0-1/4	2.49	1.702	0.79
-1/2	2.30	1.696	0.60	-1/2	2.49	1.697	0.79
-3/4	2.29	1.691	0.60	-3/4	2.47	1.690	0.78
1-2-12.5-1/4	2.22	1.675	0.55	2-1-12.5-1/4	2.42	1.678	0.74
-1/2	2.23	1.670	0.56	-1/2	2.41	1.683	0.73
-3/4	2.22	1.685	0.54	-3/4	2.42	1.689	0.73
1-3-7.5-1/4	2.35	1.720	0.63	2-2-7.5-1/4	2.54	1.720	0.82
-1/2	2.35	1.719	0.63	-1/2	2.54	1.735	0.81
-3/4	2.30	1.715	0.59	-3/4	2.54	1.672	0.87
1-3-10.0-1/4	2.29	1.680	0.61	2-2-10.0-1/4	2.52	1.737	0.78
-1/2	2.29	1.691	0.60	-1/2	2.54	1.731	0.81
-3/4	2.26	1.679	0.58	-3/4	2.53	1.738	0.79
1-3-12.5-1/4	2.26	1.683	0.58	2-2-12.5-1/4	2.41	1.685	0.73
-1/2	2.20	1.680	0.52	-1/2	2.40	1.681	0.72
-3/4	2.22	1.680	0.54	-3/4	2.38	1.664	0.72
	Average	Difference	0.063		Average	Difference	0.085

Note: Sample ID Legend: Lot No.- Mix No.- % fiber- section, e.g., 1-2-7.5-1/4

The correlations can be better observed by looking at the data plotted together. These are shown in Figs. 8-11, which are for the 2 different mixes. Figures 8 and 9 show that the ANL nondestructive data clearly defines differences in density between 7.5%, 10.0% and 12.5 Vol. % chopped carbon fiber differences (better than the destructive analysis).

Figures 10 and 11 are for Series 2 mixes. In these correlations, there is less variation between 7.5, 10.0 and 12.5 vol. % chopped carbon fiber as determined either destructively or nondestructively. We will look at these a little more carefully but except for a constant, .59 for Series 1 and .78 for Series 2, the destructive and nondestructive data correlate well.

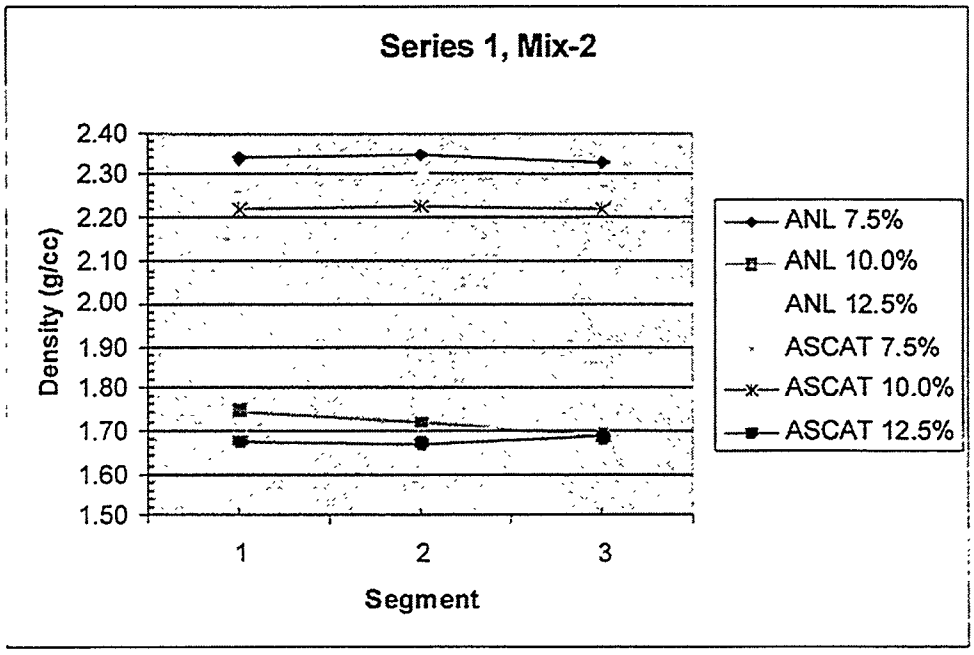

Fig. 8. Correlation of destructive measured density and nondestructive measured density for Series 1, Mix 2.

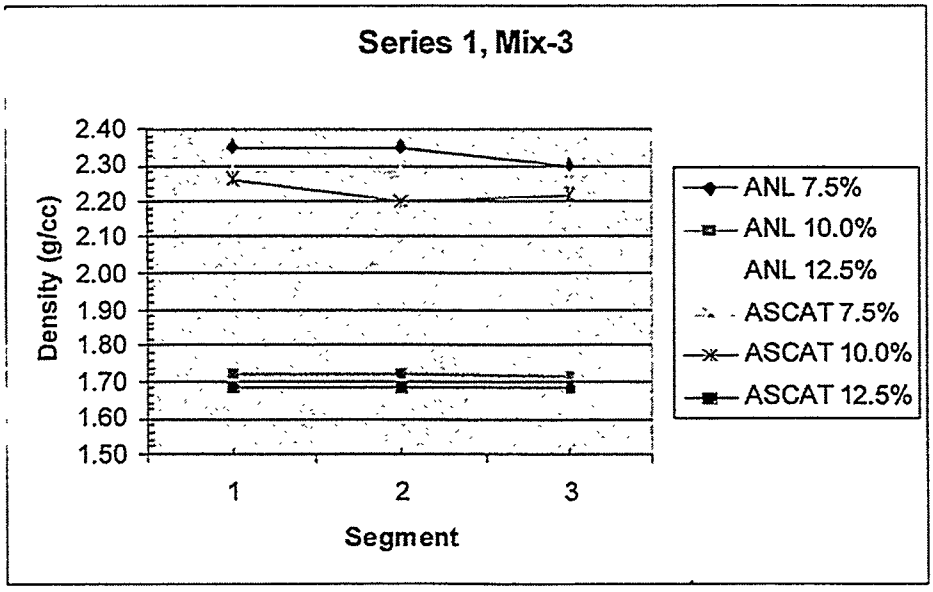

Fig. 9. Correlation of destructive measured density and nondestructive measured density for Series 1, Mix 3.

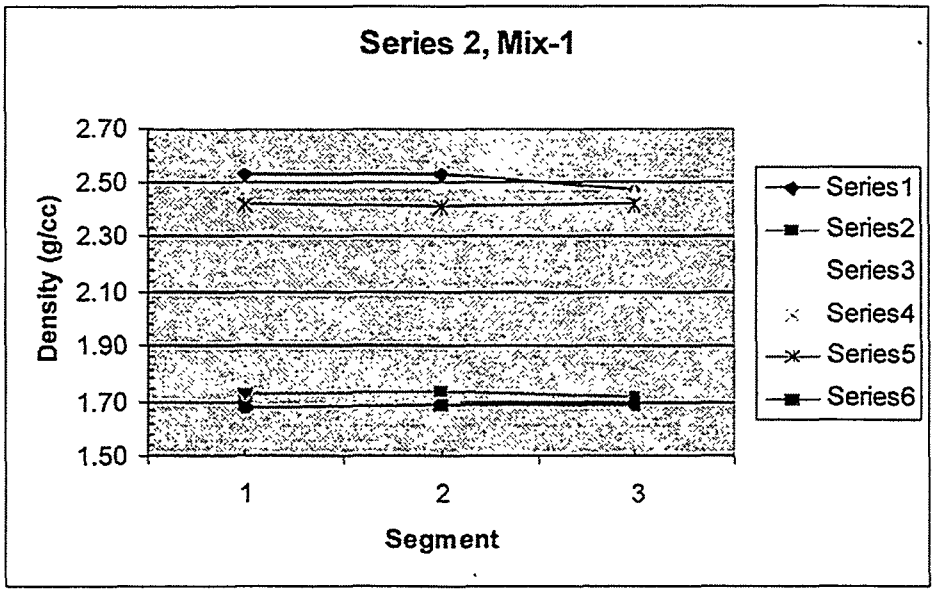

Fig. 10. Correlation of destructive measured density and nondestructive measured density for Series 2, Mix 1.

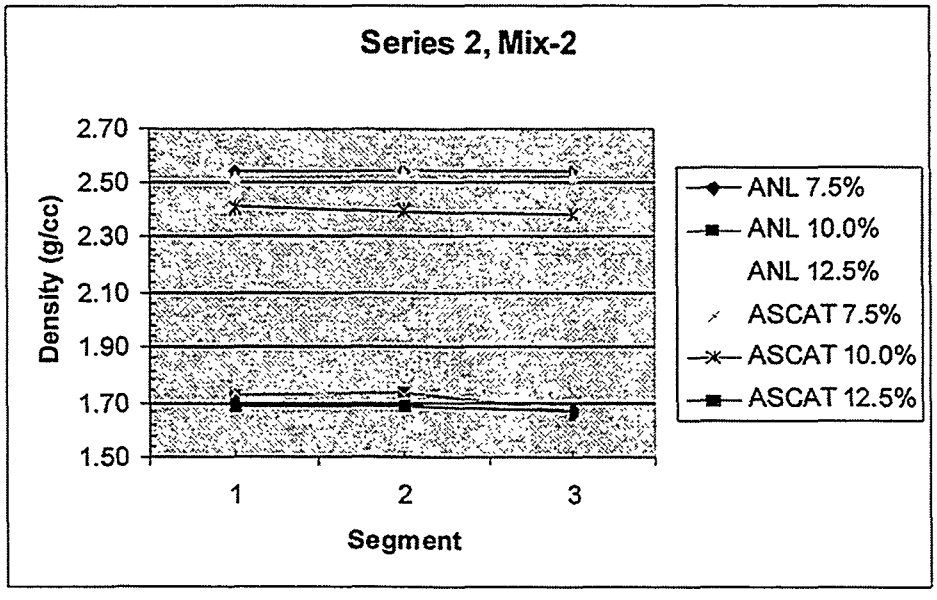

Fig. 11. Correlation of destructive measure density and nondestructive measure density for Series 2, Mix 2.

3. Diesel Fuel Injector Nozzles

This period we conducted additional studies of the metallic fuel injector nozzles we already have on hand and in addition we extended the industrial interaction through discussions with Cummins Engine in Columbus, Indiana. Again, it is clear that fuel delivery systems are important.

Publications:

- H.-R. Lee and W. Ellingson, "Development of Metrological NDE methods for Ceramic Components for Microturbines," submitted to the 45th ASME Gas Turbine and Aeroengine Technical Congress Exposition and Users Symposium, sponsored by ASME, Munich, Germany, May 9-11, 2000
- H.-R. Lee and W. Ellingson, "Comparison of flat-panel amorphous-silicon and image-intensifier/CCD detectors for X-ray tomographic imaging," submitted to Review of Scientific Instruments, October 1999.
- H.-R. Lee and W. Ellingson, "Characterization of a flat panel, amorphous silicon detector as an imaging device for computed tomography," submitted to Journal of X-ray Science and Technology, May 1999.

TESTING AND EVALUATION OF ADVANCED CERAMICS AT HIGH TEMPERATURE

J. Sankar, A. D. Kelkar, S. Yarmolenko, W. Windley III, and Q.Wei (Department of Mechanical Engineering, North Carolina A & T State University, Greensboro, NC 27406).

Objective/Scope

The objective of this research is to test and evaluate the long-term mechanical reliability of a Si_3N_4 at temperatures up to 1300°C.

The required research includes four (4) major tasks:

Task 1. Four (4) Point Flexural Test

Four (4) point flexural tests shall be performed for Allied Signal's GS44 silicon nitride at lower temperatures to investigate 500° -1100° C characteristics of the material at this temperature range.

Task 2. Cyclic Flexural Fatigue Testing of GS44

Cyclic flexural fatigue of GS44 silicon nitride shall be performed at room and elevated temperatures.

Task 3. Stress - Rupture Study of GS44

Stress-rupture study of GS44 silicon nitride will be performed at various temperatures and stresses.

Task 4. Microscopy

High-resolution microscopy and fractography work are a part of all tasks shown above.

Technical Highlights

During reporting period four point bend and flexural fatigue tests of sintered Si_3N_4 were completed at room and elevated temperatures. Extensive transmission electron microscopy (TEM) has been carried out to study the microstructural evolution of in situ self-reinforced silicon nitride.

Introduction

GS 44 was designed for applications where the temperature is not more than 1100°C. A number of investigations on the room temperature behavior such as fracture toughness, R-curve behavior, etc. have been reported, literature survey shows that studies on the microstructure and mechanical behavior of this material is quite limited. We have reported earlier that the stress exponent of this material increased from unity at temperatures below 1100° C to 2.0 at temperatures above 1100°C. To understand the underlying mechanism of this change, we studied the microstructural changes during high temperature creep of this material. The following is what we have observed.

In the studies of influence of heat treatment on creep behavior of GS44 sintered silicon nitride Liu et al. [1] have conducted various post-fabrication heat treatment on the material, including furnace annealing and microwave annealing at 1200°C. It was shown that microwave annealing at 1200°C could significantly enhance the creep resistance of this material. Furnace annealing at 1200°C for 100 hours was also somewhat effective in lowering creep rate and resulted in longer creep life compared to that of unannealed material, but was far less effective than microwave annealing at 1200°C.

In order to understand the behavior of the materials, we first studied the fractography of several samples. The samples include as sintered, furnace annealed and microwave annealed. From scanning electron microscopy, we found that the fracture surface of as sintered GS44 exhibits a large volume of cavities and also the size of cavities were relatively large. Also observed in these samples were large size flaws, which might have been the damage initiation. On the other hand, the volume and size of the cavities in the microwave-annealed samples were much less. The furnace-annealed samples showed fracture surface features between the as sintered and the microwave annealed. It is therefore presumed that the effect of annealing is in essence to change the grain boundary structure and multiple junction structure. Annealing may have also healed the bulk flaws in the material. Detailed information about this presumption will be available upon TEM studies.

Experimental Data

Four (4) Point Flexural Tests

The American Society for Testing and Materials (ASTM C 1161-94) Standard Test Method for Flexural Strength of Advanced Ceramics at Ambient Temperature and (ASTM C 1211-92) Standard Test Method for Flexural Strength of Advanced Ceramics at Elevated Temperatures were followed as a guide for testing. The experiments were performed with 21 specimens using displacement control at a rate of 0.5 mm/min. All flexural tests were performed using ATS 1605 Series Testing Machine with Series 4231 High Temperature Bend Testing LVDT Extensometer and furnace (up to 1600°C).

Four (4) Point Flexural Fatigue Tests

Fatigue tests have been performed under displacement control at rate 10mm/min. Cyclic loading frequency depends on loading amplitude (0.35 Hz for maximum load

700 N or 0.5 Hz for 500 N). Data acquisition system collected displacement data with threshold level 5 N (cyclic loading amplitude accuracy not more than 1%). We designed software, which can analyze up to 20 Mbytes data files to perform extraction data, visualization and calculations for each cycle. Tests have been conducted at room temperature and at 1000°C. The fatigue samples were etched for two minutes with molten sodium hydroxide at 300°C. The grain structure after fatigue tests at room and elevated temperatures has been studied using the scanning electron microscopy (SEM). Micrographs have been collected using variable pressure scanning electron microscope Hitachi S-3000N.

Results and Discussion

Creep

Figure1 shows the creep fracture surface of as sintered GS44. A large size flaw can be seen from this micrograph. Figure 2 shows a large amount of cavities. All the cavities are located at the multiple junctions.

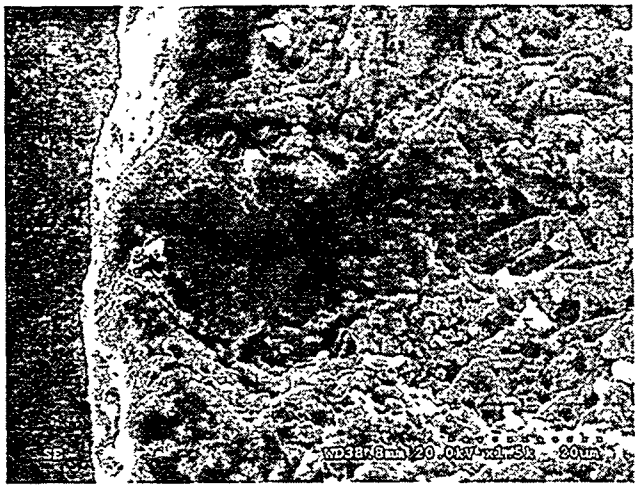

Fig. 1 SEM micrograph of the fracture surface of as sintered GS44, showing a large size bulk flaw.

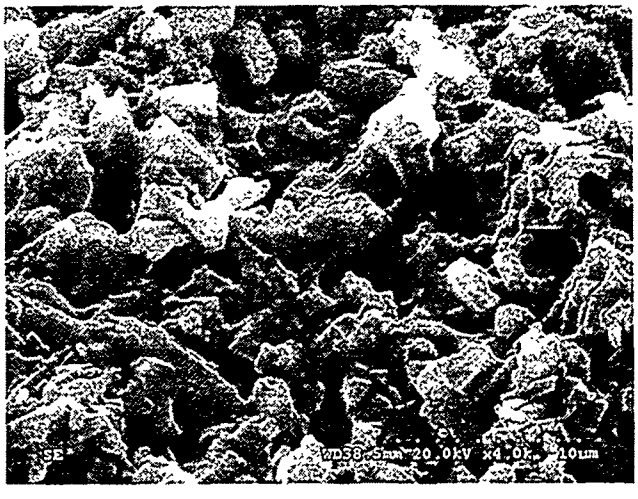

Fig.2 SEM micrograph of the fracture surface of as sintered GS44, showing a large volume of large size cavities located on the multiple junctions.

Figure 3 is the SEM micrograph of the creep fracture surface of GS44 microwave annealed at 1200°C. The amount of cavities in this sample is much less as compared to that of Figure 2. Figure 4 is the fracture surface of another microwave annealed sample.

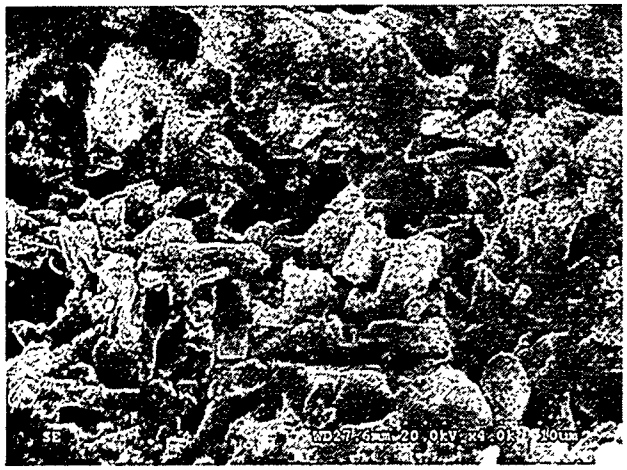

Fig. 3 Creep fracture surface of a microwave annealed GS44.

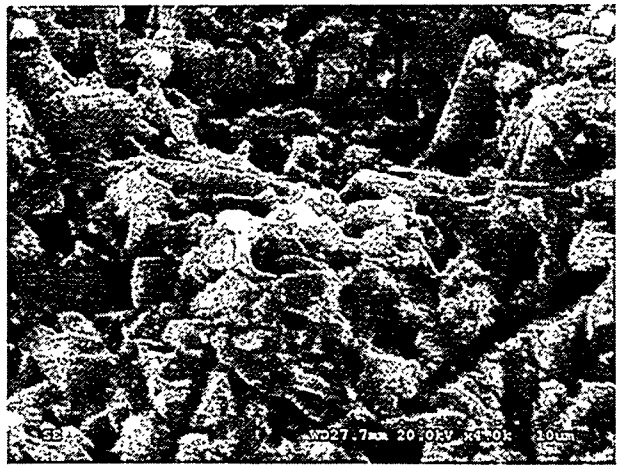

Fig. 4 Creep fracture surface of a microwave annealed GS44.

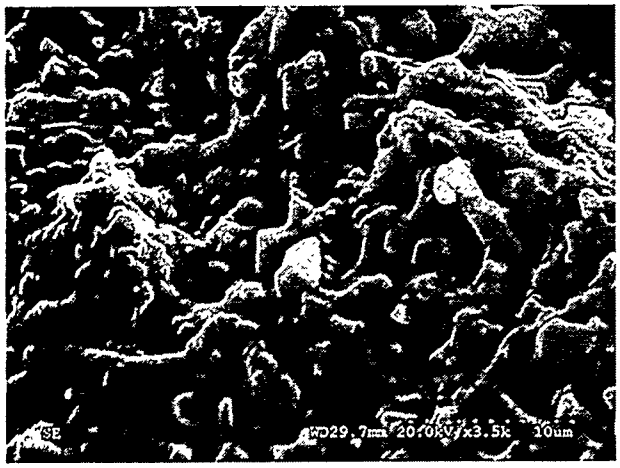

Figure 5 is the SEM micrograph of the creep fracture surface of GS44 furnace annealed at 1200°C. The features in this sample are somewhat between those of as sintered and microwave annealed. It should be noted that more convincing conclusion should be drawn when the detailed TEM studies are available. This will be completed in the next reporting period.

Flexural Tests at room and elevated temperatures

Figure 6 shows changes of failure load vs. temperature. Flexural strength depends on temperature as monotonic function with scattering less than 10%, which can be used to predict failure properties of the GS44 under bend test conditions. Flexural strength at 1000°C less than the room temperature value in 1.6 times (60% of room temperature value). Increasing test temperature on another 200°C (up to 1200°C) leads to 1.5 times less flexural strength at 1200°C compare to 1000°C. It shows that flexural strength of GS44 drops dramatically at temperatures higher than 800 - 1000°C. This results correspond to creep analysis reported earlier which shown that the stress exponent of GS44 increases from unity at temperature below 1100°C to 2.0 at temperature above 1100°C.

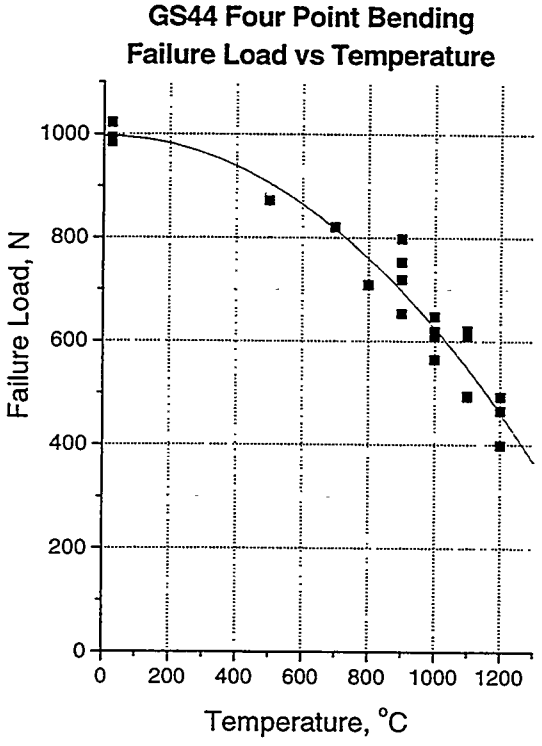

Fig. 6. Failure Load vs Temperature

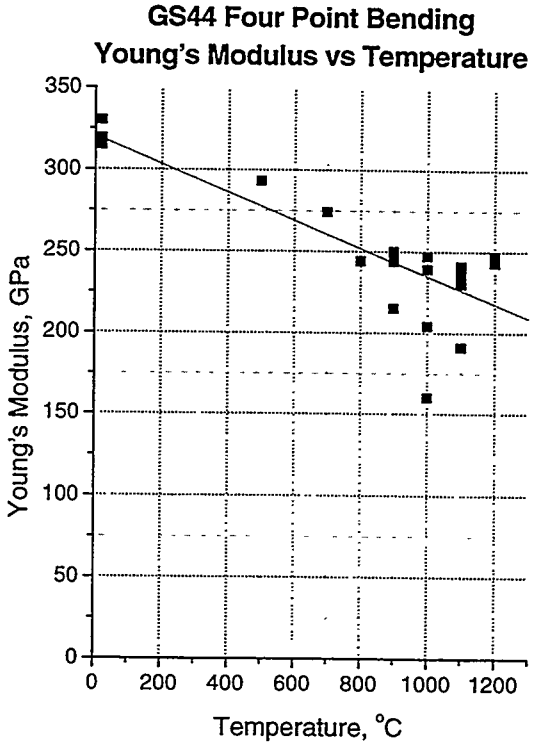

Fig. 7. Young's Modulus vs Temperature

Figure 7 shows changes of Young's Modulus with temperature. This dependence seems to be linear with significant scattering at temperatures more than 900°C.

Flexural Fatigue

The specimens were tested at room temperature and 1000°C. The room temperature specimen was fatigued using 70 % of the ultimate load (~1000 N) and the 1000°C specimen at 80 % ultimate load (~500 N). After 4000 cycles the modulus of the room temperature specimen dropped only about 1 % (70% ULT) and 3% (80% ULT). At elevated temperature specimen lost 10 % of its modulus after 4000 cycles (Table 1). Figure 8 shows Young's Modulus changes during fist 4000 cycles in four-point bending fatigue test at room temperature. Figure 9 shows changes of modulus for 1000°C for the first 4000 cycles.

Table 1. Flexure Fatigue Test Results for GS44 at room and 1000°C.

% ULT	Temp (°C)	Initial Modulus (GPa)	Final Modulus (GPa)	% Drop in Modulus	Total Cycles	Failure (yes/no)
70	20	302.3	298.4	1.29	16000	No
80	20	332.9	322.2	3.21	3000	No
80	1000	282.2	253.6	10.13	4000	No
80	1000	260.9	244.4	6.32	4000	No

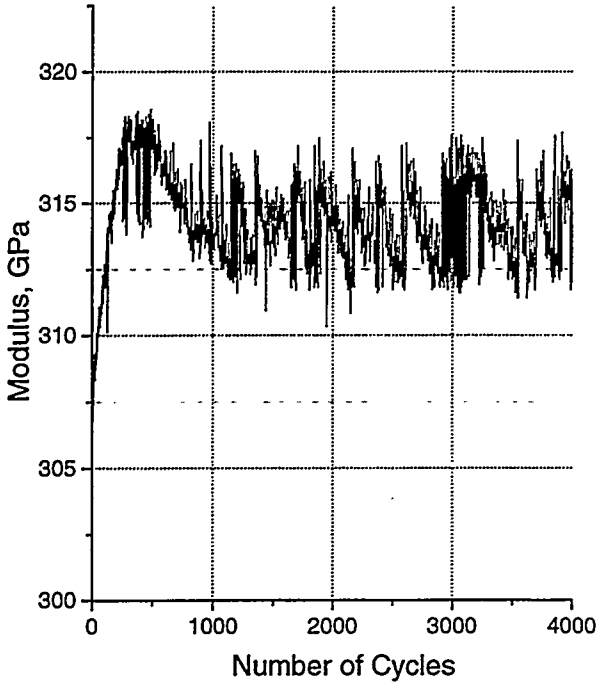

Fig. 8. GS44 Fatigue Four Point Bending Test (70% ULT at Room Temperature): Young's Modulus vs Number of Cycles

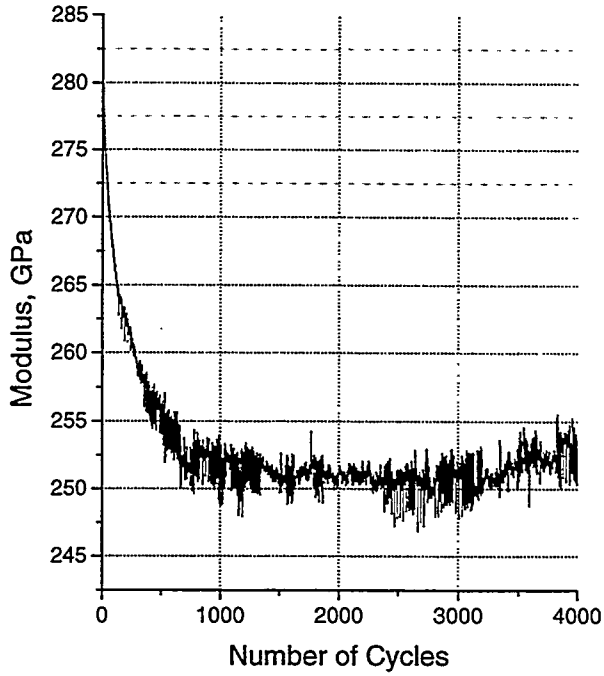

Figure 9. GS44 Fatigue Four Point Bending Test (80% ULT at 1000°C): Young's Modulus vs Number of Cycles

Figure 10 shows the grain structure of silicon nitride in GS44 (polished and etched sample, SEM). Grain sizes vary from 1 to 10 μm with aspect ratio of 3-4. Observed grain size depends on etching condition significantly, which does not allow performing accurate comparative grain size analysis for soaked and fresh samples.
Figure 11 shows a crack that was initiated from surface flow during fatigue testing.

Figure 10. Gs-44 Silicon Nitride Fatigue Test at 1000°C Sample Etched for 2 Minutes with Molten NaOH

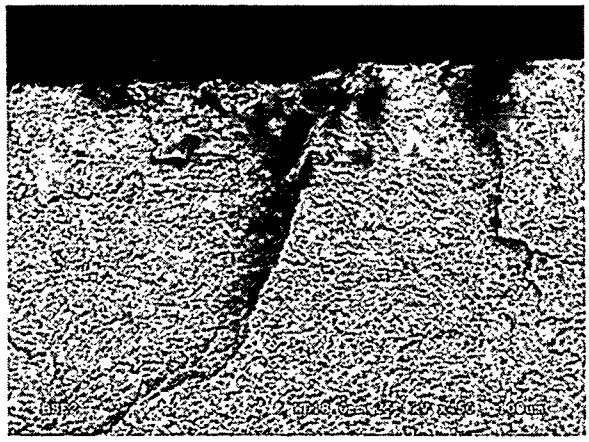

Figure 11. GS-44 Surface Crack from Fatigue Sample

Status of Milestones

On Schedule

Communications/Visitors/Travel

Communicated with Dr. Tom Yonushonis of Cummins Engine Co. related to Zirconia materials

J. Sankar attended Heavy Vehicle Propulsion Materials workshop, Aug. 19-20th at Knoxville, TN

Problems Encountered

None

Status of Milestones

On Schedule

Publications

1. Q. Wei, J. Sankar, A. D. Kelkar, and J. Narayan, "Microstructure Evolution Accompanying High Temperature Uniaxial Tensile Creep of Self-Reinforced Silicon Nitride Ceramics," Materials Science and Engineering Journal A, A272, 380-388, 1999
2. L. Russell, J. Sankar, R. Windley, J. Lua, "FEM Response Analysis of GS-44 Specimen Under Four-Point Bending" Sixth International Conference on Composites Engineering, June 27-July 3, 1999, Orlando, Florida, pp. 885-886.
3. Q. Wei, J. Sankar, J. Narayan, "Role of Dislocations in High Temperature Creep of in situ reinforced Silicon Nitride" Sixth International Conference on Composites Engineering, June 27-July 3, 1999, Orlando, Florida, pp. 721-722.
4. L. Russell, J. Sankar, Q. Wei, "The Effects of Thermal Soaking on the Performance of Si_3N_4 Slurry Coated Substrates" Sixth International Conference on Composites Engineering, June 27-July 3, 1999, Orlando, Florida, pp. 711-712.
5. J. Lua, L. Russell, J. Sankar, "Processing Induced Thermal Residual Stress in Thermal Barrier Coated Substrates" Sixth International Conference on Composites Engineering, June 27-July 3, 1999, Orlando, Florida, pp. 515-516.
6. R. Windley and J. Sankar, "Finite Element Analysis of Sintered Silicon Nitride Specimens Under Four-Point Bending" presented in 24th Annual Cocoa Beach Conference and Exposition, Jan. 23-28, 2000, Cocoa Beach, Fl. (under preparation for peer publication).

7. Q. Wei, J. Sankar, J. Narayan, K. Liu, "Microstructure and Creep Behavior of Self-reinforced Silicon Nitride Ceramics Heat-Treated by Furnace and Microwave Annealing", Accepted at the 24th Annual Cocoa Beach Conference, Paper #2000-1603, Cocoa Beach, FL, Jan. 23-38, 2000 (Paper under preparation).
8. Q. Wei, K.C. Liu, J. Sankar, "Effect of Heat-Treatment on Creep Behavior of Self-Reinforced Silicon Nitride", Accepted at the 24th Annual Cocoa Beach Conference, Cocoa Beach, FL, Jan. 23-38, 2000 (Paper under preparation).

References

[1] K.C.Liu, C.O.Stevens, C.R.Brinkman, J.O.Kiggens, T.N. Tiegs, "Influence of Heat Treatment on Creep Behavior of a Scintered Si_3N_4 Ceramics", Ceram. Eng. & Sci. Proc., 17(3) 401-410 (1996).

Life Prediction of Ceramic Diesel Engine Components

A. A. Wereszczak (ORNL), T. P. Kirkland (ORNL), H. - T. Lin (ORNL), R. Tandon (Caterpillar), S. K. Lee (Adecco TAD Technical), and M. J. Andrews (ORNL)

Objective/Scope

The valid prediction of mechanical reliability and service life is a prerequisite for the successful implementation of structural ceramics as internal combustion engine components. There are three primary goals of this research project which contribute toward that implementation: the generation of mechanical engineering data from ambient to high temperatures of candidate structural ceramics; the microstructural characterization of failure phenomena in these ceramics and components fabricated from them; and the application and verification of probabilistic life prediction methods using diesel engine components as test cases. For all three stages, results are provided to both the material suppliers and component end-users.

The systematic study of candidate structural ceramics (primarily silicon nitride) for internal combustion engine components is undertaken as a function of temperature (< 900°C), environment, time, and machining conditions. Properties such as strength and fatigue will be characterized via flexure and rotary bend testing.

The second goal of the program is to characterize the evolution and role of damage mechanisms, and changes in microstructure linked to the ceramic's mechanical performance, at representative engine component service conditions. These will be examined using several analytical techniques including optical and scanning electron microscopy. Specifically, several microstructural aspects of failure will be characterized:

(1) strength-limiting flaw-type identification;
(2) edge, surface, and volume effects on strength and fatigue size-scaling
(3) changes in failure mechanism as a function of temperature;
(4) the nature of slow crack growth; and
(5) what role residual stresses may have in these processes.

Lastly, numerical probabilistic models (*i.e.*, life prediction codes) will be used in conjunction with the generated strength and fatigue data to predict the failure probability and reliability of complex-shaped components subjected to mechanical loading, such as a silicon nitride diesel engine valve. The predicted results will then be compared to actual component performance measured experimentally or from field service data. As a consequence of these efforts, the data generated in this program will not only provide a critically needed base for component utilization in internal combustion engines, but will also facilitate the maturation of candidate ceramic materials and a design algorithm for ceramic components subjected to mechanical loading in general.

Technical Progress

The description of the technical progress for the present semiannual reporting period is provided in two sections: the completion of the NT551 silicon nitride analysis, and the current research efforts on the Caterpillar project.

NT551 Silicon Nitride Analysis

Microstructural and chemical characterizations of the NT551 silicon nitride and detailed examinations of the "porous region" defect were completed. Elemental mapping, in concert with back-scatter scanning electron microscopy (BS-SEM) imaging, provided new evidence that the grain boundaries within the macroscopic "snowflakes" in the NT551 were comprised of two different silicate phases: a phase containing Y, Al, Nd, and N, and a second phase containing essentially only Si and O. Early in this study, polished cross-sections examined with secondary electron SEM (SE-SEM) imaging revealed the appearance of relatively high concentrations of pores

in these "snowflakes" [1]. However, BS-SEM imaging showed the presence of a relatively dark (*i.e.*, species with relatively low atomic weight) phase coincident with what were thought of as pores. Elemental mapping of these dark regions showed the presence of only Si and O. In the surrounding grain boundaries, the elemental mapping showed that they contained Y, Al, Nd, N, Si, and O. The phase containing the Si and O appeared to be preferentially polished (compared to the Y-Al-Nd-Ni silicate phase) or pulled out when cross-sections were metallographically prepared resulting in the appearance of pores in SE-SEM. Although "snowflakes" were often observed on machined NT551 surfaces and bend bar fracture surfaces, "porous regions" like those on polished NT551 cross-sections were never located (although sought). It is not known if the presence of these two phases were a result differing crystallization kinetics or phase separation; however, their concurrent presence accounted for the macroscopic "snowflake" that was visible to the naked eye in the NT551. This type of inhomogeneity is still a volume-type-flaw, so this new information will not affect the censored Weibull distributions in past analyses because the previously designated "porous region" was also a volume-type-flaw.

M. J. Andrews successfully completed the oral defense portion of his Ph.D. at New Mexico State University, Las Cruces, NM, on September 15. The dissertation addressed the mechanical testing, fractography, and valve life prediction involving NT551 silicon nitride. Mark's thesis will be reformatted and published as a DOE/ORNL Technical Report by the end of this calendar year.

Caterpillar Test Program

The flexure test matrix under examination is shown in Table 1. The test matrix for the AS800, GS44, N7202, KYON3000 is now completed and the strength data and Weibull statistics have been supplied to Caterpillar and to the respective silicon nitride manufacturers for their examination. Microstructures of the AS800, GS44, N7202, KYON3000, and KYON3500 silicon nitrides are shown in Fig. 1. Their respective uncensored flexure strength distributions for transversely machined bend bars are shown in Figs. 2-6.

The strength results from the testing of the AS800, GS44, KYON3000, KYON3500, and N7202 silicon nitrides show that their 850°C strengths are lower than their 20°C strengths, and that they are relatively susceptible to slow crack growth or fatigue at 850°C. A common denominator among these five silicon nitrides is that they all contain a relatively high amount of sintering aid (compared to past-studied hot-isostatically-pressed, or HIPed, silicon nitrides). To examine the significance of this parameter on strength and fatigue at 850°C, flexure testing of NT154 silicon nitride is introduced into the matrix for only longitudinally machined sets. The strength of this material is very well documented above 980°C [2], but strength and dynamic fatigue data in the operating-temperature-range of the diesel engine ($\approx$ 850°C) has not been found. NT154 bend bars were machined from tensile specimen shanks that were tested as part of Reference 2. NT154 is a HIPed silicon nitride and contains a relatively low amount of sintering aid. Its strength results should provide some insight into what effect (if any) that the amount of sintering aid has on strength and fatigue at 850°C.

Fractography and strength-limiting flaw identification of the tested bend bars is underway. Initial results show that strength-limiting flaws in AS800, GS44, and N7202 are different at 850°C and 0.003 MPa/s than they were at 850°C and 30 MPa/s. The decrease in strength that these materials exhibited at 850°C and 0.003 MPa/s appears to be a consequence of this change in failure mechanism. Flexure strength tests involving GS44 in nitrogen, oxygen, and moist air are planned to study the strength-reduction phenomenon further. ORNL's H. -T. Lin has joined this effort and will be providing characterization assistance to the understanding of these failure mechanism changes.

Supplemental testing and microstructural characterizations of the silicon nitrides continued during the present reporting period. The thermal conductivity and thermal expansion measurements of AS800, GS44, N7202, KYON3000, and KYON3500 were completed as a function of temperature to 900°C. Their results were provided to Caterpillar and to their respective manufacturers. Microstructural and phase identification studies are under examination as well.

The utility and applicability of a new, accelerated, cyclic-fatigue-tester is under examination. A rotating beam fatigue tester is being overhauled so that a monotonically increasing load may be applied to the specimen during its rotation. A computer system was being interfaced with the unit to control the test and to measure cycles. The idea motivating this is analogous to what dynamic fatigue analysis does for static fatigue testing of monolithic ceramics; however in this case, the stress amplitude during cyclic testing is gradually increased. Tests are planned with AD995 alumina in both "dynamic-cyclic" fatigue testing as well as the more conventional cyclic ("static-cyclic") fatigue testing. AD995 alumina was chosen as the model material for the examination of this technique because its strength and fatigue are fairly well documented in the literature and the expense to procure and machine a statistically significant number of specimens was moderate. Specimens have been commercially machined and have been received. If the dominant fatigue mechanisms are the same in both types of cyclic tests, then mathematical formulations may be introduced to account for the monotonically increasing stress amplitude and then coupled with existing stress-amplitude-cycles-to-failure models. In such a circumstance, test durations for cyclic tests will be reduced because potentially long-duration "run-out" tests at low stress amplitudes will not occur.

Status of Milestones

All milestones are on schedule.

Communications / Visitors / Travel

- Billets of AS800 and GS44 were sent to Caterpillar's Raj Tandon for supplemental characterization.
- Elemental mapping results were communicated to SGNIC's V. Pujari.
- A. A. Wereszczak attended Mark Andrew's Ph.D. defense, New Mexico State University, Las Cruces, NM.

Problems Encountered

None.

Publications

An abstract was submitted for presentation/proceedings-paper-inclusion for the 24th Annual Cocoa Beach Conference and Exposition, January 23-28, 2000, Cocoa Beach, FL. Its title was "High Temperature Inert Strength and Dynamic Fatigue of Candidate Silicon Nitrides for Diesel Exhaust Valves" by A. A. Wereszczak, T. P. Kirkland, R. Tandon, and S. K. Lee.

References

[1] A. A. Wereszczak, M. J. Andrews, M. K. Ferber, and T. P. Kirkland, "Life Prediction Verification," *Heavy Vehicle Propulsion System Materials Program Semiannual Technical Progress Report to DOE Office of Transportation Technologies*, Apr. 1997 - Sep. 1997.

[2] J. C. Cuccio, P. Brehm, H. T. Fang, J. Hartman, W. Meade, M. N. Menon, A. Peralta, J. Z. Song, T. Strangman, J. Wade, J. Wimmer, and D. C. Wu, *Life Prediction Methodology for Ceramic Components of Advanced Heat Engines, Phase 1*, DOE Report ORNL/Sub/89-SC674/1/V2, 1995.

Table 1. Silicon nitride test matrix to compare inert strength, high temperature fatigue performance, and effect of machining orientation. A minimum of twenty-five ASTM C1161B specimens are being 4-pt flexure strength tested per condition.

Test Condition	AS800	GS44	KYON 3000	KYON 3500	N7202	NT154
20°C 30 MPa/s Longitudinal	Completed	Completed	Completed	X	Completed	X
20°C 30 MPa/s Transverse	Completed	Completed	Completed	X	Completed	
850°C 30 MPa/s Longitudinal	Completed	Completed	Completed	X	Completed	X
850°C 30 MPa/s Transverse	Completed	Completed	Completed	Completed	Completed	
850°C 0.003 MPa/s Longitudinal	Completed	Completed	Completed	Completed	Completed	X
850°C 0.003 MPa/s Transverse	Completed	Completed	Completed	Completed	Completed	
Material's Manufacturer	AlliedSignal Ceramic Components	AlliedSignal Ceramic Components	Kennametal	Kennametal	CFI	Norton

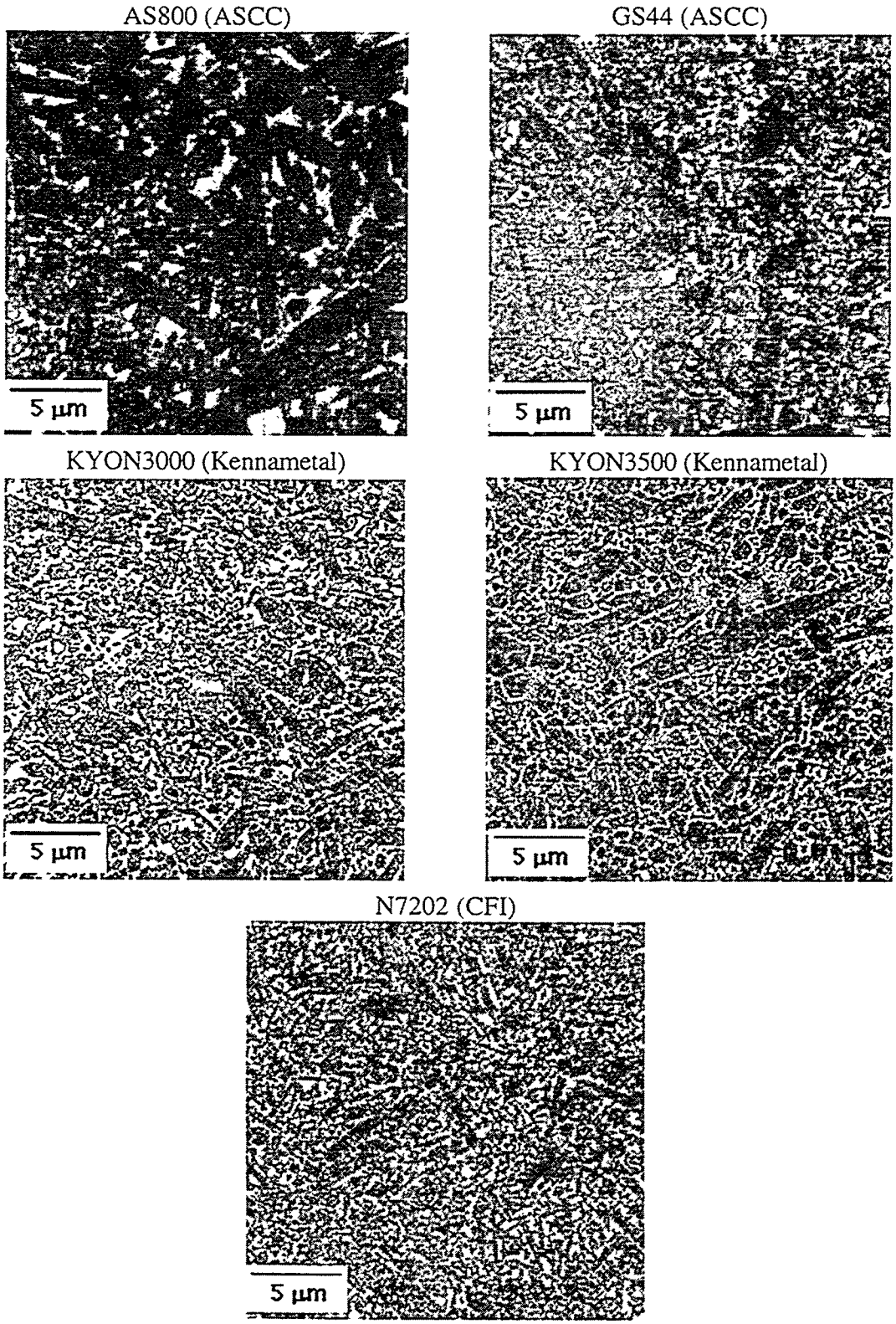

Figure 1. Silicon nitride microstructures of polished, plasma-etched cross-sections.

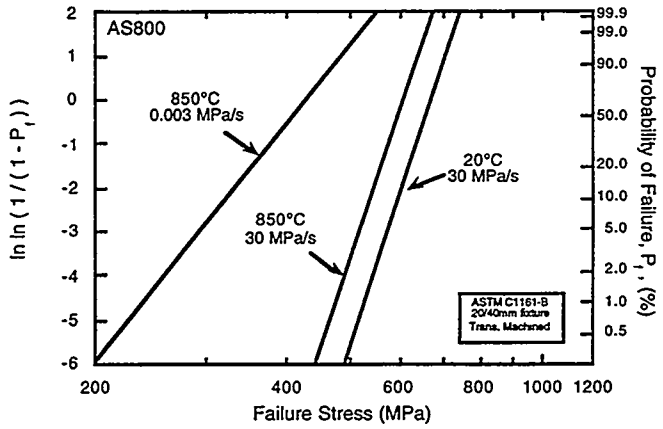

Figure 2. Uncensored, maximum likelihood, Weibull flexure strength distributions of transversely machined AS800 silicon nitride.

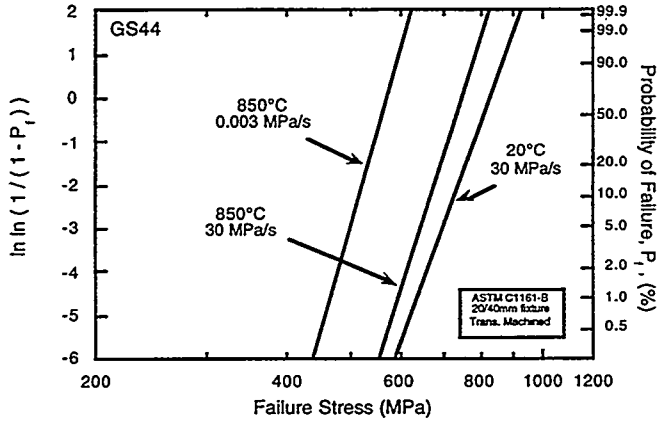

Figure 3. Uncensored, maximum likelihood, Weibull flexure strength distributions of transversely machined GS44 silicon nitride.

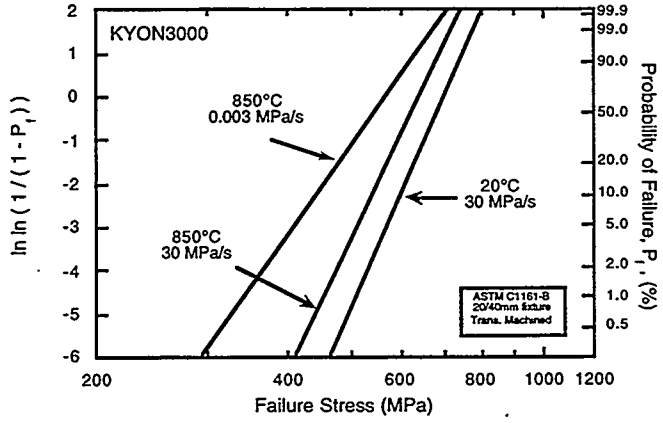

Figure 4. Uncensored, maximum likelihood, Weibull flexure strength distributions of transversely machined KYON3000 silicon nitride.

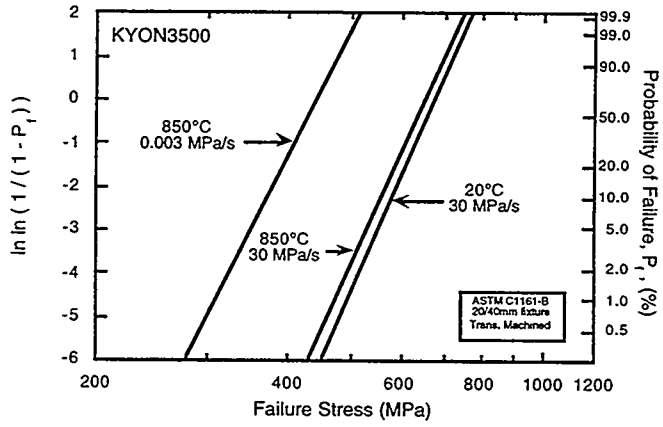

Figure 5. Uncensored, maximum likelihood, Weibull flexure strength distributions of transversely machined KYON3500 silicon nitride.

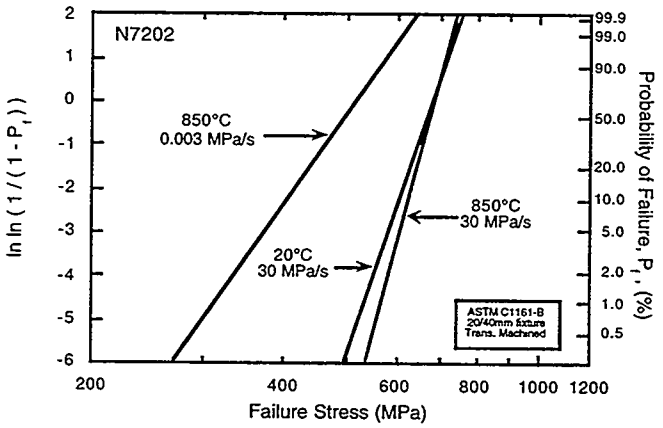

Figure 6. Uncensored, maximum likelihood, Weibull flexure strength distributions of transversely machined N7202 silicon nitride.

Field Emission Analytical Electron Microscopy for Characterization of Catalyst Microstructures

L. F. Allard and T. A. Nolan

OBJECTIVE/SCOPE

The objective of the research is to use analytical and high resolution transmission electron microscopy (TEM) to characterize the microstructures of emission control catalysts. Emphasis is placed on relating microstructural changes to performance of diesel NOx reduction catalysts. The research is focussed on understanding these changes through TEM studies of experimental catalysts materials reacted in an ex-situ catalyst reactor system especially constructed to allow appropriate control of the reaction conditions and the transfer of the sample between reactor and microscope.

TECHNICAL HIGHLIGHTS

Work has continued on the characterization of catalyst materials for potential use to trap NOx and SOx species in both gasoline and diesel exhaust streams. In experiments conducted with our colleague Dr. C. K. Narula at Ford Research Laboratory, a series of samples of Ag/Al_2O_3 materials and sol-gel-processed $BaO.nAl_2O_3$ materials have been reacted under controlled conditions at FRL, and the resulting specimens characterized using the Hitachi HF-2000 FE-TEM at the HTML to determine the morphological changes resulting from the reaction treatments. The results and the general conclusions of these studies are outlined briefly below.

Ag/Al_2O_3 materials

The Ag/Al_2O_3 catalyst system was used in studies of the efficacy of this material for trapping SOx species upstream of a NOx trap. Sulfur oxides (SOx) present in the exhaust are also trapped by the NOx trap materials during lean operation.. The sulfates thus formed reduce NOx trapping efficiency. A high temperature reduction of sulfates leads to regeneration of NOx traps. However, the high temperature exposure causes the trap to deteriorate. Furthermore, the high temperature requirement leads to a high fuel efficiency penalty. These phenomena are primarily of concern for NOx and SOx emissions from gasoline engines, but understanding these mechanisms may also be important for operation of similar traps for diesel engines.

In order to circumvent the SOx problem, it has been proposed to use a SOx trap, comprising a transition metal oxide, upstream of the NOx trap. Transition metal oxides oxidize both SOx and NOx during the lean cycle, but trap only SOx because transition metal nitrates are unstable at SOx trap operating temperatures. The SOx trap strategy is based on the premise that SOx released during the rich-burn cycle will not be trapped by the downstream NOx trap. To test our hypothesis, we exposed a Ag/ Al_2O_3 material to (i) an extended lean cycle, (ii) an extended rich cycle, (iii) and an extended alternating lean-rich cycle in.a reactor system at Ford, but collected the sample at the mid-point of the rich cycle. We hypothesized that SOx is probably trapped as SO_3^{2-} or oxidized by NOx to SO_3 and then trapped as SO_4^{2-} in the rich cycle.

TEM observations of samples taken during the lean cycle operation showed widely dispersed, large discrete Ag particles, which showed no S species even in long acquisition time energy dispersive spectra. However, an EDS spectrum acquired for a long time (several hundred sec) from a large region of the material which did not show discrete metal particles showed small Ag and S peaks, suggesting that the Ag and S species were dispersed over the support surface at the nearly atomic level. In the sample taken during a rich operating cycle, the alumina morphology was identical to that of the original material, but in this case there was a uniform distribution of 10nm Ag particles. S was not detected by EDS in this specimen, even after 10 min acquisition times. The disparity between the Ag particle sizes in the lean vs rich samples may be an anomaly due to non-homogeneous distributions of Ag in the material, and the fact that such small amounts of material are used in preparation of the TEM specimen. However, the possibility that Ag rearrangement with operating treatments will be determined with further experiments.

$BaO.nAl_2O_3$ materials

$BaO.nAl_2O_3$ materials prepared by a sol-gel process were studied to obtain information on the structural changes that occur on thermal treatment that might have significant effects on the efficiency of these materials for trapping nitrogen oxides in exhaust gas streams. Samples with high concentrations of BaO were shown to crystallize barium aluminates at low temperature, leading to a drastic reduction in surface area. However, the formulation BaO.6Al2O3 was shown to retain a high surface area even after sintering at 900°C. After impregnation with 1% Pt, the high BaO material showed only a 20% NOx trapping efficiency, but the $BaO.6Al_2O_3$ material showed a 70% NOx trapping efficiency, both during alternating lean-rich cycles of 1 minute duration. Further improvement in NOx trapping efficiency was observed using gels of BaO.6Al2O3 prepared in the presence of Tergitol® 15-S-12, a neutral surfactant. The NOx trapping efficiency of this powder impregnated with 1%Pt and 0.4%Rh is 95%.

Barium aluminate gels prepared in the presence of another surfactant, PL-64, showed surface properties almost identical to the materials prepared with Tergitol. However, as detailed in the present report, the TEM clearly showed Tergitol-mediated $BaO.6Al_2O_3$ material to have a structure consistent with molecular sieve structure (also confirmed by low-angle XRD). The PL-64- mediated $BaO.6Al_2O_3$ structure was borderline, however, and will require further study by low-angle XRD to determine if the structure can be considered to retain a molecular sieve structure.

The retention of the high surface area of the $BaO.6Al_2O_3$ even after sintering at 900°C, and the high NOx trapping efficiency of the Tergitol and PL-64 surfactant-mediated structures makes this type of material a strong candidate for future NOx trapping schemes.

Papers published

1. C.K. Narula, S. R. Nakouzi, R. Wu and L.F. Allard, "Sol-Gel processed $BaO.nAl_2O_3$ materials derived from $Ba[Al(O^iC_3H_7)_4]_2$: Their evaluation as NOx trap materials;" submitted to J. Catalysis, Sept. 1999.

MATERIALS AND TESTING STANDARDS

IEA Annex II Management (April 1, 1999-September 30, 1999)
M. K. Ferber and K. Breder (Oak Ridge National Laboratory)

Objective/Scope

The purpose of this task is to organize, assist, and facilitate international research cooperation on the characterization of advanced structural ceramic materials. A major objective of this research is the evolution of measurement standards. This task, which is managed in the United States by ORNL, now includes a formal IEA Annex agreement identified as Annex II between the United States, Germany, Sweden, Japan, and Belgium. The original annex included four subtasks: (1) information exchange, (2) ceramic powder characterization, (3) ceramic chemical and physical characterization, and (4) ceramic mechanical property measurements. In the United States, a total of 13 industrial and government laboratories have participated and contributed their resources to this research. The research in Subtasks 2, 3, and 4 is now complete. In 1990, research in two new subtasks was initiated, including Subtask 5, Tensile and Flexural Properties of Ceramics, and Subtask 6, Advanced Ceramic Powder Characterization. The research in Subtasks 5 and 6 was completed in 1993 and the reports were distributed. Two new tasks (Subtask 7 on Ceramic Machining and Subtask 8 on Ceramic Powder Characterization) were proposed in late FY 1993 and the research is completed (1996). Subtask 7 in the United States included eight companies and three federal laboratories. The report on the results from research performed in the United States on Subtask 7 is complete (the final report has been compiled of all the international research and distributed). Subtask 8 included six companies. The final report for Subtask 8 is complete. In 1996, research in two new subtasks was initiated, including Subtask 9 - Thermal Shock and Subtask 10 - Ceramic Powder Characterization.

Recent Developments

Meeting of Coordinators for Subtask 9 Thermal Shock - Indianapolis, April 27, 1999. (Held in conjunction with the 101st American Ceramic Society Annual meeting.)

No formal working group meeting had been called because up to a week before the America Ceramic Society Meeting it was still uncertain whether the U.S. Department of Energy (DOE) would support continued work. However, Matt Ferber opened the meeting saying that at a recent meeting at ORNL Dr. Sid Diamond had declared that he was positive to continue the collaboration under the IEA. Hence the group needed to continue with plans to coordinate suggestions for continued work. Rolf Wäsche stated that the funding situation in Germany is uncertain, and that Fraunhofer Institute therefore is out of the collaboration for now. However, at BAM in Berlin they will acquire thermal testing equipment and will be able to participate in the IEA collaboration, perhaps with work on thermal fatigue. They would possibly be interested in initiating work on Thermal Barrier Coatings (TBCs). Mineo Mizuno stated that he had investigated the status of TBCs in Japan and said there is no support for performing this type of work on TBCs. The manufacturers keep most of the TBC work proprietary, and it is very difficult to establish collaboration in this area.

It was decided that all countries should send suggestions for work to ORNL by the middle of May, and we will try to find common ground between these. A draft of this should be ready for discussion and vote at the Executive Meeting to be held in Paris on or about October 4, 1999. A discussion of how long the next sets of subtasks should last followed. NEDO in Japan wanted two years, i.e., ending the task March 2001. Germany and Sweden agreed that at least two years was needed, however, it was thought that at least two years from the actual start of the subtasks should be needed. The matter of timing will have to be

an item for the executive committee to discuss in October. Robert Pompe also stated that the timing needed to be coordinated with the powder group. Matt Ferber posed the question to the powder group; could they consider characterizing plasma spray powders.

Mineo Mizuno distributed the Japanese report from Subtask 9. The German report had been distributed previously. The Swedish results will be delayed due to their delayed entrance into the Subtask. The goal is to have the Swedish data in time to distribute the draft of the international report at the Executive committee meeting in October.

Discussion followed about the annual (biannual) report for the Implementing Agreement. One of the focuses of this report will be links to standards bodies and documentation how our work is linked to these. Matt Ferber will solicit input from all members for the annual report. This needs to be at ORNL by the end of May 99.

The next Executive Committee Meeting will be held in Paris at the IEA Headquarters on October 12, 1999. Preceding the meeting (October 11), a Workshop will be held with the End Use Working Party (EUWP) to discuss our Implementing Agreement (IA) and strategic planning regarding our future effort.

Subtask 9, Technical Efforts

The preliminary draft report of the U.S. Subtask 9 research is complete. The final Subtask 9 report is being compiled by the U.S. and includes each country's results.

Subtask 10, Characterizing Ceramic Powders

Major responsibility for this subtask in the United States is at NIST, and a detailed report of progress in these subtasks is provided in the section of this report submitted by NIST.

Status of Milestones - Milestone 411529 has been changed and completed (June 1, 1999) [Organize data and prepare outline for final reports (Subtask 9 & Subtask 10] to [Organize data and prepare outline for final report (Subtask 9)] since the Subtask 10 work is completed by NIST and reported by them. Milestone 411531 [Publish Thermal Shock (Subtask 9) Final Report] due date September 30, 1999, has been changed to November 30, 1999. Milestone 411532 [Publish Powder Characterization (Subtask 10) Final Report] due date September 30, 1999, has been changed to November 30, 1999. Milestone 411533 (Provide reports to ASTM) due date September 30, 1999, has been changed to November 30, 1999.

Communications/Visits/Travel - Kristin Breder and Matt Ferber attended the 101st Annual Ceramic Society Meeting and Expo in Indianapolis, Indiana, April 25-27, 1999.

Steve Freiman (NIST), Sandy Dapkunas (NIST), Ray Johnson, Matt Ferber and Kristin Breder met at Oak Ridge National Laboratory to discuss future activities within the IEA activity (September 15, 1999)

Publications and Presentations – Mizuno, Mineo, Mitsue Ogawa, and Yasuo Nagano, "Thermal Shock of Structural Ceramics within IEA Subtask 9," Japanese Final Report, International Energy Agency Co-Operative Programme on Ceramics for Advanced Heat Engines and Other Conservation Applications, Japan Fine Ceramics Center, Nagoya, Japan, March 1999.

NDE Standards for Advanced Ceramics

R. W. McClung

The development of standards is important for the establishment of reliability and acceptance of advanced structural materials. Committee C-28, on Advanced Ceramics, has been organized in the American Society for Testing and Materials (ASTM) to address this issue. One of the activities of the C-28 committee is nondestructive examination (NDE). The Section C-28.02.02 on NDE is reviewing existing standards on NDE (primarily developed for metals) to determine potential applicability for ceramics, as well as drafting original standards. Use of existing or modified standards, if available, is more efficient that generation of new documents and will assure the input of a large body of NDE expertise. Close liaison has been established with ASTM Committee E-7 on Nondestructive Testing, and documents are in various stages of review, recommendations for change, modification, and balloting. R. W. McClung is a subcommittee chairman in both committees and the official liaison.

Technical Highlights

Liaison and technical support have been continued between ASTM committees C-28 and E-7. To date, 50 E-7 NDE standards identified as having potential relevance to ceramics have been reviewed in detail with recommendations made to E-7 for modifications to identified documents. Successful action is complete on 45 documents; eight are being addressed by E-7; others require action by C-28. C-28 standard, C-1175, the guide to existing NDE standards, currently contains relevant information on 36 standards that were approved for incorporation.

A revision to C-1175, the guide to existing NDE standards applicable to advanced ceramics, was balloted successfully at both subcommittee and committee levels. The revision incorporated relevant information from E-7 acoustic emission standards: E-569, Practice for Acoustic Emission Monitoring of Structures During Controlled Stimulation; E-650, Guide for Mounting Piezoelectric Acoustic Emission Sensors; E-750, Practice for Characterizing Acoustic Emission Instrumentation; E-976, Guide for Determining the Reproducibility of Acoustic Emission Sensor Response; E-1106, Method for Primary Calibration of Acoustic Emission Sensors; and E-1781, Practice for Secondary Calibration of Acoustic Emission Sensors. Collated comments on five of the six standards developed during the advisory ballot of C-28.02.02 have been sent to the chairman of the E-7 subcommittee on AE with a recommendation for modification to the standards and E-7 is working on these. The revision to C-1175 received ATM approval, and reprints were published by ASTM in August 1999.

In April a proof copy from ASTM was received, reviewed, corrected, and approved for a prior revision to C-1175 that was approved by ASTM in January 1999. That revision added technical information (scope, summary, and significance and use) about one additional NDE standard from Committee E-7. The standard was E-1817, Practice for Controlling Quality of Radiological Examination by Representative Quality Indicators (RQIs).

The meeting of Committee C-28 was held in Seattle, Washington, May 19-21, 1999. McClung was in attendance but it was necessary for him to return on May 19 due to the death of his wife's mother. Action items related to revisions of C-1175 and liaison with Committee E-7 were reported to the chairman of C-28 in Seattle for use in the meetings.

A limited amount of data has been identified for establishing radiographic equivalence factors for advanced ceramics. Additional specimens will be sought for experimental radiography to develop additional data. A volunteer for the radiography has been recognized. The intent of this action is to provide data for a table in an E-7 standard, E-94 on the radiographic method. Other work in progress includes an amplified outline for a draft standard for reference specimens containing laser-drilled holes and a possible standard on determination of porosity in ceramics using ultrasonic velocity. In addition, interest has been indicated in potential standards for reference specimens for surface flaws and high-resolution penetrant examination.

At the meeting of E-7 in Seattle, Washington, June 27-July 1, 1999, a number of standards were discussed with current or potential future relevance to advanced ceramics. Participation by McClung as C-28 liaison included the executive subcommittee (for liaison reporting), the administrative subcommittee for international standards, and technical subcommittees for radiology, ultrasonics, liquid penetrants, and acoustic emission. Significant activity is ongoing on each of the technical subcommittees on standards of interest and value for advanced ceramics. This includes drafting of new standards, revisions of existing standards, and ballots for approval of the new or revised drafts. Some of the revisions and ballots are based, in part, on requests and comments from C-28; some of the revisions are on standards already incorporated in C-1175, the guide to existing NDE standards. It is necessary to participate in, or maintain awareness of, such revisions to assure the continued applicability to advanced ceramics.

Current activities in the radiology subcommittee on relevant (to advanced ceramics) standards include E-1570, a practice for computed tomographic (CT) examination; E-1441, guide for CT imaging; E-746, test method for determining image quality response of radiographic film; E-999, guide for controlling quality of film processing; E-94, guide for radiographic testing, and E-2007, guide for computed radiology. E-1570, E-1441, E-999, and E-94 are currently incorporated in C-1175. Several standards are progressing toward becoming international standards as part of ISO/TC135 on Nondestructive Testing.

Current activities in the ultrasonic subcommittee on relevant (to advanced ceramics) standards include E-114, a practice for straight beam examination by the contact method; E-587, a practice for angle beam examination by the contact method; E-797, practice for measuring thickness by the contact method; E-1901, guide for detection and evaluation of discontinuities by the contact method; E-214, practice for immersed examination by longitudinal waves; E-1001, practice for detection and evaluation of discontinuities by the immersed method; E-664, practice for measurement of apparent attenuation by the immersed method; E-317, practice for evaluating performance characteristics of ultrasonic testing systems. E-317, E-1001, and E-1324, guide for measuring electronic characteristics of

ultrasonic instruments, are progressing toward becoming international standards in ISO/TC135. E-114, E-587, E-664, E-317, and E-1324 are in the most recently published version of C-1175.

Current activities in the liquid penetrant (and magnetic particle) subcommittee on standards relevant to advanced ceramics include E-165, test method for liquid penetrant examination; E-1210, test method for fluorescent liquid penetrants using the hydrophilic post-emulsification process; and E-1220, test method for visible liquid penetrants using the solvent-removable process. Each of these is in C-1175.

Current activities in the acoustic emission subcommittee on standards relevant to advanced ceramics include E-976, guide for determining reproducibility of sensor response; and a new standard on determining sensor response with acrylic waveguides. A new international standard (in ISO/TC135) on secondary calibration of sensors has passed international ballot and will be published. It is based on E-1781; practice for secondary calibration of sensors. E-976 and E-1781 were recently approved by C-28 and ASTM for addition to C-1175.

Activities and discussions in the subcommittee (the USA technical advisory group) for ISO/TC135 included several E-7 standards (relevant to advanced ceramics) advancing through the international revision and balloting process (some discussed earlier in this report). They included E-1001 (ultrasonic immersion testing); E-1324 (characterization of ultrasonic instruments); E-1106 (primary acoustic emission calibration); E-317 (performance characteristics of ultrasonic instruments); and E-1781 (secondary acoustic emission calibration).

Following the E-7 meetings, several standards from Committee E-7 that are incorporated in C-1175 were revised and balloted at subcommittee level by E-7. These were reviewed and comments prepared to assure continued relevance to advanced ceramics. They include E-1441, guide for computed tomography (CT) imaging, E-1570, a practice for CT examination (being revised in response to earlier comments from Committee C-28), E-317, a practice for evaluating performance characteristics of ultrasonic systems, and E-587, a practice for ultrasonic angle-beam examination by the contact method. In addition, a ballot was conducted on a revision to E-214, a practice for immersed ultrasonic examination using longitudinal waves, that was prepared largely in response to requests from C-28. After successful balloting by E-7 and publication of the revision by ASTM, it is anticipated that it will have become relevant to advanced ceramics for incorporation into a revision of C-1175.

IEA Subtask 10
Lin-Sien Lum and Said Jahanmir
National Institute of Standards and Technology
Bldg 223, Room A256, Div. 852
Gaithersburg, MD 20899

Objective/Scope

The objectives of the IEA Subtask 10 were to evaluate test methods for the characterization of selected properties of ceramic powders through an international round robin study and to determine the repeatability and reproducibility of the test methods. The results will be used to develop recommendations for drafting of national and international standard test methods. Thirty-four laboratories from Belgium, Germany, Japan, Sweden and the U.S representing industrial, academic and government research organizations participated in this program.

The properties that were measured during this project consisted of: 1) Characterization of powders suspended in water (particle dispersion); 2) Characterization of spray dried powders (flow rate, particle size distribution, and moisture and binder content); and 3) Green body characterization (bulk density and strength). Three powders were studied: silicon nitride, silicon carbide, and aluminum oxide.

Technical Progress

All the data for the round robin has been compiled and entered into the database. The final report is being completed. The round robin data were summarized for each of the measurement method by presenting the mean of each laboratory data, the standard deviation for each of the laboratory data, the overall mean and the overall standard deviations. Graphical presentations of the round robin data for all measurement method were also prepared. In addition, precision statements such as repeatability and reproducibility were calculated for each set of data for which sufficient values were available. Repeatability described how well the laboratory is able to obtain the data using the same method on identical test material in the same laboratory by the same operator using the same equipment. Similarly, reproducibility described how the data is reproduce between different laboratories using the same method on identical test material using similar different equipment.

The compiled data were analyzed to determine the repeatability of the data within each laboratory and to examine variations in the data obtained by different laboratories. However, significant variations were observed for a few measurement methods when the test results from different laboratories were compared. These measurement methods that resulted in unacceptable variation will need further evaluation to improve the procedures used for testing before the results can be used to establish national and international standard test methods for characterization of ceramic powders.

Communications/Visits/Travel-

Technical Leaders Meeting at Indianapolis, Indiana, April 27, 1999

Ceramic Mechanical Property Test Method Development

George D. Quinn (National Institute of Standards and Technology)

Objective/Scope

This task is to develop mechanical test method standards in support of the Propulsion Systems Materials Program. The test methods should meet the needs of the DOE engine community but should also consider the general USA structural ceramics community as well as foreign laboratories and companies. Draft recommendations for practices or procedures shall be developed based upon the needs identified above and circulated within the DOE ceramics engine community for review and modification. Round-robins will be conducted as necessary, but shall be well-focused, limited in scope, and complementary to IEA round-robins. Procedures developed in this program will be standardized by ASTM and/or ISO.

Technical Highlights and Results

1. Summary

In this semiannual period, there was progress on several standards. The ASTM fracture toughness standard was finally adopted after years of work. Several International Standards Organization Standards were advanced. A new silicon nitride bearing ball material specification was prepared by the "Rolling Element Bearing Group." We worked on the following formal standards

1.	ISO DIS 14704	Advanced (Fine) Ceramics - Determination of Flexural Strength at Room Temperature (NIST-USA convenes)
2.	ISO DIS 14705	Fine Ceramics (Advanced Ceramics, Advanced Technical Ceramics) - Test Method for Hardness for Monolithic Ceramics at Room Temperature (Convened by Japan, NIST represents the USA)
3.	ISO WD 15765	Advanced (Fine) Ceramics - Determination of Flexural Strength at Elevated Temperature (NIST-USA convenes)
4.	ISO DIS 15732	Fine Ceramics (Advanced Ceramics, Advanced Technical Ceramics) - Determination of Fracture Toughness at Ambient Temperature by Single Edge Precracked Beam (SEPB) Method (Convened by Japan, NIST coordinates with ASTM Task Group)
5.	ISO draft	Fine (Advanced) Ceramics - Determination of Fracture Toughness at Room Temperature by the Surface Crack in Flexure (SCF) Method (convened by USA-NIST)
6.	ASTM C1421-99	"Standard Test Methods for Determination of Fracture Toughness of Advanced Ceramics Conversion of PS 070-97
7.	REBG-draft	Specification for Silicon Nitride Bearing Balls

(DIS = Draft International Standard; WD = Working Draft)

Earlier work in this project has contributed to twelve completed standards:

1.	ASTM C 1161-90	Standard Test Method for Flexural Strength of Advanced Ceramics at Ambient Temperature
2.	ASTM C 1198-91	Dynamic Young's Modulus, Shear Modulus, and Poisson's Ratio for Advanced Ceramics by Sonic Resonance
3.	ASTM C 1211-92	Standard Test Method for Flexural Strength of Advanced Ceramic at Elevated Temperature
4.	MIL HDBK 790	Fractography and Characterization of Fracture Origins in Advanced Structural Ceramics
5.	ASTM C 1239-94	Standard Practice for Reporting Strength Data and Estimating Weibull Distribution Parameters
6.	ASTM C 1322-96	Standard Practice for Fractography and Characterization of Fracture Origins in Advanced Ceramics
7.	ASTM C 1326-96	Standard Test Method for Knoop Indentation Hardness of Advanced Ceramics.
8.	ASTM C 1327-96	Standard Test Method for Vickers Indentation Hardness of Advanced Ceramics.
9.	ASTM PS 070-97	Standard Test Methods for the Determination of Fracture Toughness of Advanced Ceramics
10.	ASTM E-1875-98	Standard Test Method for Dynamic Young's Modulus, Shear Modulus, and Poisson's Ratio by Sonic Resonance
11.	ASTM E-1876-98	Standard Test Method for Dynamic Young's Modulus, Shear Modulus, and Poisson's Ratio by Impulse Excitation
12.	ASTM C 1421-99	"Standard Test Methods for Determination of Fracture Toughness of Advanced Ceramics

The last one was recently approved by ASTM and culminates nearly 9 years of work on this difficult topic. The length gestation period of this standard was caused by a variety of factors, but our perseverance paid off. The comprehensive standard includes three different test methods giving users some flexibility. The three methods produce identical answers for a simple, flat R-curve ceramic material. During the last 9 years, there were several major international round robins that fed information into the standard. NIST prepared a supporting standard reference material. The ASTM task group refined the three test methods, monitored emerging developments in the state of the art of testing, incorporated new aspects to reflect new knowledge of R-curve behavior of ceramics, and interacted with other ASTM committees, foreign standards groups, and American industry. This all took time and patience.

2. Fracture Toughness

2a. ASTM Standard - Refine PS 070 and create C 1421-99

The provisional ASTM standard PS 070-97 was finally converted and adopted as a full consensus ASTM standard designated C 1421-99. Over 110 revisions were made to the Provisional Standard.

2b. Standard Reference Material 2100 for Fracture Toughness

The Standard Reference Material for fracture toughness was finished and was available for sale in June 1999. This is the first reference material in the world for the property fracture toughness for any class material (metal, ceramic, polymer, composite). During this semiannual period, the certificate that accompanies the test specimens was revised and edited, and final statistical analyses conducted. SRM 2100 costs $335 for a kit of 5 specimens with certified fracture toughness.

2c. Draft International Standard, SEPB Method, ISO Technical Committee TC 206, Fine Ceramics

The latest draft fracture toughness by the Single Edged Precracked Beam (SEPB) method standard, which was prepared by Dr. T. Nose in Japan, was reviewed and only minor changes recommended prior to the ISO Technical Committee meeting in London in June 1999. The document has been approved for a Final Draft International standard (FDIS) ballot. The document is harmonious in most respects with ASTM C 1421-99.

2d. Draft International Standard, SCF Method, ISO Technical Committee TC 206, Fine Ceramics

The success with the SEPB fracture toughness standard in TC 206 prompted us to propose a second test method for fracture toughness, but based on the Surface Crack in Flexure method. This is one of the three in ASTM C 1421-99. This proposal was approved and a draft prepared and reviewed at the London June 199 meeting. Although initially reticent about this method (since it is not in their Japanese Industrial Standards standard), the Japanese delegation is cooperating and offered to contribute an annex on how the SCF method could be applied to characterization of R-curve behavior. The document has "working draft" status and a revised version must be prepared in the fall of 1999

3. Flexure Strength at Room Temperature - New Semiarticulating Fixture Design

No activity this period. All work is complete, but a report and engineering drawings must be prepared.

4. Diametral Compression

No activity this period. This work is on hold pending further intensive fractographic analysis to determine why our earlier test specimens did not fracture from volume flaws in the middle of the specimens. We remain optimistic that this method can be refined and made into a user friendly, standardized test. In response to a request from Kristin Breder at ORNL a compilation of a few key references was made.

5. Flexure Testing of Cylindrical Ceramic Specimens

Figure 1 shows the new fixture design developed as part of the NIST Machining of Ceramics Consortium. Since there is interest within the DOE Heavy Duty Diesel community for such testing, we accelerated the development of these fixtures in this program. A paper is in preparation for the Journal of the American

Ceramic Society which will feature the new fixtures. In response to a request from K. Breder at ORNL, a polished set of engineering drawings was prepared and sent to ORNL for review. HTML may make a set and compare results to those obtained with their in-house fixtures.

We derived closed form analytical solutions for the effective surface and effective volume of cylindrical ceramic tests pieces for flexure strength tests. These formulas will facilitate comparisons of

Figure 1 Flexure Fixture For Cylindrical Specimens with a Glass Specimen

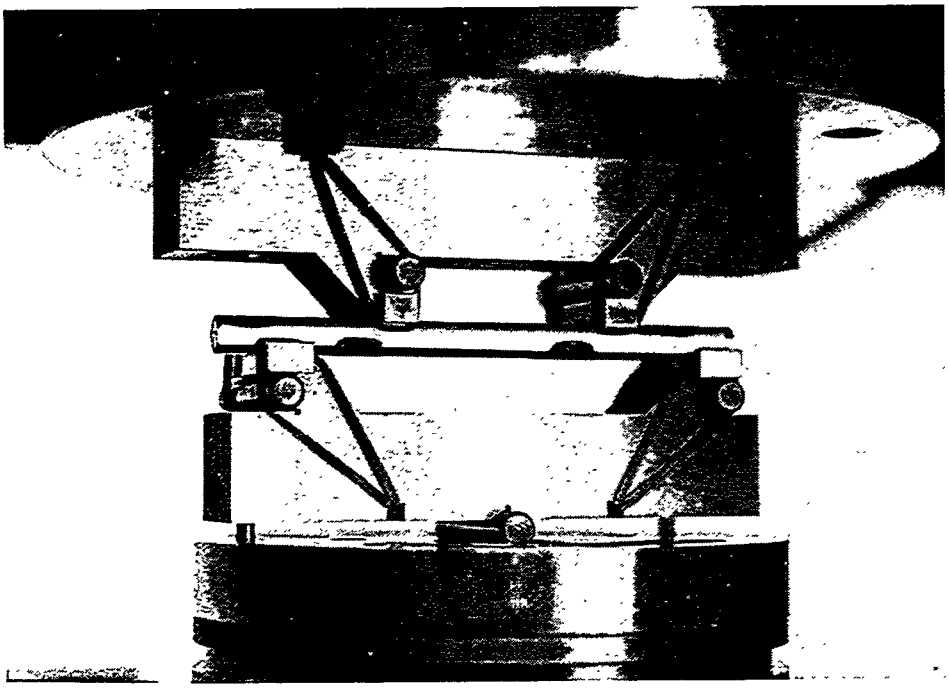

cylindrical specimen strengths to rectangular specimen strengths. The odd appearing equations have appeared infrequently in the literature through the years and usually in very obscure places. For example, progress reports of work by the University of Nottingham, England in the late 1970's for the UK Defense Research Office included a few of the equations. Dr. S. Starrett at SoRI may have derived the same equations (but did not list them explicitly) in progress reports for the US Air Force. To rectify this, we derived the equations from scratch and will include them in a review paper manuscript on testing cylindrical test specimens. The closed form equations are listed below:

Table 1 Effective Volumes and Surfaces for flexural loaded cylinders

Configuration	V_E	S_E
Uniform bending	$V\frac{1}{\pi}G$	$S\frac{(m+2)}{2\pi}G$
3-point	$V\left(\frac{1}{\pi(m+1)}\right)G$	$S\left(\frac{(m+2)}{2\pi(m+1)}\right)G$
4-point, general*	$V\left(\frac{1}{2\pi(m+1)}\right)[4n+2(m+1))(1-2n)]\,G$	$S\left(\frac{(m+2)}{4\pi(m+1)}\right)[4n+2(m+1))(1-2n)]\,G$
4 point, -1/4 point	$V\left(\frac{(m+2)}{2\pi(m+1)}\right)G$	$S\left(\frac{(m+2)^2}{4\pi(m+1)}\right)G$
4-point, 1/3 point	$V\left(\frac{(m+3)}{3\pi(m+1)}\right)G$	$S\left(\frac{(m+3)(m+2)}{6\pi(m+1)}\right)G$

* The inner loading points are located at nL inwards from either outer support point. E.g., for 1/4 point four-point loading, n= 1/4.

V and S are the total volume and surfaces, respectively of the test specimen within the two outer (support) loading points.

m is the Weibull modulus

G is a combined Gamma function (where Γ is the Gamma function):

$$G=\left(\frac{\Gamma\left(\frac{m+1}{2}\right)\Gamma\left(\frac{3}{2}\right)}{\Gamma\left(\frac{m+4}{2}\right)}\right)$$

6. Flexure Testing of Segmented Cylindrical Ceramic Specimens

No progress this period.

7. Rolling Element Bearing Group (REBG) Silicon Nitride Bearing Ball Specification

A draft material specification for silicon nitride is being developed by the REBG, an association of bearing manufacturers and users and the Department of Defense. The draft specification is at an advanced stage and includes a suite of materials requirements including density, color uniformity, surface finish, surface flaws, hardness, flexure strength, and fracture toughness. The specification was prepared by the REBG based upon prior internal company specifications in use at SKF and MRC. The members of the silicon nitride bearing ball subcommittee include the US Department of Defense (US Air Force Wright Patterson AFB, Defense Center Supply, Richmond; and the Defense Contracts Management Center, Buffalo), Norton Advanced Ceramics, Hoover Precision Products, Enceratec (Cummins-Toshiba), ESK, Pratt and Whitney, SKF, MPB, MRC, the Aerospace Corp, Quasar International, Hughes, Winsted Precision, Draper Lab, and NIST.

The REBG is an association of bearing manufacturers, bearing users, and the Department of Defense but it is not formally sanctioned by the US Department of Defense. Their new specification will become a "standard" despite the fact that REBG is not a classic "standards development organization, (SDO)" such as the American Society of Testing and Materials, the American Society of Mechanical Engineers, or the

American Petroleum Institute. This is not unusual in the United States, however. Of the 93,000 standards in the United States, approximately 18,000 have been prepared by Trade Associations or Consortia such as REBG.

The new specification is titled: "Silicon Nitride Bearing Ball Specification." There are three possible classes. Class I is the highest grade for extreme performance requirements and Class III the lowest grade for low duty applications. The document is 14 pages long and includes citations of 10 ASTM test method standards, 6 *of which were developed in large part due to work in this DOE program.* These include ASTM C 1161, flexure strength; C 1198 and C 1259, elastic modulus; C 1327, Vickers hardness; C 1239 Weibull modulus; and C 1421, fracture toughness.

As an example of the application of the standards in the specification, mean flexure strength may be measured by 4-point flexure according to C 1161 and:

Class I silicon nitride shall have a strength of 700 MPa or greater.
Class II silicon nitride shall have a strength of 600 MPa or greater
Class III silicon nitride shall have a strength of 450 MPa or greater.

Similar specifications are set for Weibull modulus, elastic modulus, hardness, fracture toughness, chemical purity. There are microstructural limits on second phases and porosity. We are gratified that ASTM C-28 standards are used by the specification. Unfortunately, a group of Japanese Industrial Standards and a few German DIN standards are also listed as options. This will cause some confusion. For example a class I bearing material must have a 4-point strength of 700 MPa or greater, but it is not specified whether this result may be obtained with the smaller 3 x 4 x 30+ mm JIS specimen or the larger 3 x 4 x 40+ mm ASTM "B" specimen (or from the ASTM mini "A" sized specimen for that matter). The specification's authors do not seem to be cognizant of the variation in ceramic strength due to specimen size differences. This must be cleared up.

The specification also includes a Weibull modulus requirement. A class I bearing material should have a Weibull modulus, M, of 10 or more, but nowhere is it stated how to obtain this value. Only 20 specimens be tested. Using Weibull modulus in a specification is a "risky" proposition. Years of work in the DOE program by this investigator and many other DOE subcontractors (e.g. GE; Allied Signal, Ford, ORNL-HTML, etc,) have shown that estimates of Weibull modulus are "noisy" due to simple statistical sampling variability. For example, one investigator may obtain an M of 9 with his sample set of 20 specimens when the true M is 12. The low estimate is just a common outcome from using a limited sample size (n=20). The low M from the one data set would cause the material to be unfairly rejected. Different values may be obtained by different analysis techniques (linear regression with various probability estimators or maximum likelihood). We will recommend that the REBG cite and use the ASTM standard C 1239 for estimating M. This will resolve the analysis methodology issue, but it will not resolve the uncertainty or statistical sampling variability issue.

The draft specification has other weak elements but these can be polished up by standards experts. A 6 page critical review of the draft was sent to key individuals in the REBG. The REBG met in Jacksonville, Florida on the 4th and 5th of May 1999 and the ceramic ball subcommittee went over many of these technical issues. Most suggested revisions were adopted, but a few outstanding issues need to be discussed with some members who were not in attendance. For example, some of the strength and Weibull modulus values in the specification were originally suggested by SKF, in the Netherlands, so we need to establish how strongly they wish to adhere to the suggested numbers. The next meeting of the REBG is in November 1999 in Long Beach, CA.

The Department of Defense has implemented a Military Specification Reform which is transitioning many standards and specifications to private USA SDO's. Consequently, the REBG Steering Committee decided in September to recommend that the REBG be dissolved as a separate association and become affiliated with ASTM as a new Committee "Rolling Element Bearings." It is likely that this step will be approved by the REBG membership during a formal ballot which is now underway. The REBG silicon nitride specification may be one of the last accomplishments of the REBG association. The specification probably will be converted eventually into a full consensus ASTM material specification (one of the six classes of standards that ASTM prepares).

8. Other Activities

8a. Fractographic Webb Site

NIST finished the installation of the new NIST web site for fractographic analysis of advanced ceramics. The web site, which is in essence a skeletal version of ASTM standard C 1322, is:

http://www.ceramics.nist.gov/webbook/fracture/fracture.htm

8b. ISO Technical Committee TC 206 (Fine Ceramics)

WG 2 Flexure Strength at Room Temperature

Following recommendations by Mr. Quinn, the ASTM Committee voted "negative" on the draft international standard, which actually had been prepared by Mr. Quinn, the convener for this topic. It was agreed that the draft did not adequately deal with the issue of test humidity and its effect on test results. This point had been raised by the Korean delegation in the last TC 206 Fine Ceramics meeting in September, 1998. A number of nations agreed that if humidity was not controlled or monitored during the experiments, then there could be problems comparing results. A proposed remedy to the DIS was presented at the London TC meeting and was approved by the attendees. The language in the draft pertaining to reporting humidity will be strengthened and additional cautionary remarks regarding the desirability of conducting inert atmosphere testing will be added

WG 3 Hardness

A draft prepared by the Japanese convener was found to be completely satisfactory to the USA. The draft is consistent with (and indeed, uses some figures from) ASTM standards C 1326 and C 1327 prepared by ASTM Committee C-28. The USA voted affirmative with no comments on this DIS.

WG 8 Flexure Strength at Elevated Temperature

The latest draft of this ISO test method was extensively revised and distributed prior to the ISO TC 206 meeting in London in June. Despite strong Japanese pressure to eliminate as-fired specimens and fully-articulating fixtures as options in the draft, these elements were retained since they are integral to the USA and European testing methods. Some limits to bow and curvature of the specimen were incorporated.

WG 10 Elastic Modulus

At the ISO TC 206 meeting, we helped represent the United States in the Working Group 10, Elastic Modulus, meeting. Back in the USA after the meeting, we reviewed the rationale for choosing a specimen size of 75 mm x 15 mm x 3 mm in the ASTM C 1198 and C 1259 resonance standards. Follow up messages were sent to Dr. Gonczy, the USA ASTM task group leader, and to Dr. Sakaguchi, the ISO working group convener.

WG 11 Weibull statistics

We helped represent the United States and the ASTM position on the Weibull modulus ISO draft standard. Dr. Steven Duffy of Cleveland State prepared a draft standard and this was presented to the ISO delegates at

the London TC 206 meeting. The draft was based on the ASTM standard C 1239 and includes multimodal flaw analysis. Although no other nation uses it, we managed to persuade the other delegates to retain the multiple flaw population analysis.

8c . Proposed VAMAS round robins

At the VAMAS Technical Working Area 3, Ceramics meeting in late June in England, six new projects that may be of interest to DOE contractors were proposed by VAMAS members. For further information, please contact Mr. Quinn at NIST.

1. ***High Temperature Flexure Strength*** Dr. M. Mizuno of Japan Fine Ceramic Center presented a proposal for this project. This work is intended to support the development of the ISO TC 206, Fine Ceramics, elevated temperature flexure strength test standard. This project started in October 1999. From the USA, ORNL (Breder) and NASA-Glen (Choi) are participating.
2. ***Surface Roughness*** Proposed by the National Physical Laboratory, United Kingdom, this project is on hold pending analysis of the European Phase I project.
3. ***Nondestructive Characterization*** Dr. O. Toft Sorenson of RISOE, Denmark proposed a project for nondestructive characterization (NDC) of ceramics. The objective is to determine whether micro-defects in ceramics can be characterized effectively by current nondestructive characterization techniques and whether the data obtained by these techniques can be used reliably to predict mechanical strength.
4. ***Elastic Modulus***

Dr. R. Morrell of NPL initiated a project for elastic modulus determination. The project would include: static flexure of a beam, beam resonance by forced excitation, beam resonance by impulse excitation, and ultrasonic time of flight.

5. ***Wear resistance***

Dr. J-P. Erauw and Dr. P. Descamps of the Belgian Ceramic Research Center in Mons proposed a project for wear resistance evaluation. CRIBC has a new model for correlation of wear resistance to basic mechanical properties such as elastic modulus, hardness, and fracture toughness.

6. ***Thermal Shock***

Dr. R. Wäsche of BAM, Berlin proposed a thermal shock project. BAM is acquiring a laser shock apparatus for thermal shock evaluation of ceramics. It is understood that few other laboratories could have such equipment, but Dr. Wäsche proposed that laboratories could compare different methods on a common material. Mr. Quinn will coordinate any VAMAS thermal shock program with **IEA subtask 9 activities**.

8d. Elastic Modulus by Resonance - Refinements to ASTM standards C 1198 and C 1259 for chamfers.

Years ago as part of this project, we helped write ASTM standard C 1198 for the determination of elastic modulus of ceramics by resonance of prism specimens. This standard was adapted to more modern impulse excitation methods which also use beam resonance and a follow on standard C 1259 was prepared. In each case, the method involves vibrating a beam specimen and measuring the natural resonance frequency. The mathematical equations which relate elastic modulus to the beam dimensions, beam mass, and the resonant frequency assume that the beam has a perfect rectangular geometry. C 1198 and C 1259 recommended against using chamfered bars.

We recently realized that the effect of the chamfers could be accounted for quite simply. The chamfers may simply alter the moment of inertia of the beam cross section and that this effect was directly analogous to experimental error caused in flexure strength testing. In April, Jeff Swab of the US Army Research Laboratory came to NIST to use our resonance equipment on both chamfered and unchamfered ceramic test bars. Jeff measured the resonant frequencies and found that indeed, the chamfers did affect the results. We devised a correction factor for the presence of the chamfers and this correction matched the experimental shift almost perfectly. We will suggest that ASTM standards C 1198 and C 1259 be rewritten with new appendices to include the correction factor for chamfers. These two standards will now be much more versatile and users may apply them to chamfered, ordinary flexure specimens with high confidence. A

paper on the analytical and experimental data was written and submitted to the Communications of the American Ceramic Society.

Status of Milestones

412124	Prepare comprehensive paper on hardness testing of ceramics	Completed May 1999
412129	Write comprehensive report on fracture evaluation by SCF method	Delayed

The following 4 milestones should be deferred or canceled due to unexpected test methodology problems.

412132	Commence diametral compression round robin	Cancel
412133	Prepare draft diametral compression standard for ASTM	Cancel
412134	Prepare review paper on diametral compression method	Cancel
412138	Conduct new Phase II diametral compression strength tests	Defer to 2000

Problems encountered

None this period, except that the attention paid to the REBG, ISO, and ASTM resonance-chamfer activities have limited our progress on other elements.

Publications/Presentations

1. J. Salem, L. Ghosn, M. Jenkins, and G. D. Quinn, "Stress Intensity Factor Coefficients for Chevron-Notched Flexure Specimens and A Comparison of Fracture Toughness Methods," presented at Cocoa Beach ACS meeting, January 1999, to be publ. Ceram. Eng. and Sci. Proc., 1999.
2. G. D Quinn, K. Xu, and R. Gettings, Standard Reference Material 2100: Fracture Toughness of Ceramics," presented at Cocoa Beach ACS meeting, January 1999, to be publ. Ceram. Eng. and Sci. Proc. 1999
3. G. D. Quinn, "Indentation Hardness Testing of Ceramics," Chapter 3E of Materials Testing and Evaluation, Vol 8, Mechanical Testing, subm to ASM, Materials Park, OH, 1999.
4. G. Quinn and J. Swab, "Elastic Modulus by Resonance of Rectangular Prisms: Corrections for Chamfers," subm. to Comm. Am. Ceram. Soc., 1999.
5. G. Quinn, "Fracture Toughness Testing of Ceramics," Chapter 7d of Encyclopedia of Materials: Science and Technology," Elsevier, to be publ. 2001.

Communications/Visits

* Several calls, emails and faxes were exchanged in the ASTM task group on the topic of the ASTM fracture toughness standard and also the ISO draft SEPB standard test method. Jon Salem and Mike Jenkins were contacted in order to help set up the fracture toughness ASTM symposium in November 2000.
* Many calls, emails and faxes were sent to ASTM and DOE members in connection with the ISO standards.
* Mr. Quinn attended the meeting of the Rolling Element Bearing Group (REBG) in Jacksonville, FL, on the 4th and 5th of May 1999. A series of communications was exchanged with Jeff Wickwire of Defense Contract Management Center, Buffalo, NY regarding the REBG silicon nitride specification.
* A list of important diametral compression papers was compiled and sent to Kristin Breder at ORNL.
* A set of engineering drawings of the new NIST machining consortium fixtures for cylindrical rods was prepared and sent to K. Breder at ORNL.
* Mr. Quinn visited BAM in Berlin to coordinate VAMAS and IEA programs.

* Sung Choi at NASA-Lewis (Glen) was contacted regarding the elevated temperature flexure strength round robin.
* Mr. Quinn contacted Drs. Craft and Filatovs at NC A&T and S. Starrett at SoRI regarding cylindrical flexure strength testing.
* One set of biaxial stress rupture data (ring on ring at 1200°C) was sent to John Gyekenyesi and Sung Choi at NASA-Glen for review. The data will be used to help verify NASA's life prediction codes.
* Jeff Swab of the US Army Research Laboratory came to NIST to use our resonance equipment on both chamfered and unchamfered ceramic test bars.

INTERNAL DISTRIBUTION

L. F. Allard, Jr.
P. F. Becher
T. M. Besmann
P. J. Blau
R. A. Bradley
C. R. Brinkman
T. D. Burchell
A. Choudhury
D. D. Conger
S. A. David
M. K. Ferber
R. L. Graves
C. R. Hubbard
M. A. Janney
D. R. Johnson (5)
R. R. Judkins
M. A. Karnitz
E. Lara-Curzio
R. J. Lauf
K. C. Liu
W. D. Manly
S. B. McSpadden
T. A. Nolan
A. E. Pasto
M. H. Rawlins
A. C. Schaffhauser
D. P. Stinton
T. N. Tiegs
S. G. Winslow
R. E. Ziegler
Laboratory Records - RC

EXTERNAL DISTRIBUTION

Jeffrey Abboud
U.S. Advanced Ceramics Assoc.
1600 Wilson Blvd., Suite 1008
Arlington VA 22209

B. P. Bandyopadhyay
University of North Dakota
Box 8359 University Station
Grand Forks ND 58202-8359

Donald F. Baxter, Jr.
Advanced Materials & Processes
ASM International
9639 Kinsman Road
Materials Park OH 44073-0002

M. Brad Beardsley
Caterpillar Inc.
Technical Center Bldg. E
P.O. Box 1875
Peoria IL 61656-1875

Ramakrishna T. Bhatt
NASA Lewis Research Center
MS-106-1
21000 Brookpark Road
Cleveland, OH 44135

Bruce Boardman
Deere & Company, Technical Ctr.
3300 River Drive
Moline IL 61265-1792

Michael C. Brands
Cummins Engine Company, Inc.
P.O. Box 3005, Mail Code 50179
Columbus IN 47201

Donald J. Bray
Advanced Refractory Technologies
699 Hertel Avenue
Buffalo NY 14207

Jeff Bougher
Caterpillar Inc.
Technical Center, Bldg. E
P.O. Box 1875
Peoria IL 61656-1875

Mike Bowling
Cummins Engine Company, Inc.
1900 McKinley Avenue
P.O. Box 3005
Columbus IN 47202-3005

Walter Bryzik
U.S. Army Tank Automotive
Command
R&D Center, Propulsion Systems
Warren MI 48397-5000

David Carruthers
Kyocera Industrial Ceramics
5713 East Fourth Plain
Vancouver WA 98661

Ronald H. Chand
Morton Advanced Materials
185 New Boston Street
Woburn MA 01801

William J. Chmura
Torrington Company
59 Field Street, P.O. Box 1008
Torrington CT 06790-1008

William S. Coblenz
Defense Adv. Research Projects Agency
3701 N. Fairfax Drive
Arlington VA 22203-1714

Gloria M. Collins
ASTM
100 Barr Harbor Drive
West Conshohocken PA 19428-2959

Shawn Cooper
FEV Engine Technology
4554 Glenmeade Lane
Auburn Hills MI 48326-1766

Douglas Corey
AlliedSignal, Inc.
2525 West 190th Street, MS:T52
Torrance CA 90504-6099

Keith P. Costello
Chand/Kare Technical Ceramics
2 Coppage Drive
Worcester MA 01603-1252

Gary M. Crosbie
Ford Motor Company
P.O. Box 2053, 20000 Rotunda Drive
MD-3182, SRL Building
Dearborn MI 48121-2053

Pamela Cunningham
WETO Technical Library
MSE, Inc.
Industrial Park, P. O. Box 4078
Butte MT 59702

S. Keoni Denison
Norton Company
1 New Bond Street
Worcester MA 01615-0008

Sidney Diamond
U.S. Department of Energy
Office of Transportation Technologies
EE-33, Forrestal Building
Washington DC 28505

Ernest J. Duwell
3M Abrasive Systems Division
3M Center, Bldg. 251-01-34
St. Paul MN 55144

Michael Easley
AlliedSignal Engines
P. O. Box 52181
MS 551-11
Phoenix AZ 85072-2181

James J. Eberhardt
U.S. Department of Energy
Office of Transportation Technologies
EE-33, Forrestal Building
Washington DC 20585

Jim Edler
Eaton Corporation
26201 Northwestern Highway
P.O. Box 766
Southfield MI 48037

William A. Ellingson
Argonne National Laboratory
Energy Technology Division, Bldg. 212
9700 S. Cass Avenue
Argonne IL 60439-3848

John W. Fairbanks
U.S. Department of Energy
Office of Transportation Technologies
EE-33, Forrestal Building
Washington DC 20585

Ho Fang
Applied Materials
2695 Augustine Drive, MS-0962
Santa Clara CA 95054

Dan Foley
AlliedSignal Ceramic Components
MS:1/5-1, 26000
2525 West 190th Street
Torrance CA 90504

Douglas Freitag
DuPont Lanxide Composites
21150 New Hampshire Avenue
Brookeville MD 20833

Richard Gates
NIST
Bldg. 223, Rm. A-256
Rt. 270 & Quince Orchard Road
Gaithersburg MD 20899

Ludwig J. Gauckler
ETH Zurich
Nonmetallic Materials
Sonneggstr. 5
CH-8092 Zurich, SWITZERLAND

Allan E. Goldman
U.S. Graphite, Inc.
907 W. Outer Drive
Oak Ridge TN 37830

Robert J. Gottschall
U.S. Department of Energy
Metal & Ceramic Sciences, ER-131
19901 Germantown Road
Germantown MD 20874-1290

Thomas J. Gross
U.S. Department of Energy
Office of Transportation Technologies
EE-30, Forrestal Building
Washington DC 20585

Changsheng Guo
United Technologies Research Center
Machining Systems, MS 129-46
East Hartford CT 06108

Darryl Gust
Cummins Engine Company, Inc.
1900 McKinley Avenue
P.O. Box 3005
Columbus IN 47202-3005

Nabil S. Hakim
Detroit Diesel Corporation
13400 Outer Drive West, A08
Detroit MI 48239-4001

Alan M. Hart
Dow Chemical Company
1776 Building
Midland MI 48674

Michael H. Haselkorn
Caterpillar Inc.
Technical Center, Building E
P.O. Box 1875
Peoria IL 61656-1875

Deborah A. Haught
U.S. Department of Energy
Ofc. of Industrial Crosscut Technologies
EE-23, Forrestal Bldg.
Washington DC 20585

Daniel Hauser
Edison Welding Institute
Microjoinint & Plastics Tech. Team
1250 Arthur E. Adams Drive
Columbus OH 43221-3585

John Haygarth
Wah Chang
P.O. Box 460
Albany OR 97321-0460

Gene Huber
Precision Ferrites & Ceramics
5432 Production Drive
Huntington Beach CA 92649-1525

Thomas A. Johnson
Lanxide Corporation
1300 Marrows Road
P.O. Box 6077
Newark DE 19714-6077

Adam Jostsons
ANSTO
PMB1
Menai, NSW, Australia 2234

Yury Kalish
Detroit Diesel Corporation
Mechanical Systems
13400 Outer Drive West
Detroit MI 48239-4001

Roy Kamo
Adiabatics, Inc.
3385 Commerce Park Drive
Columbus IN 47201

Ralph Kelly
Cincinnati Milacron
P.O. Box 9013
Cincinnati OH 45209

W. C. King
Mack Truck, Z-41
1999 Pennsylvania Avenue
Hagerstown MD 21740

Tony Kirn
Caterpillar Inc.
Defense Products Dept., JB7
Peoria IL 61629

Joseph A. Kovach
Parker Hannifin Corporation
6035 Parkland Boulevard
Cleveland OH 44124-4141

Edwin H. Kraft
Kyocera Industrial Ceramics
5713 E. Fourth Plain Boulevard
Vancouver WA 98661

Oh-Hun Kwon
Norton Company
Saint Gobain Industrial Ceramics
1 Goddard Road
Northboro MA 01532-1545

S. K. Lau
B. F. Goodrich Aerospace R&D
9921 Brecksville Road
Brecksville OH 44141

Elaine Lentini
Saint-Gobain Industrial Ceramics
Goddard Road
Northboro MA 01532

Stan Levine
NASA Lewis Research Center
21000 Brookpark Road, MS:106/5
Cleveland OH 44135

Robert H. Licht
Norton Company
Saint Gobain Industrial Ceramics
1 Goddard Road
Northboro MA 01532-1545

E. Lilley
Norton Company
Saint Gobain Industrial Ceramics
1 Goddard Road
Northboro MA 01532-1545

B. J. McEntire
Applied Materials Corporation
3050 Bowers Avenue
Santa Clara, CA 95054

James McLaughlin
Sundstrand Power Systems
4400 Ruffin Road
P.O. Box 85757
San Diego CA 92186-5757

Biljana Mikijelj
Ceradyne, Inc.
3169 Red Hill Avenue
Costa Mesa CA 92626

Carl E. Miller
Delphi Energy & Engine Mgmt. Systems
4800 S. Saginaw Street, MC 485-301-150
P. O. Box 1360
Flint MI 48501-1360

Curtis V. Nakaishi
U.S. Department of Energy
Federal Energy Tech. Center
3610 Collins Ferry Rd.
P.O. Box 880
Morgantown WV 26507-0880

Malcolm Naylor
Cummins Engine Company, Inc.
P.O. Box 3005, Mail Code 50183
Columbus IN 47202-3005

Dale E. Niesz
Ceramic & Materials Engineering
607 Taylor Road, Rm. 204
Piscataway, NJ 08854-8065

Thomas J. Paglia
Coors/ACI
3315 Boone Road
Benton AR 72015

Richard Palicka
CERCOM, Inc.
1960 Watson Way
Vista CA 92083

Vijay M. Parthasarathy
Solar Turbines
2200 Pacific Highway, M.Z. R-1
San Diego CA 92186

Magan Patel
Cummins Engine Company, Inc.
Mail Code 50183
Box 3005
Columbus IN 47202-3005

James W. Patten
Cummins Engine Company, Inc.
P.O. Box 3005, Mail Code 50183
Columbus IN 47202-3005

Joe Picone
Norton Company
1 New Bond Street
Box 15008
Worcester MA 01615-0008

Stephen C. Pred
Pred Materials International, Inc.
60 East 42nd Street, Suite 1456
New York NY 10165

Vimal K. Pujari
Norton Company
Saint Gobain Industrial Ceramics
1 Goddard Road
Northboro MA 01532-1545

Fred Quan
Corning Inc.
Sullivan Park, FR-2-8
Corning NY 14831

George Quinn
NIST
I-270 & Clopper Road
Ceramics Division, Bldg. 223
Gaithersburg MD 20899

Mike Readey
Caterpillar, Inc.
Technical Center, Bldg. E
P.O. Box 1875
Peoria IL 61656-1875

Harold Rechter
Chicago Fire Brick Company
7531 S. Ashland Avenue
Chicago IL 60620-4246

Jack A. Rubin
CERCOM, Inc.
1960 Watson Way
Vista CA 92083

Robert J. Russell
Riverdale Consulting, Inc.
24 Micah Hamlin Road
Centerville MA 02632-2107

J. Sankar
North Carolina A&T State Univ.
Dept. of Mechanical Engineering
Greensboro NC 27406

Maxine L. Savitz
AlliedSignal, Inc.
Ceramic Components
2525 West 190th Street
P.O. Box 2960, MS:1/5-1, 26000
Torrance CA 90509-2960

Jim Schienle
AlliedSignal Aerospace
1130 West Warner Road
M/S 1231-K
Tempe AZ 85284

Gary Schnittgrund
Transfer Technology
16401 Knollwood Drive
Granada Hills CA 91344

Robert S. Shane
Shane Associates
1904 NW 22nd Street
Stuart FL 34994-9270

Subu Shanmugham
MicroCoating Technologies
3901 Green Industrial Way
Chamblee GA 30341-1913

Albert J. Shih
North Carolina State University
Mechanical & Aerospace Engineering
2217 Broughton Hall, Box 7910
Raleigh NC 27695

Charles Spuckler
NASA Lewis Research Center
21000 Brookpark Road, MS: 5-11
Cleveland OH 44135-3127

Gordon L. Starr
Cummins Engine Company, Inc.
P.O. Box 3005, Mail Code:50182
Columbus IN 47202-3005

Marian Swirsky
Cambridge Scientific Abstract
Commerce Park, Bldg. 4, Suite 804
23200 Chagrin Blvd.
Beachwood OH 44122

Victor J. Tennery
113 Newell Lane
Oak Ridge TN 37830

Malcolm Thomas
Allison Engine Company
P. O. Box 420 (W06)
Indianapolis IN 46206

Marc Tricard
Norton Company
Superabrasives Division
1 New Bond Street, MS-412-301
P. O. Box 15008
Worcester MA 01615-0008

Marcel H. Van De Voorde
Commission of the European Union
Eeuwigelaan 33
1861 CL Bergen
THE NETHERLANDS

V. Venkateswaran
Materials Solutions International, Inc.
P.O. Box 663
Grand Island, NY 14072-0663

Robert M. Washburn
ASMT
11203 Colima Road
Whittier CA 90604

R. W. Weeks
Argonne National Laboratory
Bldg. 362, E313
9700 S. Cass Avenue
Argonne IL 60439

Sheldon M. Wiederhorn
NIST
Building 223, Room B309
Gaithersburg MD 20899

Matthew F. Winkler
Seaworthy Systems, Inc.
P.O. Box 965
Essex CT 06426

Thomas J. Wissing
Eaton Corporation
26201 Northwestern Highway
P.O. Box 766
Southfield MI 48037

James C. Withers
MER Corporation
7960 S. Kolb Road
Tucson AZ 85706

Dale E. Wittmer
Southern Illinois University
Mechanical Engineering Dept.
Carbondale IL 62901

Egon E. Wolff
Caterpillar Inc.
Technical Center
P.O. Box 1875
Peoria IL 61656-1875

Roy Yamamoto
Ethyl Petroleum Additives, Inc.
500 Spring Street
P. O. Box 2158
Richmond VA 23218-2158

R. L. Yeckley
Kennametal, Inc.
P.O. Box 231
Latrode, PA 15650

Thomas M. Yonushonis
Cummins Engine Company, Inc.
1900 McKinley Avenue
P.O. Box 3005, Mail Code 50183
Columbus IN 47202-3005

S. Charles Yoon
Cincinnati Milacron, Inc.
P.O. Box 9013
3000 Disney Street
Cincinnati OH 45209-9013

Jong Yung
Sundstrand Aerospace
Dept. 789-6
4747 Harrison Avenue
Rockford IL 61125

A. L. Zadoks
Caterpillar Inc.
Technical Center, Building L
P.O. Box 1875
Peoria IL 61656-1875

Zhenqi Zhu
Stevens Institute of Technology
Department of Mechanical Engineering
Castle Point on Hudson
Hoboken NJ 07030

Department of Energy
Oak Ridge Operations Office
Assistant Manager for Energy
Research and Development
P. O. Box 2001
Oak Ridge TN 37831-8600

For distribution by microfiche
as shown in DOE/OSTI-4500,
Distribution Category UC-332
(Ceramics/Advanced Materials).